First Principles Study of Effect of Surface Structure on Chemical Activity of Pt Electrocatalysts in Fuel Cells

by

Byungchan Han

B.S. Nuclear Engineering, Seoul National University, 1998
M.S. Nuclear Engineering, Seoul National University, 2000

Submitted to the Department of Materials Science and Engineering
in partial fulfillment of the requirements for the degree of

Doctor of Philosophy in Materials Science and Engineering

at the

MASSACHUSETTS INSTITUTE OF TECHNOLOGY

February 2008

MASSACHUSETTS INSTITUTE OF TECHNOLOGY
JUN 16 2008
LIBRARIES

ARCHIVES

© Massachusetts Institute of Technology 2007. All rights reserved.

Author: _____
Byungchan Han
Department of Materials Science and Engineering

Certified by: _____
Gerbrand Ceder
R. P. Simmons Professor of Materials Science and Engineering Thesis Supervisor

Accepted by: _____
Samuel Miller Allen
POSCO Professor of Physical Metallurgy
Chair, Department Committee on Graduate Students

First Principles Study of Effect of Surface Structure on Chemical Activity of Pt Electrocatalysts in Fuel Cells

by

Byungchan Han

Submitted to the Department of Materials Science and Engineering
on September 20, 2007 in partial fulfillment of the
requirements for the degree of
Doctor of Philosophy in Materials Science and Engineering

Abstract

To facilitate commercialization of fuel cell systems as alternative energy device, the enhancement of Pt electrocatalysts activity is one of the most challenging issues. The first step to the solution is elucidating relationship between surface structure and chemical reactivity as electrocatalysis occurs on its surface. However, in spite of concerted experimental and theoretical research over the last decades, the detailed mechanism is still in debate.

This thesis explores a structural sensitivity of the chemical reactivity in the Pt-based alloy electrocatalysts by combining ab-initio density functional theory (DFT) with relevant thermodynamic and kinetic approach. We developed a rigorous statistical mechanical formalism, which can parameterize the energetics obtained by first principles calculations as a function of

surface topologies. This methodology enables kinetic Monte Carlo simulations to provide thermally equilibrated structures as a function of partial pressures of adsorbates and alloy compositions. With our consistent methods, we characterize surface structures on the atomic scale, and quantify chemical reactivity of various Pt-alloy model systems. Our methodology reproduced accurate and consistent results of available experimental measurements.

We find that our methodology is considerably useful for studying the structural effect on the heterogeneous catalysis. Through the thesis, we understood better how surface structures evolve according to environmental conditions and hence, the structure-activity relationship, which is useful for design of electrocatalysts.

Thesis Supervisor: Gerbrand Ceder

Title: R. P. Simmons Professor of Materials Science and Engineering

Acknowledgement

More than anything else, I would like to thank my parents and two brothers. Without their unconditional devotion and prayer, this thesis could not come out. I wish I could repay small part of their loves with this thesis. I cannot forget my grand master, Chungsan sunsa as my life guide. He introduced a wonderful spiritual world to me, from which I could keep my body and mind healthy against the harsh environment.

My thesis advisor, Professor Gerbrand Ceder supported me with a research funding and great scientific insight. He also showed me qualification of great scientist: Research, speaking and writing. My two thesis committee members, Professor Sanjeev Mukerjee (University of Northeastern) and Nicola Marzari (MIT) are the infinite reservoirs of great scientific ideas. Both of them are smart and humble.

I cannot forget Professor Anton van der Ven (University of Michigan-Ann arbor) who was an awesome mentor for both of the science and my life. During five years as my office mates, he always encouraged me with unbelievably great passion and advice. The time I spent with him will be unforgettable memory for my life.

Many people in my group shared their experiences and knowledge with me. Kathryn Simons, administrator of my group, helped by correcting poor writing skill. In addition, she also introduced to me a great world of Buddhism and nice people. I thank all of the past and current group members: Dane Morgan, Dinesh Balachandran, John Reed, Eric Wu, Ashley Predith, Elena Arroyo, Dany Carlier, Maria Chan, Shirley Meng, Fei Zhou, Chris Fischer, Byoungwoo Kang, Kevin Tibbetts, Yoyo Hinuma, Osman Burak Okan, Xiahua Ma, Geoffroy Hautier, Charles Moore, and Anubhav Jain.

I got also many help from people who visited my group temporarily and from whom I have met in the conference: Professor Andrzej Wieckowski (University of Illinois at Urbana Champaign), Professor Bingjoe Hwang (National Taiwan University of Sci. and Technology), Dr. Chilhoon Doh (Korea Electrotechnology Research Institute), Professor Yang Shao-Horn, Professor Yongtae Kim (Pusan National University), Dr. Ismaila Dabo (MIT), Professor Nakayama Masanobu (Tokyo Institute of Technology), Varun Rai (graduate student at university of Stanford), Dennis Yang, Uni Kim (Master Card), Amy Kim, Seungwoo Lee, Yanghyo Kim (MIT), Taehyun Kim (Hyundai).

Contents

List of Figures

List of Tables

Chapter 1

Introduction

1.1 Overview

A fuel cell is an electrochemical device which *directly* converts chemical energy stored in fuel and oxidant into electric energy [1, 2]. More than 150 years have passed since the principle of a fuel cell was discovered by Christian Friedrich Schönbein (in 1838) and since William Robert Grove demonstrated the first fuel cell apparatus (in 1845) [3]. It was, however, Francis Thomas Bacon who successfully developed a 5 kW stationary fuel cell system (in 1959), which was licensed for use in the U.S. space program to supply electricity and drinking water in 1960s. This was the first commercial use of a fuel cell. With the fast development of global civilizations, however, high-energy consumption and environmental protection have become more serious concerns than ever. Hence, it is crucial to develop new energy sources, which are more thermally efficient and environmentally friendly. In this aspect, fuel cells have attracted interest as an alternative to traditional energy devices because of their high thermodynamic efficiency and generation of environmentally safe products.

However, in spite of its long history of intensive scientific and technological efforts, fuel cells still have too many challenging problems to replace traditional energy devices. Currently the most crucial obstacle is the low performance of the electrocatalyst and electrolyte materials. To overcome the barrier, concerted theoretical and experimental studies have been performed

over the last decades. However, the electrocatalyst and electrolyte materials still need a significant improvement in the performance for wide commercialization of fuel cells.

This thesis focuses on one of the most serious issues in low temperature fuel cells, *the structure sensitivity of the electrocatalyst activity*. For the time being, electrocatalysts in the Proton Exchange Membrane Fuel Cell (PEMFC) and Direct Methanol Fuel Cell (DMFC) are too expensive and kinetically sluggish for fuel (oxidant) oxidation (reduction) and lead to large performance losses in the operation. Most electrocatalytic processes in the fuel cell involve complex sequential or parallel elementary steps (chemisorption of adsorbates, bond forming or breaking, surface diffusion and desorption), and are sensitive to the catalyst structures [4-6]. Although a complete mapping of the *activity–structure* relationship is a formidable task, only a thorough understanding of it enables a rational design of high performing electrocatalysts feasible.

The goal of this thesis is to understand how the surface reactivity of electrocatalysts can change in realistic operating environments. The thesis approaches this aim by characterizing the morphology and composition at the surface of a catalyst as a detailed function of physical and electrochemical conditions. *Ab-initio* density functional theory (DFT) calculations are extensively used to obtain energetics and equilibrium structure of the electrocatalyst system on the atomic level. The surface structures at finite temperature and non-vacuum conditions are acquired by combining the atomic information of the electrocatalyst system with a rigorous statistical mechanical formalism and (kinetic) Monte Carlo simulations. To figure out the fundamental mechanism of how surface structure evolves, the effect of various chemical conditions (adsorbates and alloying) and physical variables (particle size and surface

morphology of a catalyst) is estimated. The surface reactivity of the electrocatalysts is analyzed in terms of electronic and geometric properties of the electrocatalysts, which are correlated with the chemical/physical variables. These studies can contribute to a rationale design of electrocatalysts by suggesting methods for optimizing catalyst structures to achieve a desired activity.

As the first part of the thesis, this chapter begins with an introduction of the general principles (section 1.2) and challenging issues (section 1.3) of current fuel cells. Section 1.4 outlines the thesis.

1.2 Principle of fuel cells

The efficiency of a fuel cell is not limited by Carnot's theorem since it electrochemically converts the chemical free energy stored in its fuel directly into electrical energy (direct current) by a continuous catalytic process. Furthermore, fuel cells are environmentally friendly devices because PEMFC generates only clean water (H_2O) and electricity at its operating location although DMFC produces additional small amounts of CO_2. As shown in Fig. 1-1, it is typically composed of three key components, i.e., anode, cathode, and electrolyte. A hydrated pure hydrogen gas (H_2) or reformate with small amounts of organic impurities is injected into the anode of the PEMFC as a fuel, while a hydrated liquid (or gas) methanol (CH_3OH) is used in the DMFC. By electrochemical oxidation on the electrocatalyst layer, fuel is eventually split into two charge carriers: electrons (e^-) and protons (H^+). The electrons circulate through the external load, while protons diffuse through the electrolyte to reach the cathode. An oxidant, an air or

oxygen gas (O_2), is fed into the cathode, where it is electrochemically reduced by an electrocatalyst to oxygen ions (O^{2-}). Eventually, all species (electrons, protons and oxygen ions) generated by the electrocatalysts react electrochemically at the cathode to produce electricity and clean water. The half-cell and overall chemical reactions and their thermodynamic properties at room temperature are described for PEMFC from Eq. (1-1) to Eq.(1-3) and for DMFC from Eq. (1-4) to Eq. (1-6) [7]. All potentials are represented with respect to a Standard Hydrogen Electrode (SHE) at 25 °C.

PEMFC:

Anode (oxidation half): $2H_2 \rightarrow 4H^+ + 4e^-$ (1-1)

Cathode (reduction half): $O_2 + 4H^+ + 4e^- \rightarrow 2H_2O$ (1-2)

Cell reaction: $2H_2 + O_2 \rightarrow 2H_2O \quad (E_{cell} = 1.23\ V)$ (1-3)

DMFC:

Anode (oxidation half): $CH_3OH + H2O \rightarrow CO2 + 6H+ + 6e^- \quad (E_{anode} = 0.046\ V)$ (1-4)

Cathode (reduction half): $\frac{3}{2} O_2 + 6H^+ + 6e^- \rightarrow 3H_2O \quad (E_{cathode} = 1.23\ V)$ (1-5)

Cell reaction: $CH_3OH + \frac{3}{2} O_2 \rightarrow CO_2 + 2H_2O \quad (E_{cell} = 1.18\ V)$ (1-6)

The two electrodes (anode and cathode) have porous structures, which enables electrolytes and fuel to penetrate into them to facilitate fuel utilization and transport of the charge carriers. The electrolyte is a thin layer (about a few ten micrometers) which shortens the ion diffusion

length. Of course, in addition to the three key components, the fuel cell contains auxiliary devices (current collectors, pumps, and sensors) to achieve the required performance and stability.

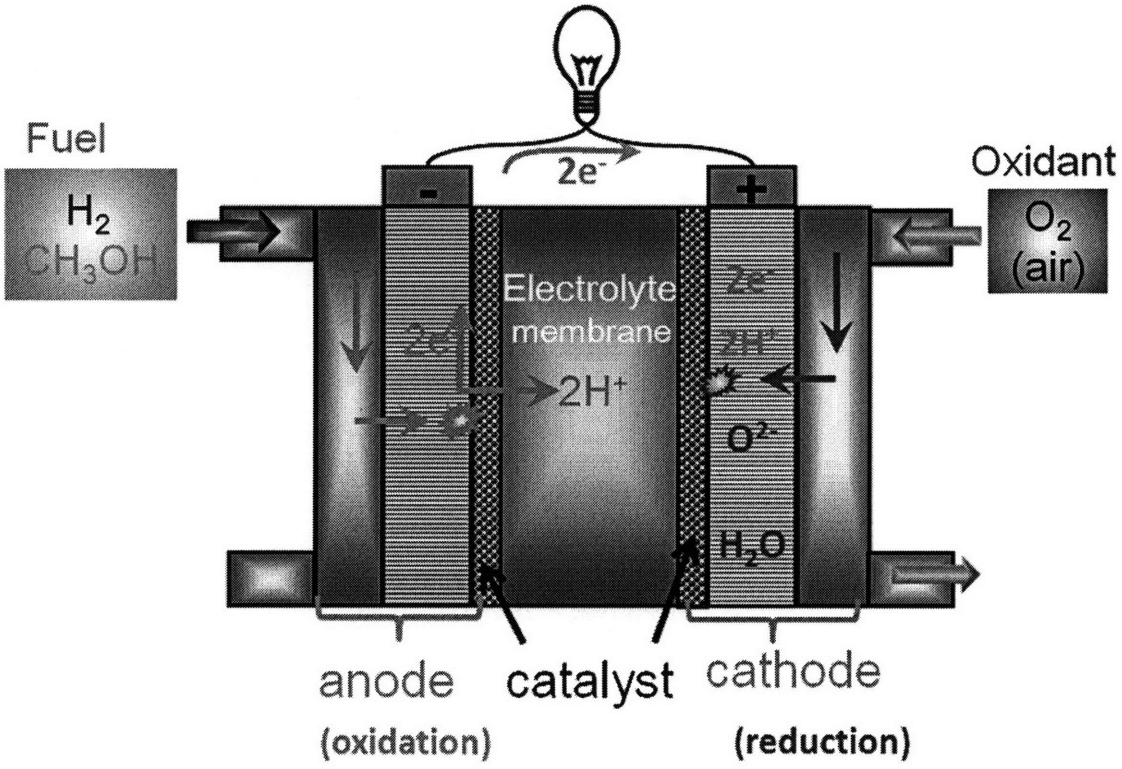

Figure 1-1: Schematic picture of low temperature fuel cells (PEMFC and DMFC) [8].

Fuel cells are generally categorized by their electrolyte, which determines an operating temperature and a fuel form. Table 1-1 shows typical commercialized fuel cells [9] and Fig. 1-2 illustrates electrochemical reactions for each of the fuel cell types. NASA invented Alkaline Fuel Cell (AFC) for the space program to power the Gemini missions and subsequent space shuttle operations. Although it is highly efficient and discharges only pure water, AFC requires pure hydrogen and oxygen gas for its operation since it is easily poisoned by a small amount of CO_2 Phosphoric Acid Fuel Cell (PAFC) commercialized in 1992 uses a concentrated phosphoric acid (H_3PO4) electrolyte retained on a silicon carbide matrix, and is currently the most mature fuel cell type. Since it is highly reliable and efficient, and operates quietly at a medium temperature ranges (150 ~ 220°C), PAFC is currently considered as a small stationary power-generation system. The electrolyte of Molten Carbonate Fuel Cell (MCFC) is an alkali carbonate (i.e., Na_2CO_3, K_2CO_2, or Li_2CO_3) which is held on a ceramic matrix of lithium aluminum oxide ($LiAlO_2$). Because of its high operation temperature (650°C), it is a candidate for large stationary or combined-cycle applications through its use of waste heat for generating additional energy. A Solid Oxide Fuel Cell (SOFC) utilizes a non-porous metal oxide (usually yttria-stabilized zirconia or Y_2O_3-stabilized ZrO_2) electrolyte material. The SOFC is best suited for large-scale stationary power generators to provide electricity for factories or cities since it operates at a very high temperature (800~1000°C).

A PEMFC is the most promising fuel cell type for widespread use because of its unique advantages over other types. Because it operates at low temperature (~80°C) and at ambient pressure ranges, PEMFC allows electric vehicles to start up quickly and can power a portable apparatus. Its electrolyte, a solid-state polymer membrane, is easier to manufacture and reduces

the weight of the fuel cell. The specific power and power density of PEMFC is higher than that of DMFC as shown in the Ragone plot [10] (Fig. 1-3). Because of these advantages, PEMFC has been studied intensively as a power source for transportation vehicles and portable electronic devices.

The DMFC shares many basic structures with the PEMFC except for its fuel, (typically) liquid methanol. Compared to the PEMFC, the DMFC does not require a complex storage system because the liquid state methanol is used directly as fuel. Although the specific energy density of liquid methanol (~19.9 MJ/kg) is much less than that of hydrogen gas (119.9 MJ/kg), the efficiency of storage (95 % for liquid methanol and 0.6% for hydrogen gas) increases the overall energy density of the DMFC. For instance, at 300 bar the actual specific energy density of liquid methanol (18.9 MJ/kg) is much higher than that of hydrogen (0.72 MJ/kg). In addition, since it can operate as a power source of portable electronic devices, the DMFC will share the fuel cell market with PEMFC.

Fuel cell devices are, in a sense, a combination of an internal combustion engine (ICE) and electrochemical batteries [11, 12]. Fuels have to be fed into the system as in an ICE, and like batteries, electric energy is generated by diffusion of the charge carries between electrodes through the electrolyte medium (ion) or external circuit (electron). PEMFC and DMFC, however, have advantages over batteries given their immediate refueling capacities and high specific energy (Fig. 1-3). Typically, the theoretical specific energy of a DMFC with the fuel system is around 3000 W/kg to be compared to batteries of about 200 W/kg. Compared with the ICE, they run quietly since no core parts move during operation and there is no combustion reaction. Unlike ICE, the fuel can be generated from the natural gas and biomass.

Table 1-1: Fuel cell types and their characteristics [9].

Fuel cell type	Electrolyte	Anode (fuel)	Cathode (oxidant)	Operating temperature	Charge carrier	Catalysts	Power (W)	Electric efficiency
Proton Exchange Membrane (PEMFC)	solid polymer membrane	hydrogen	pure or atmospheric oxygen	75°C (180°F)	H^+	Platinum	100W ~ 500 kW	Cell: 50~70% System: 30~50%
Direct Methanol (DMFC)	solid polymer membrane	methanol solution in water	atmospheric oxygen	75°C (180°F)	H^+	Platinum	1mW ~ 100 kW	Cell: 20~30% System: 10~20%
Alkaline (AFC)	potassium hydroxide	hydrogen	pure oxygen	below 80°C	OH^-	Platinum	10 kW ~ 100 kW	Cell: 60~70% System: 62%
Phosphoric Acid (PAFC)	Immobilized liquid phosphorous acid	hydrogen	atmospheric oxygen	210°C (400°F)	H^+	Platinum	~ 10MW	Cell: 55% System: 40%
Molten Carbonate (MCFC)	Immobilized liquid molten alkaline Carbonates	hydrogen, methane	atmospheric oxygen	650°C (1200°F)	CO_3^{2-}	Nickel	100MW	Cell: 55% System: 47%
Solid Oxide (SOFC)	Ceramic Oxide	hydrogen, methane	atmospheric oxygen	800~1000°C (1500~1800°F)	O^{2-}	Perovskite	~ 100MW	Cell: 60~65% System: 55~60%

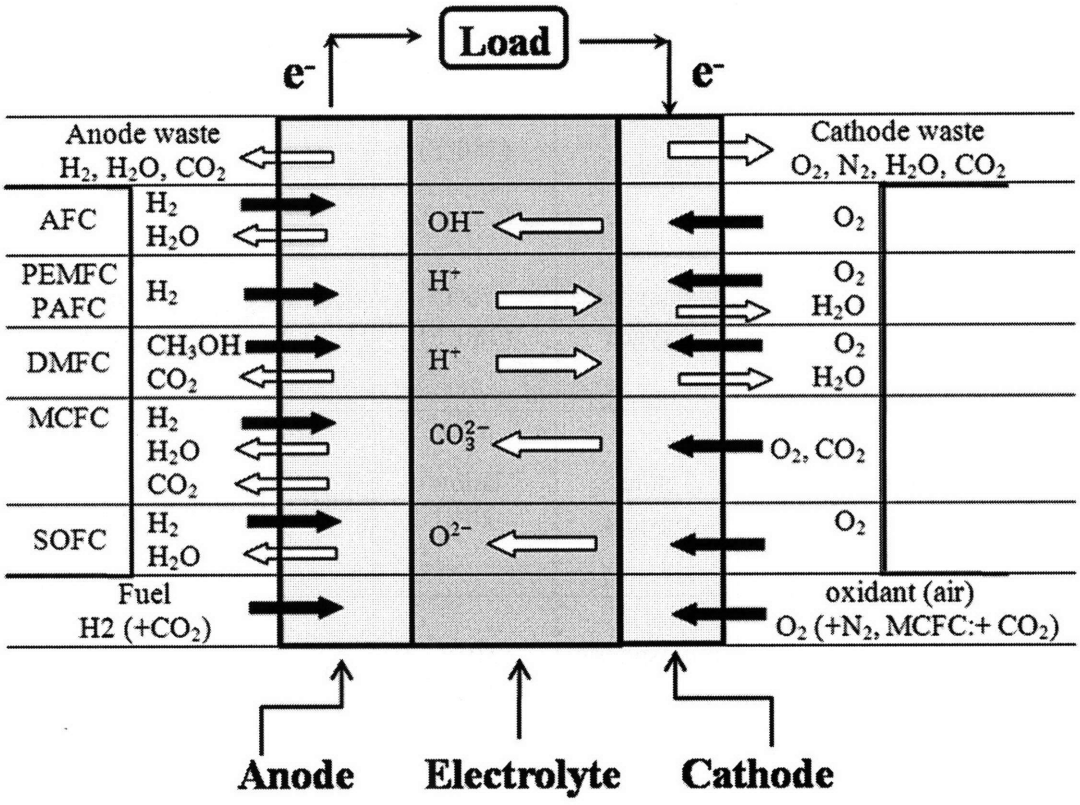

Figure 1-2: Electrochemical reactions of the fuel cell types [9].

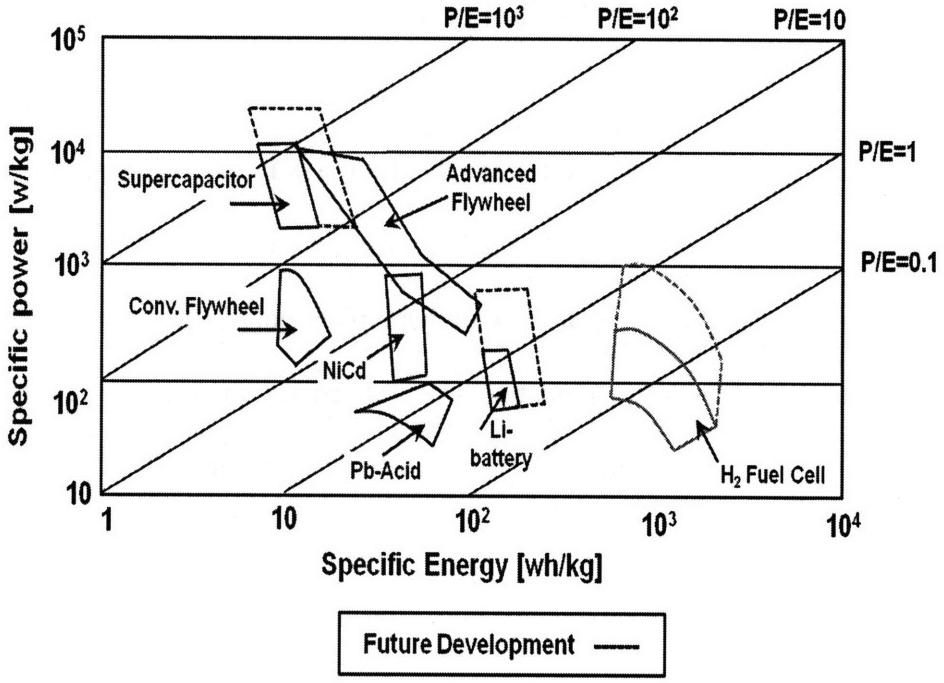

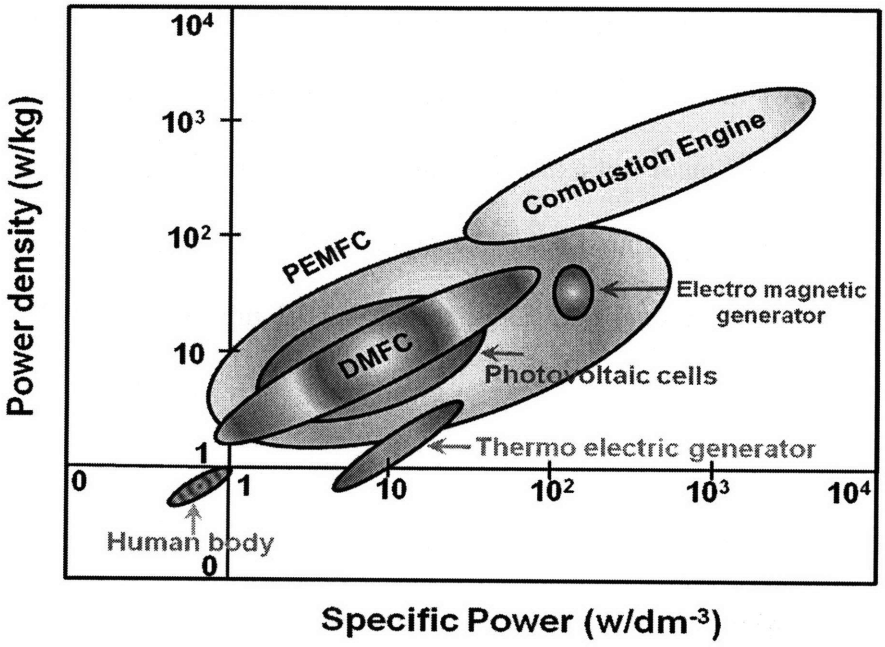

Figure 1-3: Ragone plot of several energy devices. Low temperature fuel cells (PEMFC and DMFC) are located in the region of high specific energy but low specific power compared to other systems [8].

1.3 Challenging problems of the fuel cells

In spite of the intrinsic advantages, PEMFC's and DMFC's still face many challenging problems, which will delay their wide commercialization as alternative energy devices. One of the most crucial issues is a significant decrease of the potentials from their thermodynamic values when a cell operates [1, 13]. Figure 1-4 shows typical polarization curves of the PEMFC and DMFC with the source of the overpotentials [12]. In general, the origin of the overpotentials is classified by three factors as a function of the driving current density.

(1) Kinetic loss by electrocatalysts at low current density ($i \approx 1 \sim 100$ mA/cm^2): electrocatalysts in both of PEMFC and DMFC need about 400 meV overvoltages to oxidize fuel or reduce oxidant at an operating current density of 500 mA/cm2, even with high Pt loading. In the PEMFC, the cathode induces most of the overpotential, while the DMFC has an additional loss (around 40 meV) in the anode because surface adsorbed carbon mono-oxide (COads), produced in the process of methanol oxidation, and deactivates the Pt catalyst. Typical Pt loading in a contemporary PEMFC is around 0.4 ~ 0.8 mg-Pt/cm2 and a few mg-Pt/cm2 in the DMFC, which is still a much higher load than DOE targets of 0.3 mg-Pt/cm2 for 2010 and 0.2 mg-Pt/cm2 for 2015.

(2) Ohmic loss at medium current density ($i \approx 100 \sim 500$ mA/cm^2): the intrinsic resistance of the electrolyte membrane and electrodes leads to performance loss, which is linearly proportional to the current. The charge carriers (electron and proton) generated or consumed at the electrocatalysts have to migrate to the electrode layers. Hence, electrode materials have to

possess good conductivities for protons and electrons. Since the catalyst layer by itself does not conduct protons well, an ionomer is used to enhance the protonic conductivity.

(3) Mass transport at high current density (i > 500 mA/cm^2): fuel and oxidant have to move through the gas diffusion layer (non-reacting diffusion) and the. In addition, the ionic charge carrier (proton) has to migrate through the solid electrolyte between the two electrodes.

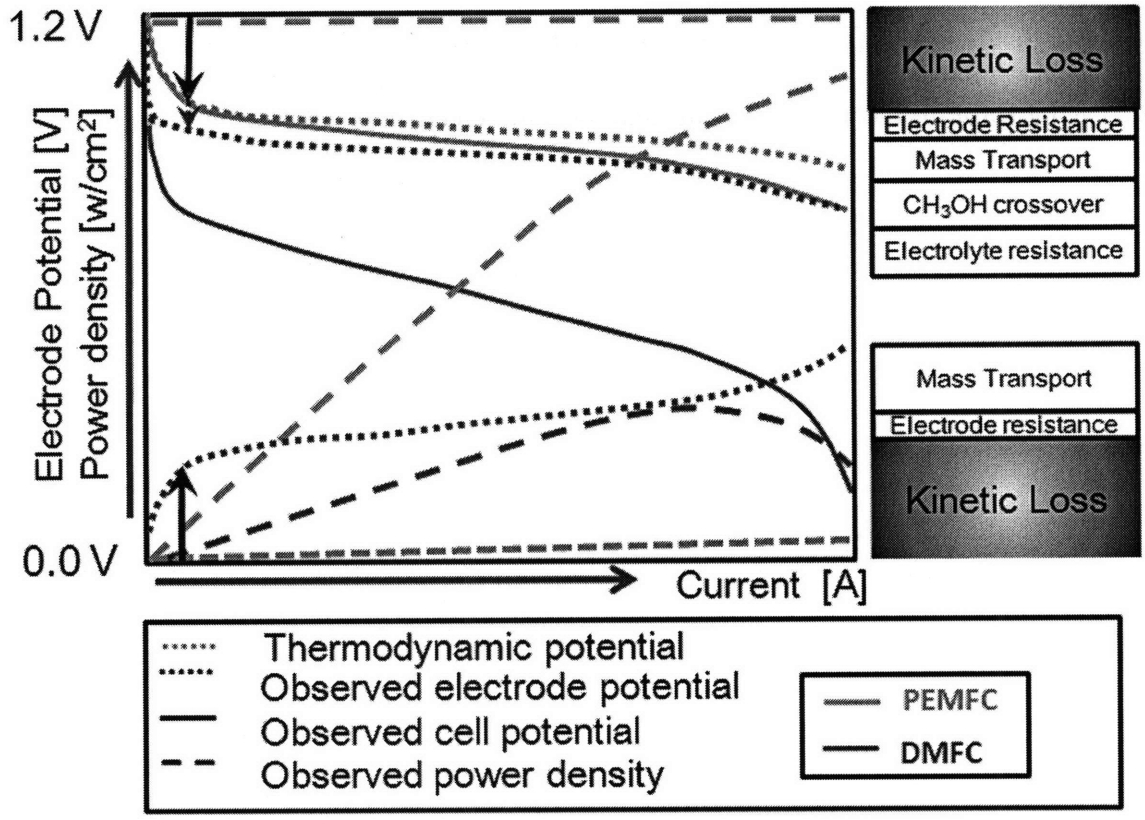

Figure 1-4: Polarization curves and power density of the PEMFC and DMFC with the sources of the overvoltages as a function of a driving current [12].

As Fig. 1-4 shows, the poor kinetic activity of the electrocatalysts is responsible for a large part of the performance loss. In both of the PEMFC and DMFC, cathodes induce most of the overpotentials. However, unlike PEMFC, DMFC suffers from kinetic losses at anode, which is because electrochemical oxidation of methanol takes place in multiple steps as shown in Eqs. (1-7), (1-8) and (1-9).

$$CH_3OH + Pt \rightarrow Pt{-}CO_{ads} + 4H+ + 4e^- \quad (1\text{-}7)$$

$$H_2O + Pt \rightarrow Pt{-}OH_{ads} + H+ + e^- \quad (1\text{-}8)$$

$$Pt{-}CO_{ads} + Pt{-}OH_{ads} \rightarrow 2Pt + CO_2 + H+ + e^- \quad (1\text{-}9)$$

The COads, which is an intermediate of methanol oxidation, substantially poisons the Pt catalyst by forming strong chemical bonds with surface Pt atoms, limiting further fuel oxidation. This poisoning is only removable by oxidizing the COads to CO2 with the help of oxygen containing chemical species (i.e.,OH_{ads}), which are usually generated by water dissociation on the catalysts as shown in Eq.(1-8). On the pure Pt catalysts, however, Eq. (1-8) is known as a rate-determining step with a potential of up to 0.7 V. Hence, to reduce performance loss in the anode of the DMFC it is necessary to invent new catalyst materials, which can dissociate water molecules at a lower potential and are highly active to CO. Over the last couple of decades, through exhaustive theoretical and experimental research, surface scientists discovered a Pt-Ru bimetallic alloy electrocatalyst [14, 15]. Although the exact mechanism is still in debate, it is now generally agreed upon that a Pt-Ru bimetallic catalyst performs much better than pure Pt for relieving CO poisoning.

In addition to their inherent kinetic sluggishness, current Pt-based alloy electrocatalysts are faced with another challenging issue: Durability under cathodic environments. It is observed by experiments that electrocatalysts in the cathode are deactivated over time through dissolution, redeposition, and precipitation [16, 17]. Pt alloy catalysts dissolve at low pH and high potential conditions, which typically are found at the cathode [18]. After dissolution, Pt ions either redeposit on the catalyst surfaces increasing particle size, or migrate through the electrolyte membrane to precipitate as Pt metals by reacting with hydrogen diffused from the anode [17, 19-22]. Both redeposition and precipitation induce serious performance losses as the result of the reduced active surface area. Experimental measurements show that the degradation is accelerated under cyclic potential operations [23-26]. Elements alloyed to Pt (e.g., Co, Cr, Ni, and Fe) dissolve in the electrolyte without redeposition. Hence, only Pt atoms are observed on the surface once alloy elements are leached out resulting in a Pt shell structure. In spite of the experimental observations, the mechanism for the formation of the Pt shell structure is not yet clearly understood. Hence, it has been one of the most interesting topics in the fuel cell electrocatalyst community. To solve this problem, more fundamental atomistic studies are necessary. It is not possible to develop more stable electrocatalysts without a complete understanding of the detailed degradation mechanism.

1.4 Thesis outline

This thesis studies mainly the challenging issues relevant to the electrocatalysts of the PEMFC and DMFC described in the last section. Considering that catalysis is a complicated surface reaction, it is important to understand the mechanism for how surface structures affect the surface reactivity of the electrocatalysts. The surface morphology and composition is influenced by environmental conditions [27], such as pH level, and the electrolyte, support materials, and the imposed electric field. In addition, surface structures significantly depend on the physical properties of the catalyst materials such as particle size, surface energy, and alloying elements. There are many theoretical and experimental investigations showing that the activity of an electrocatalyst is substantially sensitive to its own surface structure [5, 6, 13, 28, 29]. On the other hand, it is also known that surface structure alters both intrinsic (i.e., electronic structure [30-34]) and extrinsic (e.g., a coordination number, crystal plane, and defect on the surfaces) properties [35-40]. Thus, it has been argued that variations of the surface reactivity can be explicable in terms of these two properties. However, a quantitative correlation, which can describe the chemical activity as a function of inherent and environmental variables, has not been discovered yet. This is a hard task since even a pure and clean Pt catalyst has a complicated three-dimensional structure. Figure 1-5 shows a schematic picture of a typical electrode in the PEMFC and DMFC. The electrocatalyst particles are supported by carbon particles, and they are in contact with porous fuel diffusion layers as well as a polymer electrolyte. All of these components may affect the performance of the electrocatalyst. In addition, there are many chemical adsorbates and intermediates, which can selectively interact with a specific alloy

element of an electrocatalyst. For example, the structure of the electrocatalyst can be substantially modified by adsorbate-induced surface segregation [41].

Figure 1-6 shows a schematic picture of how chemical conditions can influence the surface structure (Fig. 1-6(a)) and how the surface morphology changes with particle size (Fig. 1-6(b)). A preferential interaction between atoms in a surface and adsorbates induces a surface segregation of the specific alloy element, which in turn, can cause surface strain. In addition, the adsorbates have attractive or repulsive interactions with each other, which may affect the bond strength of other chemical species with catalyst atoms, and hence their surface coverage. These chemical interactions may considerably modify the electronic structure of a catalyst and change the surface reactivity accordingly. Hence, an accurate estimation of the chemical interaction between adsorbates and catalyst atoms is important in order to predict surface structure and hence, chemical activity. Moreover, since a commercialized catalyst is typically composed of nano-sized particles, the effect of a finite surface area, particle size, and surface anisotropy should be considered as shown in Fig. 1-6(b). In such a case, the surface reactivity of the catalyst will also be influenced by the surface morphology.

Therefore, to solve the challenging issues of electrocatalysts in the PEMFC and DMFC described in the previous section (1.3), it is essential *a priori* to characterize in a systematic way how surface structure and composition is affected by intrinsic and environmental variables, and to capture the essence of the correlation between chemical activity and surface structure (activity versus structure relationship). This approach is also the first step towards developing better electrocatalysts.

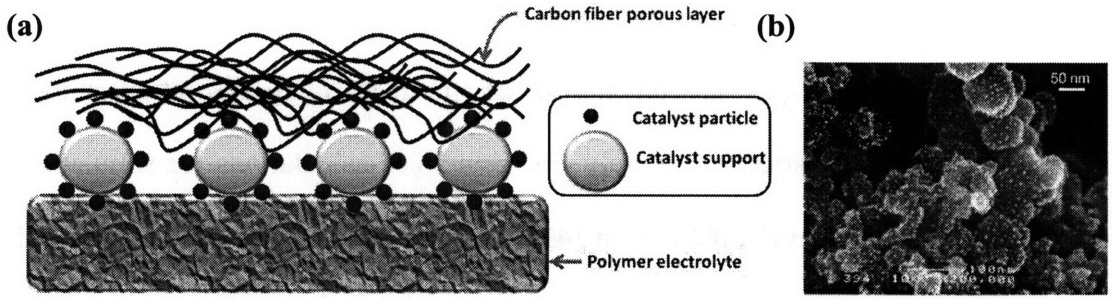

Figure 1-5: A schematic picture of the electrodes in the PEMFC and DMFC in (a) and a picture of Pt-Ru alloy catalyst observed by a scanning tunneling microscope in (b) [42].

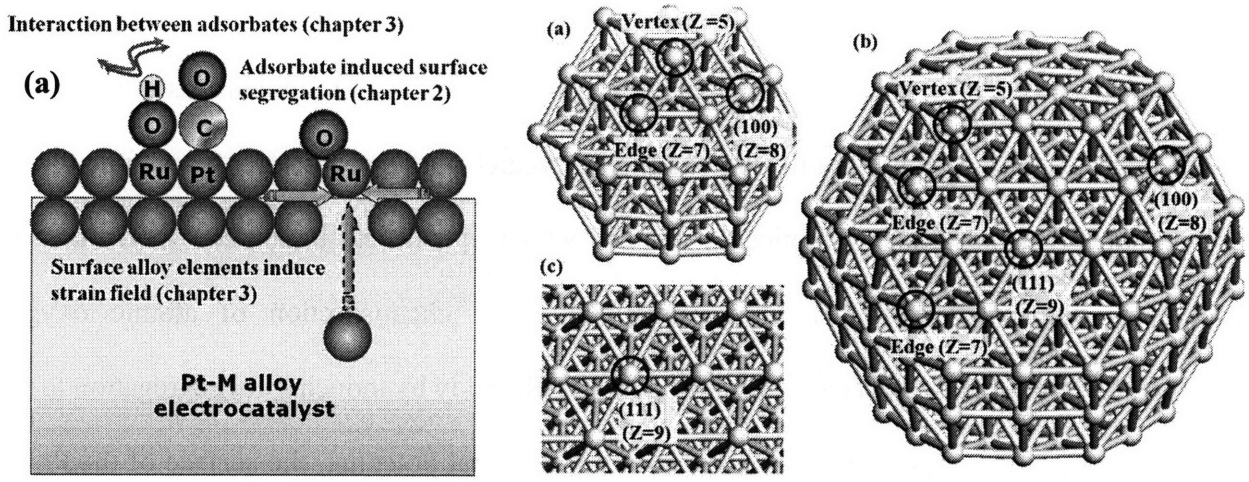

Figure 1-6: A schematic picture of possible interactions between catalyst atoms and adsorbates in an extended flat surface in (a). The picture (b) shows model systems for Pt as a function of its particle size (N is total number of surface atoms located at symmetrically the same site and Z is the coordination number of the site defined as the average nearest neighbor coordination of the Pt atom(s) that configures the adsorption site.

In experimental measurements, it may be a formidable task to decouple the chemical and physical variables shown in Fig 1-6, while an ab-initio method is well suited for this purpose. Although modern experimental instruments often produce high resolution pictures of electrocatalyst surfaces on a small scale, only first principles calculations (or simulations) can generate detailed atomistic level information [43]. During the last couple of decades, the ab-initio density functional method has been used extensively to elucidate the mechanism of heterogeneous electrocatalysis [4, 44]. This method has provided accurate thermodynamic and kinetic quantities as well as precise images of surface structures on an atomic scale. Hence, it is generally accepted that first principles DFT calculations are useful and reliable for explaining the mechanism of a heterogeneous catalytic reaction [4].

In chapter 2 of this thesis, the effect of adsorbed oxygen on the surface structure of a Pt-Ru alloy catalyst is examined. To estimate chemical interaction energies between oxygen atoms and catalyst atoms, first principles thermodynamics are combined with the coupled cluster expansion theory [45] enabling Monte Carlo simulations to predict surface structures as a function of temperature and adsorbate chemical potential which quantifies interaction potentials of adsorbates and catalyst atoms. The results show that chemisorption of atomic oxygen significantly modifies the surface composition of a Pt-Ru alloy by inducing Ru segregation to the surface. For a mild oxygen partial pressure and Ru chemical potential, the surface of the Pt-Ru catalyst is largely divided into isolated domains of Pt or oxygen covered Ru. We discuss why this surface structure has a beneficial effect on relieving CO poisoning and hence, on the activity of Pt-Ru alloy catalysts.

Chapter 3 studies how the bonding between Pt and CO_{ads} is affected by surface alloying and by coadsorption of O or OH with CO. We find that adsorbates induce considerable surface relaxation, which decreases chemisorption energy of CO on Pt surface. On the other hand, alloying Ru to a Pt surface slightly enhances the CO-Pt bond strength. The Ru is oxidized by O or OH. For the latter, the more likely scenario, the chemisorption energy of CO on the Pt site decreases considerably.

Chapter 4 studies on the effect of the physical shape of a catalyst particle on its surface reactivity with adsorbates. To decouple particle size and surface morphology, three catalyst model systems are set up: an extended Pt(111) surface in addition to 1 and 2 nm Pt clusters. By using first principles Density Functional Theory (DFT) calculations, chemisorption energies of O and OH on the model systems are obtained as a function of particle size for different adsorption sites. Through this study, we find that particle size and local morphology of the adsorption site considerably affect the surface reactivity of Pt with O and OH. The variation of the chemical properties of the Pt catalysts is explained in terms of the local electronic structure and coordination. Each of these contributions to chemical adsorption energy is decoupled and correlated to chemical activity. Using the correlations of activity-structure (electronic and geometric), it is discussed how to optimize the chemical activity of the electrocatalysts.

Chapter 5 explores electrochemical modeling of the transport of (charged) chemical species. The modeling describes an interface kinetics using more generalized transport kinetics than a classical Ficks' diffusion equation. This "phase field model" is applicable to the multiphase

system. Unlike in Ficks' diffusion equation, the thermodynamic driving force in a phase field model is obtained by expanding the local free energy of the system. Hence, it can describe moving boundary problems well, which is of interest in the microstructure evolution phenomena of multi-phase systems. In this chapter, the diffusion coefficient of a lithium (Li) particle, one of the charge carriers in the intercalating Li-ion batteries, is calculated, and is compared with the results from Potentiostatic Intermittent Titration Techniques (PITT) and Galvanostatic Intermittent Titration Techniques (GITT) simulations by using Ficks' law for a model system with a wide two-phase region.

Chapter 2

The Effect of Adsorbate and Alloying on Surface Structure of Pt Electrocatalyst

2.1 Overview

Of the several factors influencing surface structures of electrocatalysts in low temperature fuel cell, chemical adsorbates and alloying are of critical importance. This is because electrocatalysts are exposed to non-vacuum environment during operation, and they are not just pure Pt but alloyed with other elements. The natural question, then, arises: how does the interaction between chemical species and electrocatalyst atoms modify its surface structure and composition?

This chapter explores surface segregation induced by adsorbates on the surfaces of the Pt-Ru alloy electrocatalysts. To investigate how these collective behaviors of adsorbates and alloy elements affect the surface structures, ab-initio thermodynamics is combined with kinetic Monte Carlo simulations. The results show that surface segregation can be substantially modified by the presence of adsorbates and present a first-principles method that allows equilibration of simultaneous segregation and adsorption on surfaces with fixed topology. The method is based on a coupled cluster expansion theory to write the state of the system in terms of adsorbate and occupation variables on the surface layer. This model can be parameterized with Density

Functional Theory (DFT) calculations and equilibrated at finite temperature with Monte Carlo simulation. The method is applied to surface ordering and segregation on a (111) surface of $Pt_{(1-x)}Ru_x$ alloys in the presence of adsorbing atomic oxygen. While Pt segregates under vacuum conditions, the strong bond between oxygen and Ru couples the segregation energy of the Ru to the oxygen chemical potential. As a result, we find that variations in oxygen chemical potential can dramatically alter the segregation and surface ordering tendency of dilute Ru in Pt.

2.2 Introduction

Inorganic surfaces play a key role in the kinetics of many processes through catalysis of chemical reactions, or as preferred nucleation sites for phase transformations. A crucial step to understand the mechanism by which such reactions proceed is therefore the detailed chemical and structural characterization of surfaces. Most of first principles calculations are performed under vacuum conditions and provide detailed electronic and structural information. While such calculations can be compared to Ultra-High Vacuum (UHV) experiments, they may be less relevant to understand the behavior of a surface in operating environments. Hence it is needed to develop a method to deal with one particular aspect of non-vacuum conditions, namely adsorbate controlled surface segregation. The basic motivation for this work is that the segregation energy of elements in an alloy is influenced by their interaction with the adsorbed layer: When species are adsorbed on the surface, the segregating atoms see a different environment, which will affect their segregation energy. We focus here on segregation on a surface of Pt-Ru alloys important to the catalysis of methanol under varying degrees of oxygen adsorption, though the formalism is

independent of this specific chemistry, and could be used to study other alloys/adsorbate combinations. Pt catalysts are often alloyed with transition metals in order to enhance their tolerance to carbon mono-oxide (CO) poisoning. For example, addition of Ru to Pt catalysts has been shown to reduce CO poisoning dramatically. While the precise mechanism by which Ru prevents CO poisoning is unclear, it has been proposed that Ru alloying either reduces the bond strength between CO and Pt through its modification of the electronic structure at the catalyst surface [46, 47], or enhances the oxidation of CO to CO2 by offering a source of oxygen atoms [48, 49]. Both effects would be a strongly affected by the arrangement of Ru and Pt on the surface and hence some ability to model segregation under non-vacuum conditions quantitatively can be useful to optimize catalyst activity and CO tolerance. Figure 2-1 shows that oxygen adsorption has a profound effect on the segregation of dilute Ru in Pt. It shows the variation of the energy of nine layer Pt slab ((111) plane with a 3×3 surface unitcell) as a Ru is brought from the center of the slab (where the energy is set to zero) to layers successively closer to a surface in vacuum, or with a monolayer of oxygen adsorbed on the surface. The methodology to compute the energies is discussed in the next section. Oxygen adsorption turns the positive segregation energy for Ru in a vacuum environment (~ +0.6 eV) [50], into a very negative segregation energy (~ −2.0 eV). While these calculations correspond to extreme conditions, they do clearly demonstrate that the environment during processing of material can play a crucial role in the segregation of alloying elements.

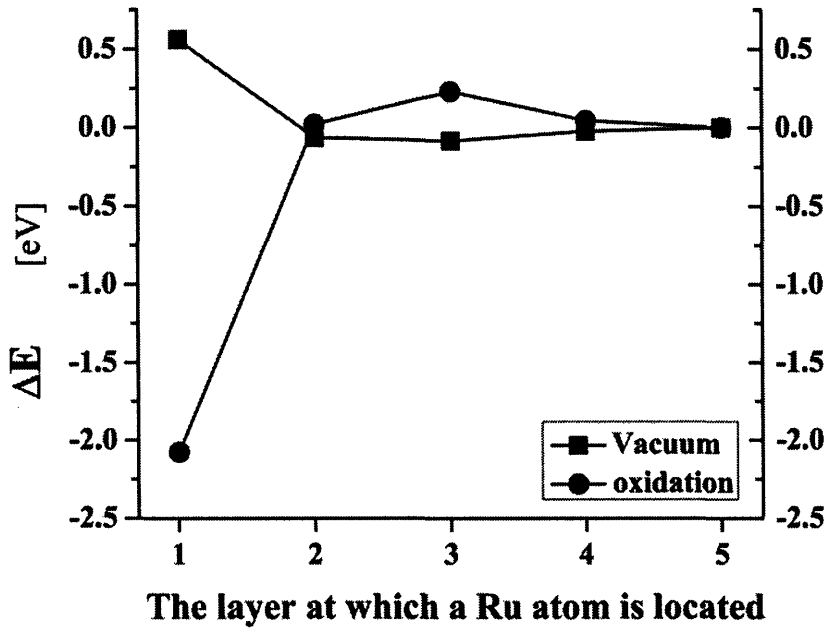

Figure 2-1: First principles energies of a 9 layer of (3×3) Pt (111) slab with one Pt atom replaced by a Ru atom under vacuum or with a monolayer oxygen adsorption. The zero of energy is Ru in the center of the slab (layer 5).

2.3 Model systems and computational methods

To study environments less extreme than vacuum or full oxygen coverage, and to investigate in more detail the interaction between adsorption and segregation we develop a model to predict from first-principles the surface thermodynamics and segregation of alloy surface as a function of adsorbate chemistry and temperature. This model combines density functional theory (DFT) total energy calculations with cluster expansion formalism and Monte Carlo simulations to obtain thermally equilibrated surface structures.

Our surface model consists of three subsystems in contact with each other (Fig. 2-2). The Pt-Ru alloy is modeled as a surface monolayer on top of bulk, which acts as a reservoir with constant chemical potential of Pt and Ru. Each site in this monolayer can be occupied by a Pt or Ru atom. On top of this is a single layer of sites on which adsorbate atoms (oxygen in our case) can be present or not. The adsorbate layer is in chemical equilibrium with an external environment at constant chemical potential of the adsorbate species. The adsorbate layer, surface layer and the bulk all interact. The restriction of a single alloy surface layer and adsorbate layer in which the configuration is varied is not fundamental to the model and can be easily extended to multiple layers though more interactions in the cluster expansion (see below) would have to be determined. The restriction to a single adsorbate layer obviously restricts application of the model to thermodynamic and kinetic conditions, which do not cause adsorbate penetration into the subsurface and bulk (e.g. whole-scale oxidation).

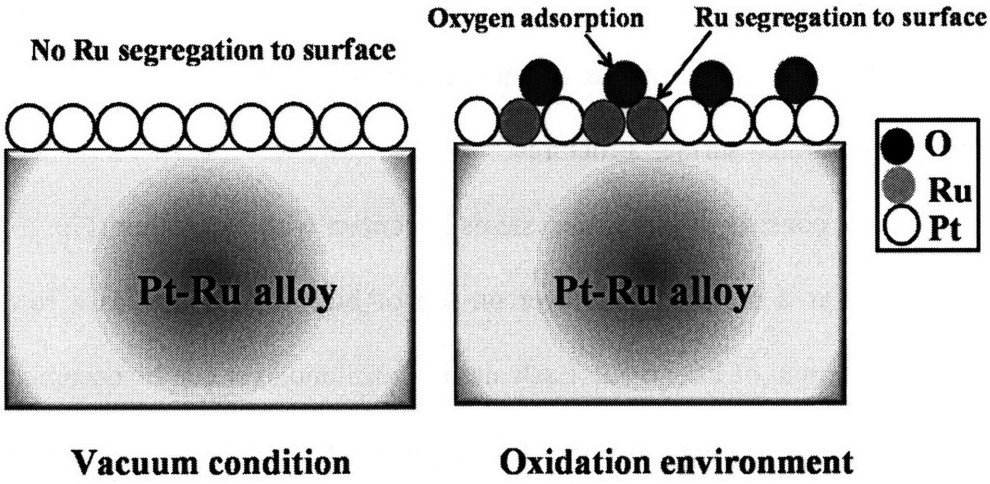

Figure 2-2: Surface model system of adsorbate and Pt-Ru alloy electrocatalysts.

While it is possible to calculate the energy of a few specific arrangements of adsorbates and surface atoms in small unitcells with modern DFT methods, chemical equilibrium requires that samples on a large number of configurations, most of which are not periodic. In alloy theory, well established techniques exist to parameterize the energy of a system with respect to configurational occupation variables and then equilibrate it with Monte Carlo simulation [51, 52]. It involves the use of a cluster expansion to extrapolate accurate DFT calculations for a few arrangements of atoms to the calculation of the energy for any arrangement of atoms over a fixed underlying lattice topology. For a material with binary disorder (e.g. a bulk crystalline A-B solution) occupation variables σ_i can be defined which take on the value (+1) or (−1) depending on whether site *i* is occupied by A or B. A cluster expansion is merely an expansion of the energy of the system in polynomials of these variables.

$$E(\sigma_1, \sigma_2, \dots, \sigma_N) = V_0 + \sum_i V_i \sigma_i + \frac{1}{2}\sum_{i,j} V_{ij}\sigma_i\sigma_j + \frac{1}{6}\sum_{i,j,k} V_{ijk}\sigma_i\sigma_j\sigma_k + \dots \quad (2\text{-}1)$$

These polynomials can be shown to form a complete basis, thereby making the untruncated cluster expansion at least formally an exact representation of the energy (*E*) [51]. It may be worth noting that occupation variables σ_i are only needed on site *i* for which the occupation is variable, but the energy, which is expanded, is the total energy of the system. Hence, when studying segregation to the surface of an alloy, one only needs to expand in the occupation of the first (or first few) layer(s). Since the total energy of the system is expanded, the interaction of these surface layers with the underlying bulk is completely accounted for. This formalism has been used successfully to calculate from first-principles the phase diagrams of a large number of bulk alloys [52-56] and surfaces [57, 58].

For the O/Pt-Ru surface, binary disorder exists both in the alloy surface (Pt or Ru occupation of sites) and in the adsorbate layer (oxygen adsorbed or not) and the results in Fig. 2-1 indicate that the occupation variables in the adsorbate layer are strongly coupled to the occupation of the underlying surface sites. The energy of such a system with two coupled binary disorder subsystems can in all in generality be studied with the coupled cluster expansion [45]. Let the variable $\delta_i = \pm 1$ indicates whether the adsorbate site i is occupied by oxygen (+1) or not (−1), and $\sigma_j = \pm 1$ whether the occupation of surface site j is occupied by Ru (+1) or Pt (−1). The energy of the system can then be expanded in terms of polynomials of both sets of occupation variables

$$E(\sigma_1, \sigma_2, \dots, \sigma_N ; \delta_i, \delta_j, \dots, \delta_N) =$$

$$V_0 + \sum_i V_i \sigma_i + \sum_j V_j \delta_j + \frac{1}{2}\{\sum_{i,j} V_{ij} \sigma_i \sigma_j + \sum_{i,j} V_{ij} \sigma_i \delta_j + \sum_{i,j} V_{ij} \delta_i \delta_j\} + \dots \qquad (2\text{-}2)$$

The expansion contains adsorbate-adsorbate ($\delta_i \delta_j$) interactions, metal-metal ($\sigma_i \sigma_j$) interactions as well as coupling terms ($\sigma_i \delta_j$) between an adsorbate and surface site. Only point and pair terms are shown in Eq. (2-2), but higher order polynomials are also considered, and are indeed essential for convergence of the expansion.

While the cluster expansions (Eq. (2-1) and (2-2)) may seem like simplified models, the completeness of the basis guarantees that the quantity which is expanded can be represented as accurately as one desires. One can think of Eq. (2-1) as an expansion in the product space of the surface and adsorbate configurational space [45].

Cluster expansions are a useful approach to study the configurational space and finite temperature thermodynamics of systems with fixed topology, i.e., the occupation of the sites can change but their connectivity cannot. Formally, it can be shown that the cluster expansion is an explicit form of the Hamiltonian that is obtained by systematically coarse-graining the partition function of a crystalline system [59, 60]. The results of a such a coarse graining procedure is a lattice (or Ising-like) Hamiltonian whose value for a specific configuration gives the free energy obtained by integrating over the non-configurational degree of freedom (e.g., vibrations, electronic excitations). Typically, only the ground state component of their free energy is calculated by placing the atoms on the ideal lattice position and allowing them to locally relax to their lowest energy position. When this ground state energy is cluster expanded and used in a Monte Carlo simulation to simulate finite temperature behavior, the results only include energy and configurational entropy effects. While for most bulk systems this seems to gives high predictive quality and reasonable quantitative agreement with experiment [61], vibrational effects can be included by expanding the vibrational free energy of each configuration [62, 63] rather than the ground state configuration. Neglecting vibrations seems to have little effect when studying equilibrium between phases with similar topology [64] though it has been shown to be critical to estimate bulk phase transition in some cases between phases with very different topology [65].

For the adsorption of atomic oxygen [66-69] we use the *fcc* hollow sites of a (111) surface, as experimental studies have found that these to be more stable than the *hcp* sites on pure Pt(111) [70-72]. Only the top (111) surface layer of the alloy was given variable occupation so that the

adsorbate and surface layer form two coupled triangular lattices on which to perform the coupled cluster expansion.

To parameterize the coupled cluster expansion, the energy was calculated for 127 configurations of Pt-Ru in the top layer and oxygen in the adsorbate layer. All configurations fit in a less than $p(4 \times 4)$ supercell slab of six (111) planes. A vacuum of 14 Å was used in the supercell calculations. The atoms of the top four layers including adsorbate were fully relaxed, while the atoms of the bottom two layers were fixed to their bulk positions. The in-plane lattice parameter was fixed to the calculated lattice parameter of pure Pt, and all layers which are not part of the top surface layers were always pure Pt. Energies were calculated in the Generalized Gradient Approximation (GGA) to density functional theory (DFT) with the Perdew-Wang exchange correlation and Projector Augmented Wave (PAW) pseudo-potentials method was used as implemented in VASP [73]. The Kohn-Sham eigenfunctions were expanded in terms of plane waves with cut-off energy of 325 eV and Brillouin zone integration was performed in on a (21×21×1) *k*-point mesh for a (1×1) surface unitcell and on smaller meshes for larger supercells.

While the cluster expansion is formally an exact representation of the energy quantity that is being expanded, its practical value relies on the fact that a practical truncation limit exists. Which particular polynomials (and therefore which the Effective Cluster Interaction (ECI)) to retain in the expansion was determined by optimizing the cross-validation score of a fit to the calculated DFT energy of the 127 configurations. The cross-validation score is essentially an average measure of how each configuration is predicted when left out of the fit and as such is a measure of the predictive capacity of the expansion [54]. More details on the cross-validation approach can be found in reference 19. Using the cluster expansion equilibrium segregation and

adsorption configurations can be obtained by applying Monte Carlo simulations to the cluster expansion (Eq. (2-2)). We performed the Monte Carlo simulations in the grand canonical ensemble with an applied oxygen chemical potential (determined by the gas partial pressure) and Ru chemical potential (determined by the bulk concentration of the alloy).

2.4 Results

2.4.1 Stable states of the Pt-Ru | Oxygen-Vacancy system

Fig. 2-3 shows the surface layer and adsorbate compositions (marked by squares) at which the energies of different configurations were calculated. The solid triangles that connect some of these points are the projection of the convex hull of the 127 energies. The points that define the convex hull (filled squares) are the adsorbate-surface configurations that are stable with respect to linear combinations of arrangements at other compositions that would give the same composition. Hence, the structures corresponding to the filled squares are the ground states of this (adsorbate/surface-layer) system. All the other structures (open squares) within a triangle are metastable with respect to the structures at the vertices of that triangle and would be able to lower their energy by separating into the structures at the vertices of the triangle they lie. The triangles that make up the ground state map also define all the possible three-phase coexistences at zero absolute temperature.

The slope of energy with respect to the composition of a species gives the chemical potential of that species. Since each triangle is the projection of a bounding face of the convex energy hull, the slopes of this face are the adsorbate and Ru/Pt chemical potentials that keep the three phases in equilibrium. Most of the groundstate structures are on the edges of the composition diagram and only three exist at intermediate compositions (see inset in Fig. 2-3). The ground state map also indicates that pure Pt surfaces partially covered by oxygen coexists with fully oxygen-covered Ru surfaces, indicating that under equilibrium conditions abrupt oxidation of the surface could occur with minor chemical potential changes of oxygen or Ru. We represented surface structures according to Wood's notation [74] and to which we added the oxygen and Ru coverage, i.e., $p(a \times b) - (\theta_1, \theta_2)$ indicate a surface unitcell of dimension a and b with oxygen and Ru surface coverage respectively given by θ_1 and θ_2. A $p(2 \times 2) - (1/4, 0)$ groundstate structure is predicted on pure Pt in agreement with experimental observations using high resolution electron energy loss spectroscopy (EELS) and LEED [75] and with theoretical work [76]. While bulk Pt-Ru alloys tend to phase separate in bulk [77], Fig. 2-3 shows that in a surface layer exposed to vacuum, ordering between Pt and Ru is favored as evidenced by the stable ordered arrangement at $\theta_{Ru} = \frac{2}{3}$. Furthermore, partial oxidation of the surface also tends to stabilize ordered configurations between Pt and Ru within the surface layer (e.g. structure $p(4 \times 4) - (3/16, 1/16)$, structure $p(2 \times 2) - (3/4, 1/4)$ and structure $p(2 \times 2) - (1/4, 3/4)$. As is evident from the inserts showing structure $p(2 \times 2) - (1/4, 3/4)$ and $p(2 \times 2) - (3/4, 1/4)$, there is a strong affinity between oxygen and Ru, with Ru tending to bind oxygen within its nearest neighbor shell. Hence, we can anticipate that oxygen adsorption will attract bulk Ru to the catalyst surface.

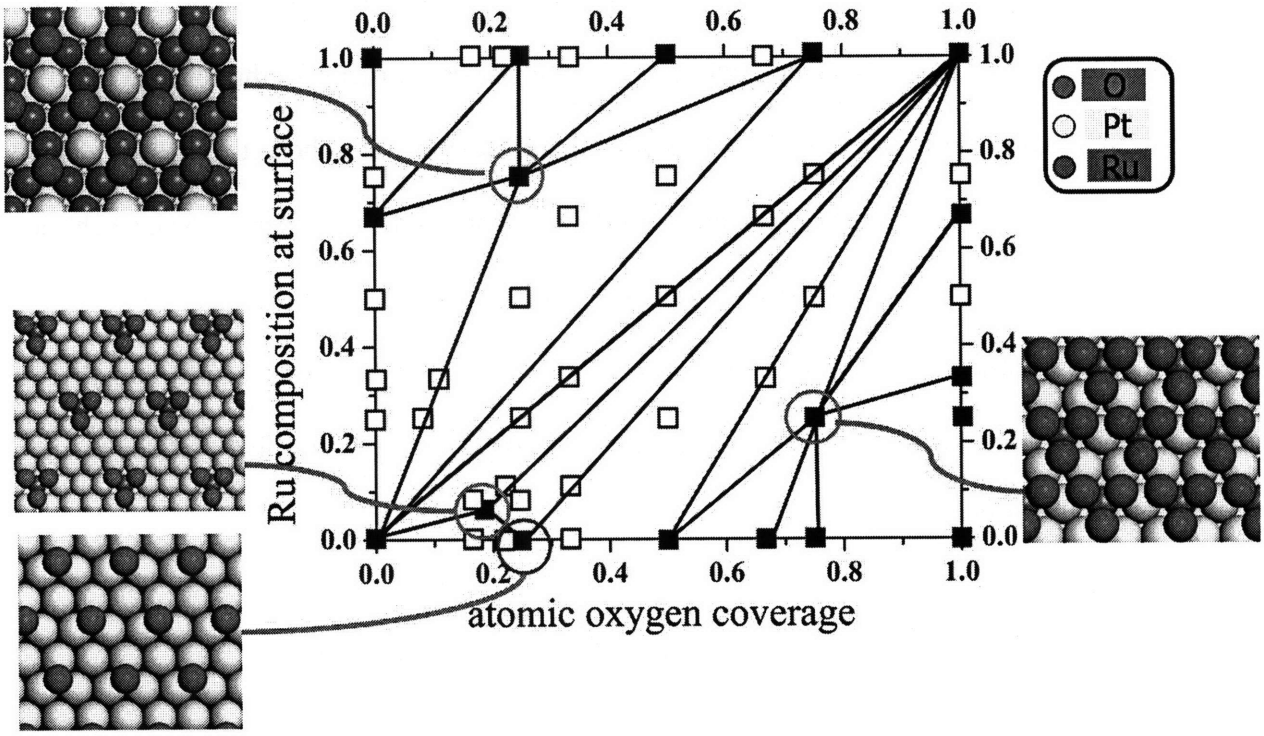

Figure 2-3: Ground state structures of the O/Pt-Ru(111) system. The points marked by squares are combinations of oxygen and Ru surface compositions at which the total energy was calculated. The filled squares represent the ground states that make up the convex hull and are stable against decomposition into other structures. Pictures of four of these structures are inserted.

To investigate the strong attraction between O and Ru, we calculated the charge density change when O adsorbs on the surface (Fig. 2-4). This charge difference plot was obtained by subtracting the charge density of a slab with a particular Pt-Ru arrangement in the surface layer without oxygen coverage from the charge density of the same slab with a monolayer of oxygen on the surface. For this particular purpose, no relaxations were allowed so that charge densities could be subtracted point by point. Such a plot therefore illustrates how the charge density changes as a result of oxygen adsorption. The dark regions indicate where oxygen subtracts charge. Fig. 2-4(b) shows the variation with distance of the difference charge density integrated within a sphere around Pt and Ru respectively. As is clear from both Fig. 2-4(a) and (b), Ru donates more charge to the adsorbed oxygen than Pt consistent with the fact that Ru is more easily oxidized that Pt.

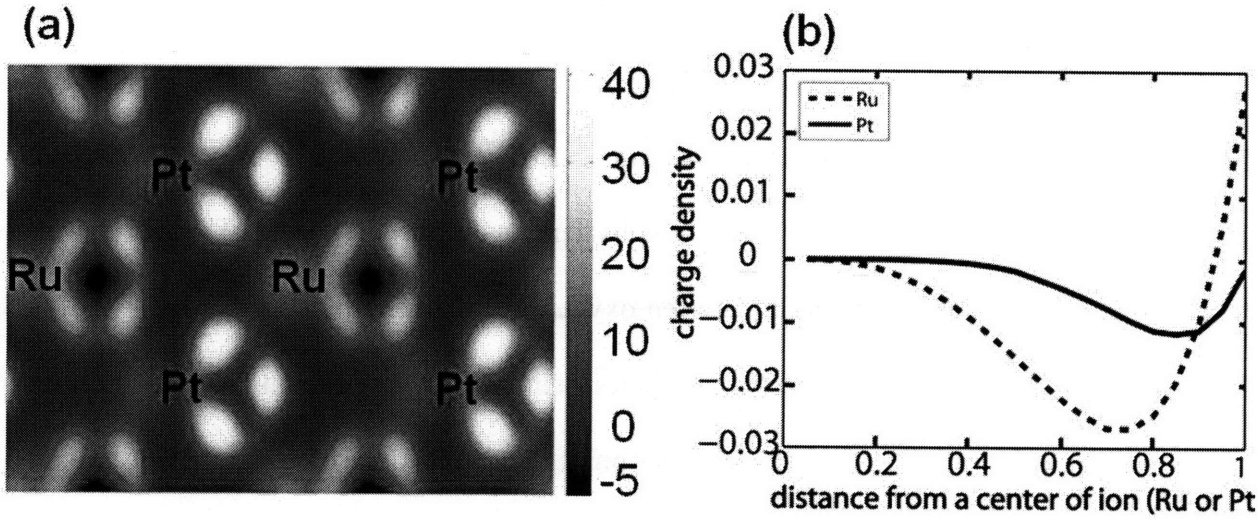

Figure 2-4: Difference in charge density of a fully oxidized and fully reduced $Pt_{0.5}Ru_{0.5}$ surface (Ru and Pt are arranged in lines) in (a). Graph (b) illustrates integral of the charge density difference around Pt (solid line) and Ru (dashed line) as a function of radius of the charge sphere.

2.4.2 Coupled Cluster Expansion (CCE)

To study the O/Pt-Ru system at finite temperature a coupled cluster expansion was derived from the 127 ab-initio energies. The cluster expansion optimized with cross validation contains 40 terms, each corresponding to a cluster of sites (e.g. pair cluster, triplet cluster etc), and reproduces the DFT energies with a root mean square (rms) error of 8 meV per surface site. The Cross Validation (CV) score of the cluster expansion, which is a measure of its predictive accuracy, is 15 meV. The values of the effective interaction coefficients (ECI) are given in Table 2-1 along with a figure of each cluster in Fig. 2-5. The nearest neighbor pair between an adsorption site and a surface site (cluster 5) is by far the largest interaction. The fact that it is negative reflects the strong attraction between oxygen and Ru (since for oxygen, $\delta_i = +1$, and for Ru, $\sigma_i = +1$). The cluster expansion includes pair interactions extending up to the fourth nearest neighbor. Note that ECI for several four point clusters (i.e. cluster 57 and 58, see Fig. 2-5 and Table 2-1) are relatively large, indicating they are essential to the convergence of the cluster expansion. The pure adsorbate terms are positive and decay well with distance, indicating repulsive interactions between oxygen on the surface. The Pt-Ru interactions in the surface layer are all small and positive indicating very weak ordering tendencies in the surface layer.

While it is difficult to make definite statements about the energetics of the system by inspecting the pair ECI, given that there are also triplet and quadruplet ECI present, Table 2-1 does give some indication that the structure of this system will be determined by a competition between the adsorbate-adsorbate and adsorbate-surface interaction, with the Pt-Ru interaction in the surface playing a small role.

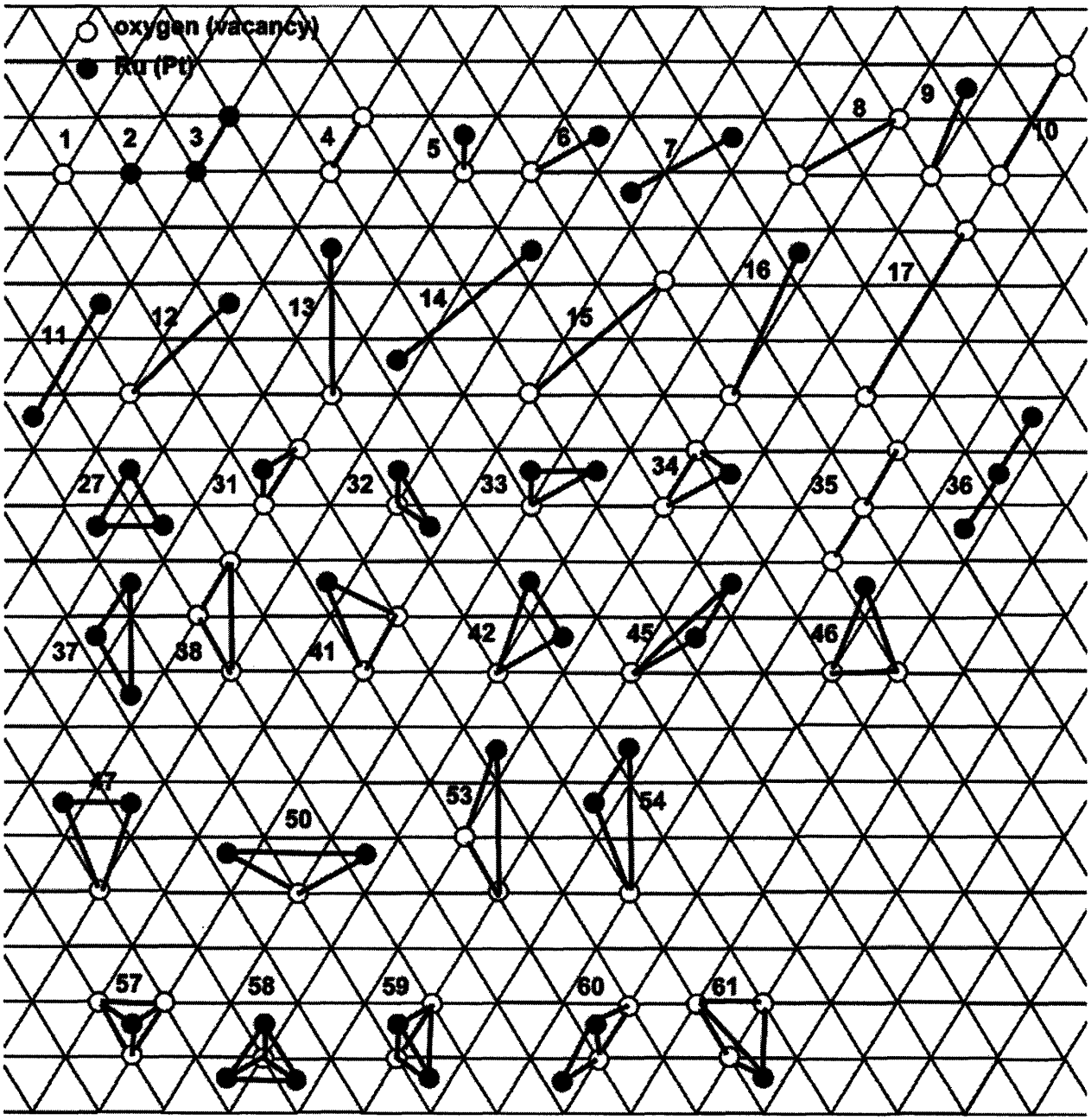

Figure 2-5: Effective interactions used in the coupled cluster expansion. The oxygen adsorption sites (open circle) sit on the points of the triangular lattices, while the alloy surface layer sites (solid circle) form another triangular lattice connecting the centers of half the triangles.

Table 2-1: Effective Cluster Interaction coefficients (ECIs). Table 1a gives the ECI for non-coupled clusters and Table 1b gives the coupled clusters between adsorbate sites and alloy surface sites. A "NN" indicates "Nearest Neighbor site".

(a) ECI of non-coupled clusters			
geometry		cluster number in Fig.2-5	ECI [meV]
pair clusters	1st NN	4	37.6
		3	4.7
	2nd NN	8	11.1
		7	3.2
	3rd NN	10	4.7
		11	4.5
	4th NN	15	6.2
		14	-0.5
	5th NN	17	6.3
triplets		35	2.0
		38	-1.4
		27	-9.8
		36	2.5
		37	1.6
(b) ECI of coupled cluster			
geometry		cluster number in Fig.2-5	ECI [meV]
pair clusters	1st NN	5	-152.7
	2nd NN	6	3.1
	3rd NN	9	-17.5
	4th NN	12	-0.3
	5th NN	13	-4.8
	6th NN	16	-2.2
triplets		31	-13.8
		32	8.8
		33	-7.0
		34	-4.0
		41	2.4
		42	13.1
		45	-10.5
		46	-7.1
		47	-6.3
		50	-1.9
		53	-1.7
		54	6.8
quadruples		57	-15.8
		58	-11.7
		59	4.8
		60	-4.5
		61	2.2

2.4.3 Monte Carlo Simulation of Finite Temperature Behavior

The surface structures were thermally equilibrated at fixed Ru and O chemical potential by applying Monte Carlo simulations to the coupled cluster expansion in a grand canonical ensemble. The constant Ru chemical potential condition simulates the bulk acting as an infinite reservoir for Ru. While the equilibrium configurations obtained in Monte Carlo simulations are independent of the reference value for the chemical potentials, it is instructive to relate the oxygen chemical potential to an oxygen partial pressure. This can be done through the standard activity equation

$$\mu_0(T,P) = \mu_0^o(T,P^o) + \frac{1}{2}kTlog_e\left\{\frac{P_{O2}}{P^o}\right\} \qquad (2\text{-}3)$$

In Eq. (2-3) the oxygen gas is treated as ideal and $\mu_0^o(T,P^o)$ is a reference chemical potential at temperature (T) and pressure (P^o). To find the values for $\mu_0^o(T,P^o)$, we fit our oxygen coverage results for a pure Pt surface to the experimental data at $T = 726\ K$ obtained by Derry and coworkers [78] who measured the oxygen adsorption isotherm for pure Pt as a function of partial pressure and coverage. The reference $\mu_0^o(T,P^o)$ at other temperatures was extrapolated from $T = 726\ K$ with the analytical free energy function of O_2 gas which includes independent rotational, vibrational and translational degrees of freedom, as for example, given by Hill [79]. Table 2-2 gives the values of the O_2 gas as a function of temperatures. This reference chemical potential contains any energetic offsets between calculation and experiment (either from GGA error or from different choices of reference state) as well as some entropic effects not accounted for in the calculation. The latter is mainly the entropic loss when oxygen goes from the molecule in the gas to the adsorption site. Note that μ_0^o does not need to fit configurational entropy effects

for the adsorbate on the surface, as these are explicitly included in the Monte Carlo simulation. Since the entropic effects in μ_0^o are dominated by the entropy in the gas phase with some contribution from vibrational entropy on the surface, we believe that it should be independent of surface details and therefore transferable from pure Pt surfaces to the Pt-Ru surfaces in our simulation.

Table 2-2: Reference chemical potentials at temperature (T) and pressure (P^o).at temperature from T=100 K to 1100 K. These values are obtained from a fit our to Monte Carlo simulation results on pure Pt and oxygen to experimental data at T = 726 K. The values at other temperatures were calculates by the analytical free energy function of a oxygen gas.

T (K)	$\mu_O^o\ (T, p^o)$	T (K)	$\mu_O^o\ (T, p^o)$
100	775.2	700	-216.3
200	637.1	800	-405.4
300	483.1	900	-598.8
400	318.8	1000	-796.3
500	146.6	1100	-997.3
600	-32.1	1200	-1201.6

Fig. 2-6 shows the oxygen coverage obtained by Monte Carlo simulation as a function of oxygen chemical potential on pure Pt(111) at $T = 726K$. An approximate relation to oxygen partial pressure scale is made with Eq. (2-3) and Table 2-2. Our calculation correctly reproduce that at about $10^{-10} \sim 10^{-5}$ (atm) adsorbed oxygen orders into a $p(2 \times 2)$ structure [75, 80].

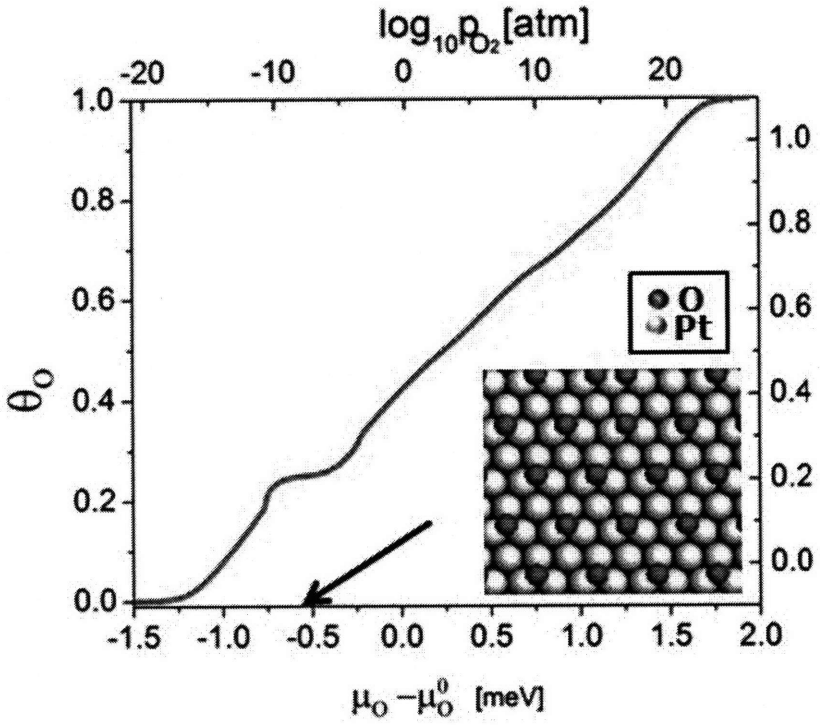

Figure 2-6: Calculated oxygen coverage on a pure Pt(111) surface at T= 726K. The chemical potential (bottom scale) has an arbitrary reference. An approximate oxygen partial pressure (top scale) is given for guidance. The insert shows the stable surface structure at $\theta_O = 0.25$.

Since the coupled cluster expansion describes the oxygen adsorption energetics and the surface segregation energetics, as well as the interaction between them, it is possible to equilibrate both surface segregation in Pt-Ru and oxygen adsorption simultaneously, and find the true equilibrium states of this system as a function of the chemical potential. Fig. 2-7 (a) and (c) show equilibrated oxygen isotherms at two different temperatures, $T = 600$ and $1050\ K$, and Ru chemical potentials (-1750 and -665 meV). The horizontal axis corresponds to the oxygen chemical potential and the vertical axis denotes the oxygen concentration (open squares) on the adsorbate lattice and the Ru concentration (filled triangles) in the surface layer. At low Ru chemical potential (see Fig. 2-7 (a)), the oxygen concentration only gradually increases, inducing only a slight enhancement of Ru segregation to the surface. As can be seen in the insets, which represent snapshots from the Monte Carlo simulation, the segregated Ru atoms are always bound to adsorbed oxygen atoms. As the oxygen chemical potential increase further, both the oxygen concentration and Ru segregation increase until a full oxygen-covered Ru surface is obtained. Fig. 2-7 (c) represents a similar simulation as Fig. 2-7 (a) but at higher Ru chemical potential and at different temperature.

A comparison of Fig. 2-7 (a) with (c) shows that the concentration trajectory changes as the Ru chemical potential increases. At low Ru chemical potential (Fig. 2-.7 (a)), the oxygen coverage is always larger than the Ru concentration in the surface layer. However, at higher Ru chemical potential (corresponding to a larger Ru bulk concentration), the Ru concentration at the surface exceeds the oxygen concentration once a threshold oxygen chemical potential is surpassed. Both results (Fig. 2-7 (a) and (c)) show that under a high enough oxygen partial pressure, Ru will segregate to the surface. While at low Ru chemical potential (Fig. 2-7 (a)),

oxygen adsorption gradually induces Ru segregation, at high Ru chemical potential (Fig. 2-7(c)), the oxygen adsorption and Ru segregation are strongly coupled, occurring suddenly at a critical oxygen chemical potential. Fig. 2-7 (b) and (d) show the Monte Carlo simulation results of system (a) and (c) respectively at the same temperature and oxygen chemical potential conditions but this time on a pure Pt surface. As is clear from the comparison of Fig. 2-7 (a) and (b), or Fig. 2-7 (c) and (d), Ru facilitates oxygen adsorption and increases the oxygen coverage dramatically.

The insets in Fig. 2-7 illustrate that the surface microstructure (ordering between Pt and Ru in the surface layer) changes with temperature and chemical potential. At low oxygen chemical potential, only isolated Ru atoms segregate to the surface. At higher oxygen chemical potential, the Ru atoms that segregate to the surface cluster together, resulting in a surface pattern consisting of islands of Pt surrounded by regions of Ru. At low Ru chemical potential (Fig. 2-7(a)), the Pt islands are still interconnected, while at higher Ru chemical potential (Fig. 2-7(c)), the Pt islands are isolated.

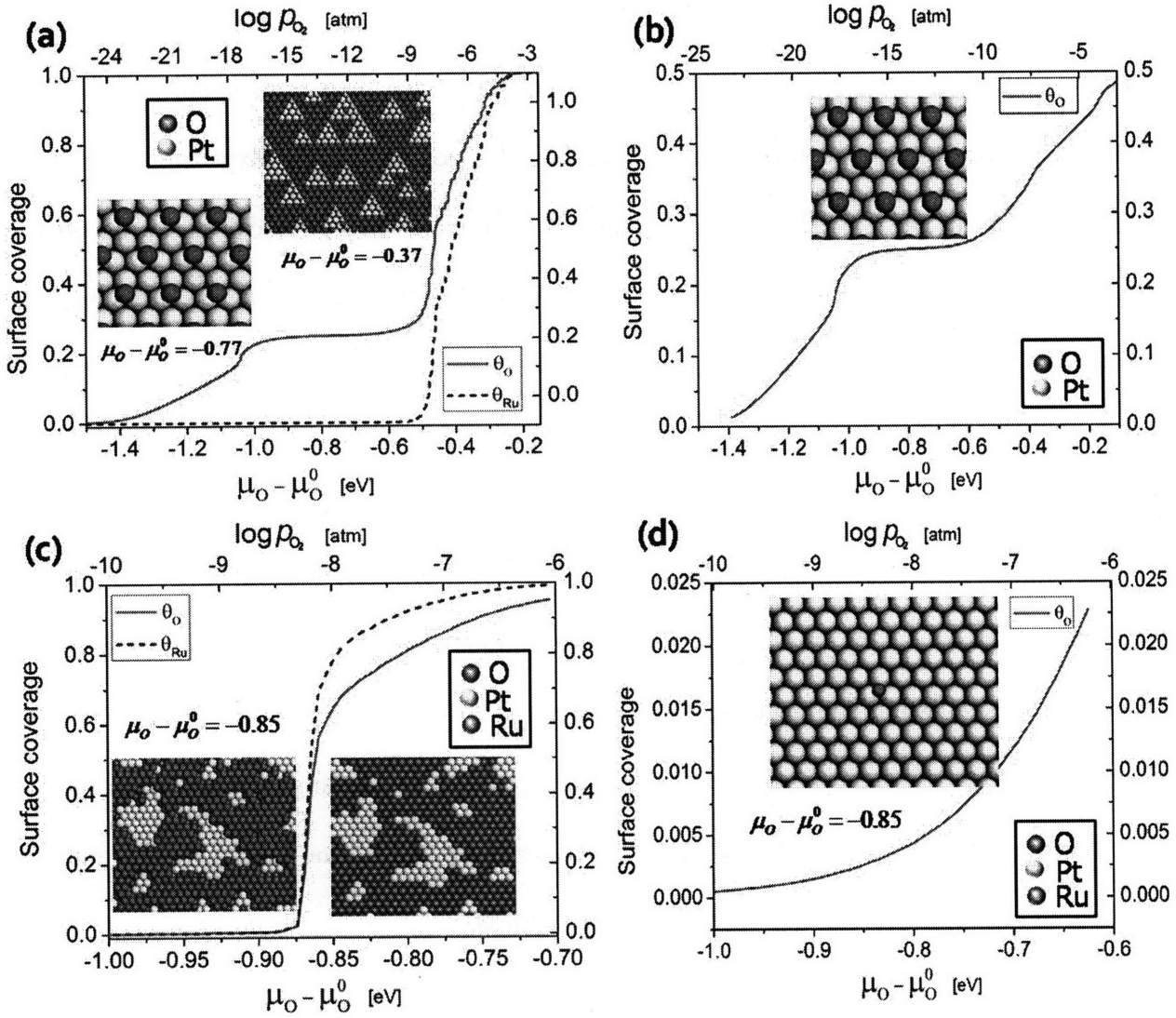

Figure 2-7: Monte Carlo Simulations and surface structures as a function of oxygen chemical potential, temperature and bulk Ru composition (C_{Ru}). The conditions of (a) are at T = 600 (K), μ_{Ru} = -1750 meV and (c) are T = 1050 (K), μ_{Ru} = -665 meV. The Figures (b) and (d) are equilibrated oxygen isotherms at T = 600 (K), and T = 1050 (K) in pure Pt surfaces with oxygen adsorbates.

2.5 Discussion

We have presented an approach to study surface segregation and adsorption simultaneously. By expanding the energy of the system into occupation variables describing the surface and adsorbate sites we can include, without bias, adsorbate-adsorbate, adsorbate-surface and alloy interactions on the same footing. The advantage of this coupled cluster expansion is that it is formally rigorous since the basis set of expansion functions (the products of the occupation variables) forms a complete set, and its form is independent of the model used to calculate energies of specific surface structures. The choice of clusters and the truncation of the expansion can be optimized through statistical methods such as the cross-validation approach used here [54], though other schemes have also been proposed [81]. As such the coupled cluster expansion can be a Hamiltonian with all the accuracy of the ab-initio DFT method by which it is parameterized, but can be evaluated orders of magnitude more faster, making it amenable to Monte Carlo simulation and accurate finite temperature statistics. It is worth pointing out that simpler models in the same spirit and with the same purpose of studying the interaction between adsorbate and alloy segregation have already been developed [82]. One should see our approach as a more formal and generalized extension of these ideas.

In the Pt-Ru system, we find a large effect of the adsorbate on the surface segregation in the alloy. While Pt has the lowest surface energy in vacuum and is expect to fully saturate the surface layer at reasonable temperature, the segregation is significantly modified in the presence of oxygen. The strong binding between Ru and O on the surface more than overcomes the higher surface energy of Ru. We find that even at low Ru and oxygen chemical potentials, oxidized islands of Ru coexist with bare Pt on the surface. These island structures are sustained up to very

high temperature. At lower temperature and higher Ru chemical potential the combined segregation of Ru to the surface and oxygen adsorption is a collective effect occurring at a critical oxygen chemical potential. Hence, one can think of this as an adsorbate induced segregation transition.

The island structures that form in our simulation may be important for catalysis, as at the edges of the Ru-O islands, both Pt sites for decomposition of methanol and O for the oxidation of CO are available. This is the bi-functional catalyst mechanism which has been proposed in the literature to explain the tolerance of Pt-Ru catalysts to CO [83]. If this is the case, control of the size and structure of the islands would be critical to the catalytic performance of these materials.

Because oxygen adsorption on the surface induces Ru segregation, processing and operating conditions will play an important role in determining the surface structure and composition. Materials formed at temperatures where there is metal atom mobility are likely to have Ru-rich surfaces unless very reducing conditions are used. How this determines the surface of a practical catalyst is unclear as the latter are often washed in mild acids before use, which may remove oxidized species.

In typical fuel cell operation, several possible species can adsorb on the catalyst. Using a simpler model Christoffersen et al. [82] already pointed out that several adsorbed species could induce alloy surface segregation. While typical operating temperatures of fuel cell electrodes are relatively low, it is possible that adsorbate induced segregation and subsequent dissolution of alloying elements contribute to the degradation of catalysts during operation.

On the other hand, surface oxide formation (RuO_2) may also play beneficial roles as it has been shown to enhance particle dispersion of Pt and Ru particle by reducing the degree of

sintering during the electro-catalyst manufacturing. Recently it has been speculated that TiO_2 also plays a similar role in the PtRu nano particles [84, 85].

Finally, it might be possible to use adsorption-induced segregation to pattern surfaces. Our ground state calculations show that ordered structures of Ru(surface) - O(adsorbate) exist for certain ranges of oxygen and Ru chemical potential. These could be formed by long annealing of alloy surfaces under the proper chemical conditions. A short reduction treatment would then remove the surface adsorbate and leave an ordered Ru-Pt surface behind.

When comparing our calculation to experiments several limitations should be kept in mind. We only study the equilibrium states in the O/(Pt-Ru) system and sufficient mobility of Ru through the alloy bulk may be required to allow Ru to diffuse to the surface. Many practical alloy catalysts are prepared through a serious of low to medium temperature processes to retain their small particle size, and their surface structure may be neither chemically nor structurally equilibrated. In addition, our study focused on a (111) surface, and nano-scale catalysts may have multiple crystallographically different planes.

The other assumption in our work is that adsorbates do not penetrate into the bulk alloy, or Ru does not form a separate oxide phase on the Pt surface. Our model may therefore only be a reasonable approximation in the early stage of oxidation.

Although our methodology was applied to Pt-Ru (111) surfaces in the presence of adsorbed oxygen, it can obviously be applied to other alloys, adsorbates, or surface facets. The important advantage of our coupled cluster expansion is that it offers a general and unbiased approach to study the equilibrium structure in surface-adsorbate problems from first principles. While this makes it possible to calculate surface-adsorbate phase diagrams, the coupled cluster expansion

could also be coupled to kinetic Monte Carlo models to study the kinetic evolution of these interesting systems. Such approaches have already been implemented to study diffusion in bulk systems [86, 87].

2.6 Conclusions

We developed and implemented a formalism to study the equilibration of alloy surfaces under a chemical field of adsorbates at finite temperature. Our methodology combines ab-initio DFT with finite temperature Monte Carlo, connected through the coupled-cluster expansion approach originally developed to study coupled cation/anion disorder in oxides. We applied our methodology to Pt-Ru(111) surfaces and investigated how the surface structures evolve as function of oxygen chemical potential. It is demonstrated that oxygen adsorption can change the surface composition dramatically. Ru is brought to the surface from the bulk by adsorbed oxygen and forms island structures. Hence, oxygen can be used as an adsorbate to control the surface morphology during processing of catalysts.

Chapter 3

The Effect of Coadsorption and Ru-Alloying on the Adsorption of CO on Pt

3.1 Overview

In this chapter, the chemical factors influencing the chemisorption energy of CO on a Pt(111) surface are investigated with first principles DFT calculations. Coadsorption of O and OH, as well as alloying of Ru is investigated. It is shown that coadsorption of CO with either O or OH on Pt weakens the strength of the Pt-CO bond, through largely surface relaxation and strain mediated interaction. Alloying Pt with Ru on the surface slightly enhances the adsorption energy of CO relative to that of pure Pt. However, once Ru is oxidized by O or OH the adsorption energy of CO on a neighboring Pt is dramatically reduced. These findings as well as some information on the competitive adsorption behavior are discussed in the context of designing CO-tolerant Pt catalysts.

3.2 Introduction

The oxidation of CO is a key aspect of low temperature fuel cell operation. CO can exist as an impurity in the fuel itself (e.g. in a Proton Exchange Membrane Fuel Cell) or be produced in the process of fuel oxidation (e.g. in a Direct Methanol Fuel Cell) [48, 88, 89]. These CO molecules bind strongly to Pt and poison the catalyst by removing sites that can participate in the catalysis. In general, alloying Pt with other metals tends to improve the CO tolerance of the catalyst, and one of the most effective alloys is Pt-Ru [90]. The effect of alloying on the CO tolerance of Pt is likely to be complex though some facets of it are understood. CO is removed from the surface by oxidation to CO_2, and the activation barrier for a reaction between CO and an adsorbed oxidant on the surface has been found to depend directly on the adsorption energy of both species [91-94]. Hence, it is critical to understand the adsorption energies of the species under complex conditions, such as segregation of alloying elements and coadsorption of other species. Several groups have focused on the direct changes in the Pt-CO bond strength when Ru is nearby in the surface layer. While it is known experimentally that alloying Ru reduces the CO poisoning of Pt electrodes [90, 95-98], first principles calculations point to a complex picture: A computational study performed by Ge et al. [99] indicates that the CO adsorption energy decreases (i.e. binds less strongly) on the surface of a bulk Pt-Ru alloy, but increases when Ru is only present in the surface layer of an otherwise pure Pt bulk material. Furthermore, they argued that the surface strain induced by the size mismatch of Pt and Ru increases the adsorption energy for CO on Pt, when Ru is present nearby in the surface layer. While instructive, it is not clear that such pure surface calculations are relevant to fuel cell operation conditions where various chemical species such as CO, O_2, O, OH and H_2O are available to adsorb on the surface. As

shown in the previous section (chapter 2 of this thesis), under most practical conditions Ru on the surface of Pt-Ru alloys is oxidized and this oxidation can even drive the segregation of Ru to the surface [100]. A limited amount of work has been done on the effect of coadsorption of other species on the Pt-CO bond strength [92, 101-104]. Bleakely et al. [104] concluded from first principles density functional theory studies that the interaction between CO and O on a Pt(111) surface is localized and that there is no bonding competition between CO and O on the Pt(111) surface. Our work shows somewhat different results and indicates stronger and more long-range coadsorption effects through the relaxations that adsorption induces in the surface layer not considered by Bleakely et al. There is considerable evidence that coadsorption and oxidation of the surface modifies the CO oxidation rate significantly [91, 105-107]. In a key paper, Hendriksen et al. [107] observed experimentally that CO oxidation on pure Pt becomes faster as the O_2 pressure is increased. In addition, oxides have considerably better CO oxidation properties than metals [91, 108]. We investigate the effect of Ru alloying, and coadsorption of O and OH on the CO adsorption energy on Pt. We find that adsorption of O or OH weakens the Pt-CO bond strength. On the other hand, alloying Ru in the bare surface layer of Pt(111) slightly enhances or leaves the CO adsorption energy on Pt unchanged. However, the adsorption of OH or O on the surface Ru atoms (common in most environments) reduces the CO adsorption energy on Pt considerably. Hence, the adsorption energy of CO on Pt is a complex function of the environment.

3.3 Model and Methodology

Adsorption energies are calculated on the slab model similar to the previous chapter: a six-layer *fcc* slab of Pt or (Pt-Ru) atoms with a (111) surface. Periodic boundaries are imposed with varying periodicities in the surface layer. The slab is augmented with 14 Å of vacuum (equivalent to the thickness of six-layer slab) perpendicular to the surface, and periodic boundary conditions are imposed on the (slab + vacuum) unit. The atoms of the top four layers and adsorbates are fully relaxed, while the atoms of the bottom two layers are fixed to their positions in the pure Pt(111) slab. All DFT energies were calculated with the Projector Augmented Wave (PAW) method [73, 109] using the Generalized Gradient Approximation (GGA) with Perdew-Wang exchange correlation functional [110, 111] as implemented in VASP [112, 113]. These pseudopotentials and exchange correlation functional give a calculated lattice parameter of 3.98 Å for bulk *fcc* Pt which agrees reasonably well with the experimental value of 3.92 Å [114]. A plane wave basis set with cut-off energy of 325 eV was used. Reciprocal space integrations were done on a 21×21×1 grid for a (1×1) surface unit cell and proportionally smaller meshes for larger supercells. All adsorption energies are calculated with respect to the atom/molecule in vacuum, unless otherwise stated. Fig. 3-1 shows the different adsorption sites on a Pt(111) surface.

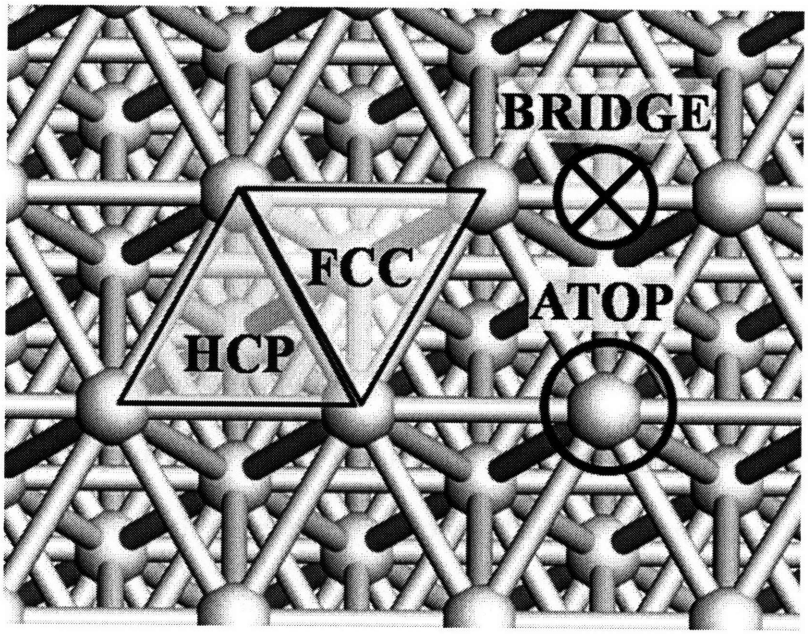

Figure 3-1: Relevant adsorption sites on a Pt(111) surface

3.4 Results

3.4.1 Coadsorption of CO and O

Experimentally, CO has been observed to form *p(4×4)* or *p(8×8)* structures on Pt(111) at low CO coverage [115], but a *p(2×2)* cell has been found to provide enough dilution to approximate the adsorption energy of an isolated CO molecule [67, 116]. Hence, the adsorption of CO on a Pt(111) surface was studied in a *p(2×2)* surface unit cell. The surface geometry of Pt(111)–*p(2×2)*–CO is shown in Fig. 3-2.

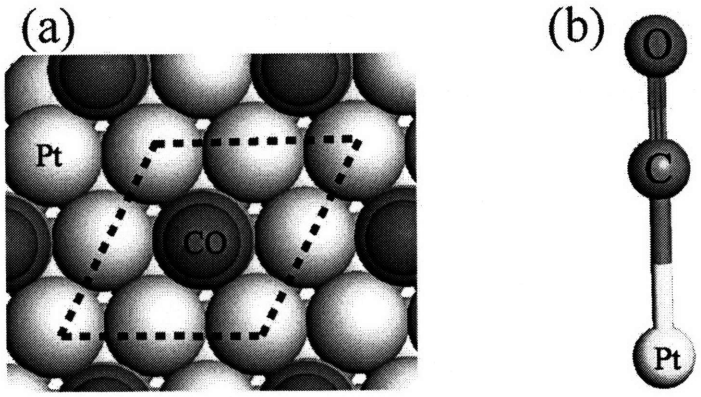

Figure 3-2: Surface geometry of a Pt(111)–*p(2×2)* surface unit cell (dashed line) with CO at the *atop* site: a top view of the surface in (a) and in (b) a lateral view for a bond of CO-Pt.

The adsorption energy for CO is calculated on the *atop* site (see Fig. 3-1), where CO is observed experimentally to adsorb [115, 117], even though it is not the most stable site in the GGA approximation [118, 119]. The chemisorption energy (E_{ad}^{chem}) for an adsorbate (*ad*) is defined as

$$E_{ad}^{chem} = \left[E_{ad/Pt} - E_{Pt(surface)} - E_{ad}\right] \tag{3-1}$$

where E_{ad} is the energy of the isolated molecule in a supercell of dimension (8×8×1). Our results in Fig. 3-3 for CO on pure Pt(111) ($E_{ad}^{chem} \approx -1.75$ eV) agree well with previous calculations [119] and with experimental data [120]. Atomic oxygen was placed in various sites but only found to be stable in the *fcc*, *hcp* and *atop* sites. The oxygen atom is unstable at the bridge site and slides off to the *fcc* site. We find that the *fcc* site is preferred for oxygen with an adsorption energy of about 0.5 eV referenced to atomic oxygen in vacuum, which is in good agreement with other experimental [121, 122] and theoretical investigations [123-125] (Fig. 3-3a) .

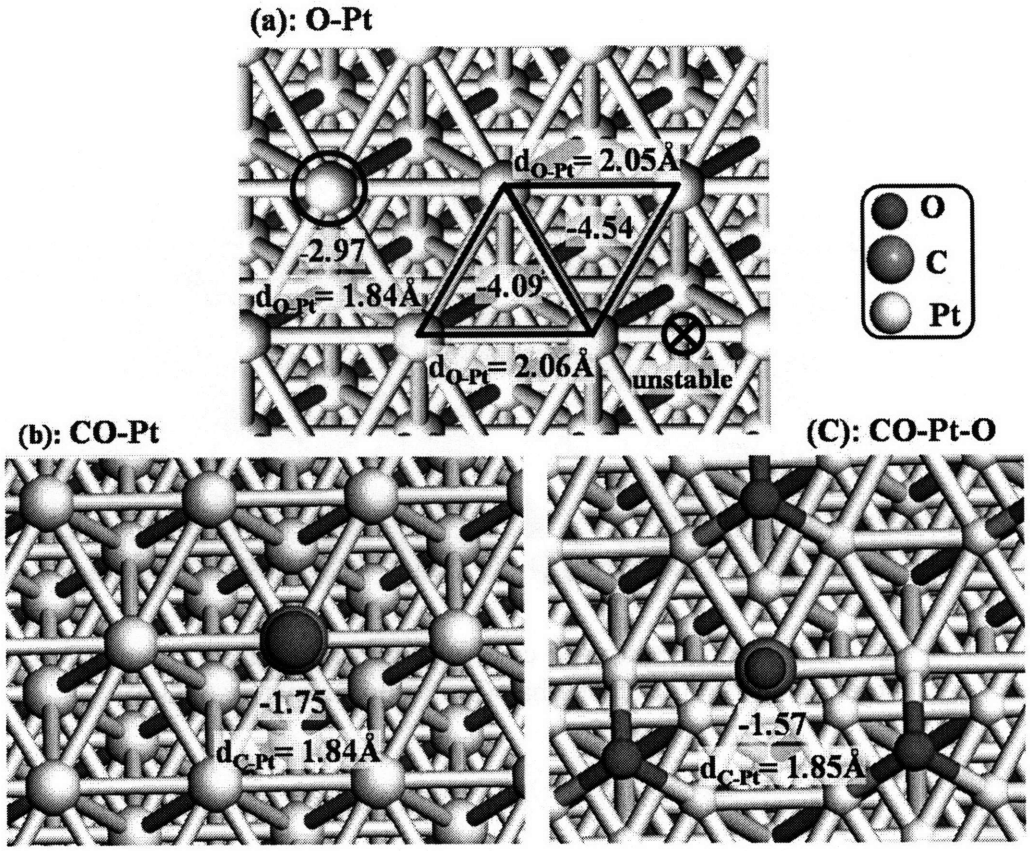

Figure 3-3: Adsorption energy of O in (a), and CO without (b) and with (c) a co-adsorbed oxygen. For CO-Pt, experimental data (in parenthesis) are also given for comparison. The adsorption energies and bond lengths are in unit of [eV] and [Å] respectively.

To study O and CO coadsorption in a *p(2×2)* cell, two geometries are possible (Fig. 3-4(a) and (b)). We chose the configuration displayed in Fig. 3-4(a), as it is energetically more favorable by approximately 0.63 eV than that in Fig. 3-4(b).

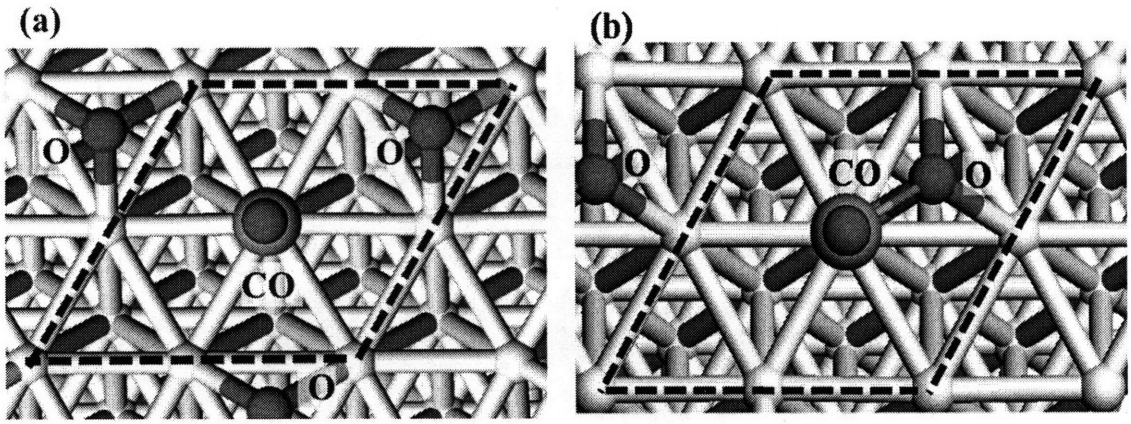

Figure 3-4: Two possible geometries for the coadsorption of CO and O in a *p(2×2)* supercell (dotted line). The structure (a) is more stable than (b) by approximately 0.63 eV.

The CO adsorption energy in the presence of adsorbed oxygen (Fig. 3-3(c)) is reduced from its value for a pure Pt surface (Fig. 3-3 (b)). The reduction we find (~ 200 meV) is considerably larger than what has been found by Bleakely et al. (~ 40 meV) [104]. We believe this discrepancy is due to the different computational approximations. Bleakely et al. did not relax Pt atoms as CO and O adsorb, while all Pt atoms in the top four layers of our six-layer slabs are fully relaxed. The significance of surface relaxations in the coadsorption energy shift can be seen by comparing Fig. 3-5 (a) (only CO adsorbed) with Fig. 3-5 (b) (CO and O coadsorbed). In Fig. 3-5 (a) the Pt atom on which CO adsorbs is pulled out from the surface by about 0.13 Å with respect to the bare Pt (having no CO). However as O coadsorbs with CO (Fig. 3-5 (b)), less surface corrugation occurs since oxygen adsorbed on the *fcc* site pulls up Pt around it by 0.10 Å and CO displaces Pt by only 0.13 Å with respect to the bare Pt. Hence, under coadsorption the surface tends to be flatter.

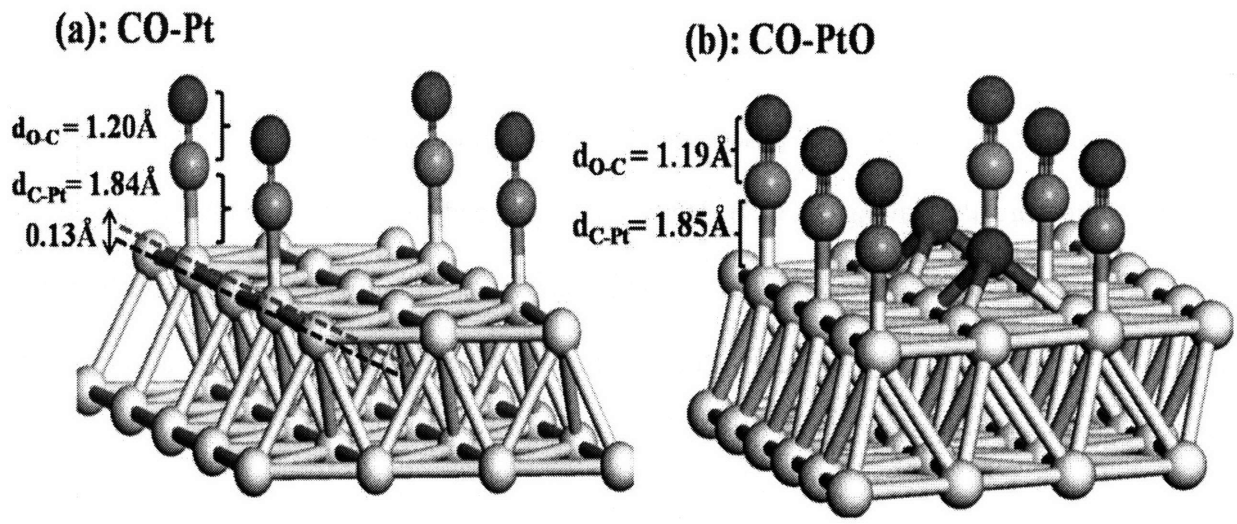

Figure 3-5: The surface structures of Pt(111)-*p(2×2)* with only adsorption of CO in (a) and coadsorption of CO and O in (b). The coadsorption of CO and O reduces the surface corrugation.

To evaluate more in detail the effect of relaxation on the coadsorption Table 3-1 illustrates the adsorption energies of CO for relaxed, and unrelaxed three-layer Pt(111) slabs (the same model system as that of reference [104]. Without surface relaxations, the CO adsorption energies on the Pt(111)-p(2×2)-O surface differ from the clean Pt(111) only by 70 meV. However, once the top surface is allowed to relax, the difference increases to approximately 170 meV. Hence, coadsorption of CO and O decreases the adsorption energy of CO with respect to the clean Pt(111) regardless of the surface relaxation. However, with surface relaxation, the bond strength of Pt-CO is much weaker and the coadsorption effect is enhanced. Thus, we find that the effect of surface relaxations is important in mediating the interaction between adsorbates.

It is notable that even though oxygen coadsorption reduces the energy for CO adsorption by almost 0.2 eV, the (C-Pt) bond distance is practically unaffected by the O-adsorption. This result is consistent with the recent explanation that different orbitals are involved in for controlling the bond length and stiffness of Pt-C-O than for the adsorption energy [126] and similar to what has been observed in the combined cyclic voltammetry and NMR study of Lu et al. [127] who observed that the changes in electronic structure of the CO-Pt bond and its bond strength were somewhat independent. The lowering of the CO adsorption energy that we find when oxygen co-adsorbs is in agreement with the experimental observation that the CO oxidation rate increases under oxidizing conditions [107].

Table 3-1: Effect of O coadsorption on chemisorption energy of CO (E_{ad}^{chem}) with and without surface relaxation. With surface relaxation the bond strength of CO-Pt is weakened (~170 meV) more than without relaxations (~70 meV).

all Pt atoms are fixed			Pt atoms on the top layer are allowed to relax		
ΔE_{ad}^{chem} [meV]	d(C-Pt) [Å]	d(C-O) [Å]	ΔE_{ad}^{chem} [meV]	d(C-Pt) [Å]	d(C-O) [Å]
+76	1.86	1.20	+173	1.84	1.20

3.4.2 Coadsorption of CO and OH

A hydroxyl group (OH) is another important chemical species in the oxidation of CO. It is observed experimentally as an intermediate of water dissociation on the Pt-electrode [128, 129]. Within the context of the bi-functional mechanism, it plays an important role as an adsorbate facilitating CO oxidation by providing a source of oxygen on the surface. A *p(2×2)* supercell was used to study OH (coverage = 0.25) adsorption, which is similar to the cell choice in previous work [68, 128, 130]. All degrees of freedom were relaxed so that the OH molecule can also change its orientation with respect to the surface plane. Fig. 3-6 shows the OH adsorption energy on various Pt(111) surface sites with their equilibrium bond lengths and bond angles. The most stable configuration of OH is on the *bridge* site with the OH bond rotated towards the surface by about 70 degrees from the surface normal direction. Its energy is only slightly below that on the *atop* site, in agreement with previous theoretical work [131]. When increasing the OH coverage to 1/3 (in a $p(\sqrt{3} \times \sqrt{3})$ cell) OH is actually more stable on the *atop* site than on the bridge site. Hence, we used the *atop* site to study OH adsorption on Pt(111). In the *fcc* and *hcp* hollow sites, the Pt-OH bond is perpendicular to the surface though these sites have considerably weaker adsorption. Compared to the clean Pt(111) surface, OH coadsorption reduces the energy for CO adsorption by 0.12 eV although the C-Pt bond distance remains practically the same as in the case of oxygen co-adsorption.

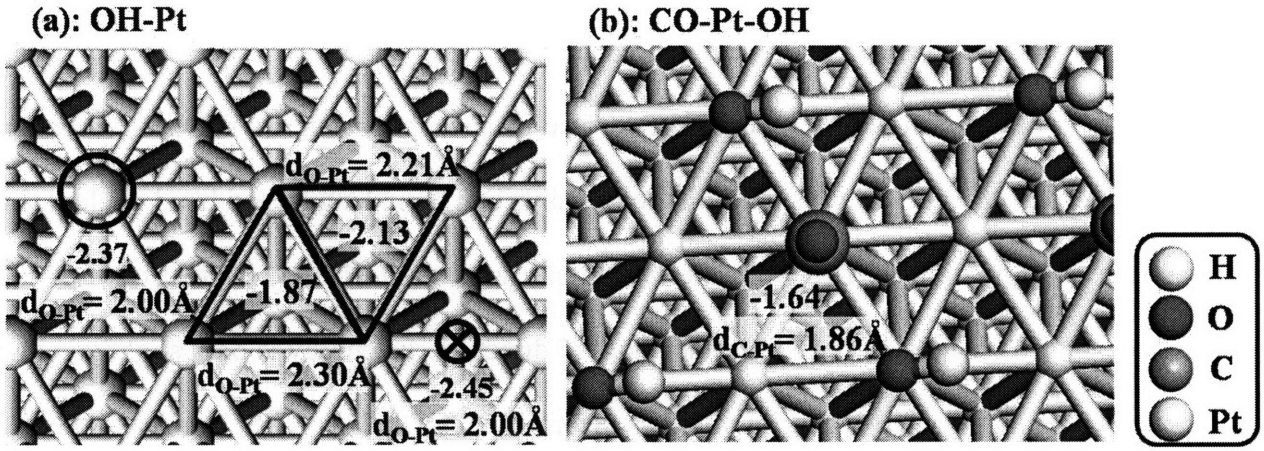

Figure 3-6: Adsorption energy on the Pt(111) surface for OH (a) and (b) CO in the presence of OH (all in a *p(2×2)* supercell*)*. Bond lengths of (O-H) are almost constant (~1 Å) regardless of adsorption sites and bond angles of Pt-O-H to the surface are zero degree in *fcc* , *hcp* sites but they tilt about 70 degrees at atop and bridge sites [132] (see Fig. 3-7 for details) .

Fig. 3-7 shows the surface structure of Pt(111) with OH in (a), and with coadsorption of CO and OH in (b). The surface Pt atoms are displaced up by OH (0.15 Å) and by CO (0.22 Å) as compared to a clean Pt(111) surface.

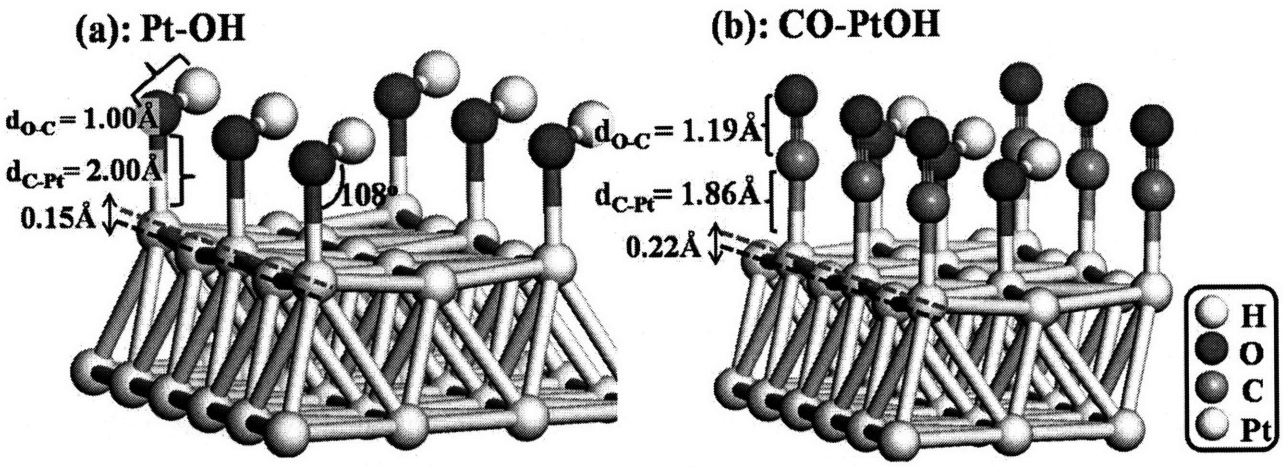

Figure 3-7: The surface structures of Pt(111)-*p(2×2)* with only OH in (a) and coadsorption of CO and OH in (b).

3.4.3 Alloying of Ru in Pt

Two mechanisms are generally called upon to explain the increased CO-oxidation rate when Ru is alloyed into Pt electrode particles: In the *bi-functional* mechanism adsorbates play a direct role by providing oxygen on the surface for CO oxidation [48, 96]. The *electronic* effect on the other hand focuses on the direct effect alloying may have on the weakening of the Pt-CO bond strength [47, 133]. We have tried to separate these effects by performing calculations on Pt-Ru(111) surfaces with and without adsorbates. Calculations are performed in a *p(2×2)* supercell with one Ru at the surface and all layers below the surface pure Pt. The adsorption energies for CO on the surface Ru atom, and Pt next to it, are given in Table 3-2 with their relevant bond lengths and angles. Fig. 3-8 shows the surface structures of CO-PtRu and CO-RuPt. In both cases, CO binds on *atop* site.

Table 3-2: Adsorption energies, bond lengths for CO on the Pt-Ru alloy surface. ΔE_{ad}^{chem} is the difference with the CO adsorption energy on the pure Pt(111) surface.

Surface	E_{ad}^{chem} [eV]	ΔE_{ad}^{chem} [eV]	*d*(C-Pt) (Å)	*d*(C-Pt) (Å)	*d*(C-Pt) (°)
CO-PtRu(111)	1.75	-6	1.84	1.2	0°
CO-RuPt(111)	2.31	-561	1.85	1.2	0°

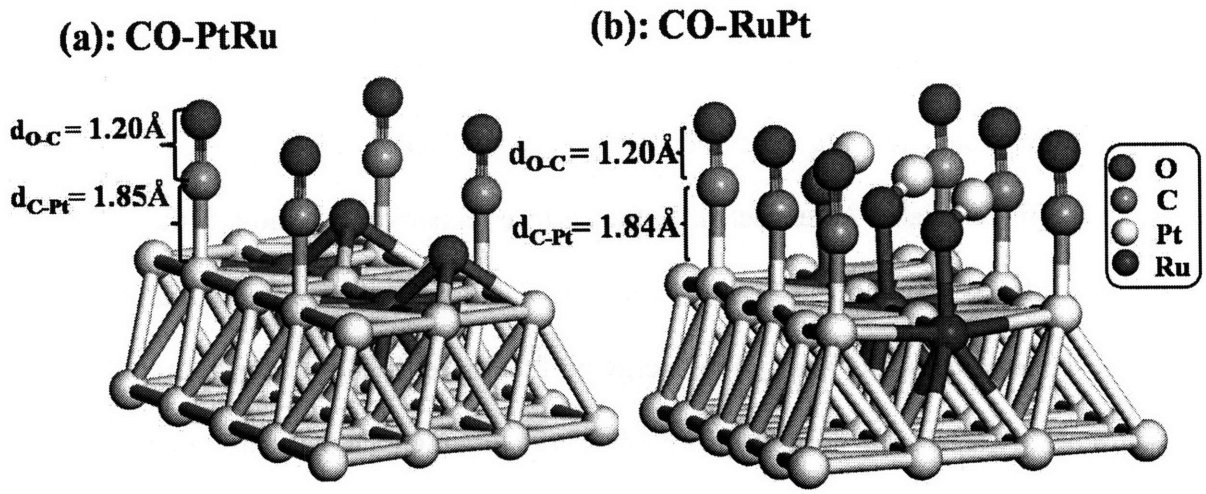

Figure 3-8: Surface structure of CO-PtRu(111)-*p(2×2)* in (a) and CO-RuPt(111)-*p(2×2)* in (b). While adsorption of CO on the *atop* site of Pt induces surface corrugation, binding with Ru keeps the surface flat.

Alloying Ru in the surface does not weaken the bond strength of (CO-Pt). In fact, it slightly enhances the adsorption of CO on Pt (*-6* meV higher than for pure Pt). Ge et al. [99] studied the adsorption of CO on the PtRu(111) alloy and claimed that the surface strain induced by the size mismatch of Pt and Ru (Ru is smaller than Pt by about 5%) increases CO adsorption. To quantitatively estimate the surface strain effect on the CO adsorption on PtRu(111) we recalculated the adsorption energy of CO in a supercell, *p(2×2)*, having all atoms except for CO fixed at the positions that atoms would have for a pure Pt surface. In this way, we can remove any strain effect from the variation in adsorption energy. Table 3-3 shows the CO adsorption energy on the frozen slabs. As expected, as the surface relaxation is removed, the Pt-CO bond strength is reduced by about 120 meV on pure Pt(111). But more importantly, without relaxation, Ru *lowers* the CO adsorption energy on Pt. Hence, it is the relaxation in the surface that makes bare Ru enhances the CO adsorption energy on Pt. Given that the strain plays such an important role in the effect Ru has on the Pt-CO bond strength, our results may be somewhat affected by the choice and size of the supercell and Ru coverage. Hence, the increase of the Pt-CO adsorption energy by 6 meV should be taken to indicate the general effect is small.

The bare Ru result may not be that important because under typical fuel cell conditions oxygen containing species, such as O or OH, are present on Ru islands. We show in the next section that such oxidized Ru is much more potent in reducing the Pt-CO bond strength than bare Ru might be.

Table 3-3: Adsorption energy of CO on the PtRu(111) surface without surface relaxation. ΔE_{ad}^{chem} is the difference in the adsorption energy of CO on PtRu(111) and on pure Pt(111) (both unrelaxed).

supercell	E_{ad}^{chem} [eV]	ΔE_{ad}^{chem} [meV]
$p(2 \times 2)$	1.63	+123

3.4.4 Simultaneous coadsorption and alloying

While many studies have investigated the effect of Ru on adsorption on Pt in vacuum conditions, it is more likely that in realistic electrode conditions, Ru sites are covered with oxygen or with hydroxyl groups. Indeed, our previous analysis, in which PtRu(111) surfaces were equilibrated in environments with varying oxygen chemical potential, shows that under most conditions Ru islands on the surface are covered with oxygen [100]. Hence, we study the effect of Ru on the CO-Pt bond strength under the condition that either O or OH is adsorbed near the Ru site. Calculations are performed in a *p(2×2)* supercell. The *atop* site is used for OH adsorption whereas the oxygen atom adsorbs on the *fcc* site.

Fig. 3-9 illustrates the calculated surface structures and Table 3-4 shows the variation of the CO-Pt bond strength/angles with varying alloying and adsorption conditions. All ΔE_{ad}^{chem} are calculated with respect to the reference of CO on a pure Pt(111) surface. While alloying Ru only has a weak (enhancement) effect in the Pt-CO bond strength (see Table 3-4), its effect becomes more profound as Ru is oxidized by O or OH. In all cases the Pt-CO bond strength is reduced

without any significant modification to the bond length and angle, corroborating the idea that different orbitals are responsible for the bond length and bonding energy [126].

Our results would indicate that the largest component of the electronic effect of Ru as an alloying element is indirect. It is only when Ru becomes oxidized that a significant bond strength reduction of the neighboring Pt-CO occurs. Hence the bi-functional mechanism (having Ru-O(H) close to the Pt-CO), and the electronic mechanism (having Ru-O(H) reduce the Pt-CO bond strength) both benefit the CO oxidation and may not be separable in experiments where only the overall CO throughput is measured. An elegant combination of cyclic voltammetry (CV) and temperature programmed desorption (TPD) did separate the two effects concluding that the bi-functional mechanism is about four times more effective in reducing the activation barrier for CO oxidation than is the ligand field effect [127]. Since our results point at the interfaces of Ru-Pt on the surface as the important places for CO oxidation, the island structure predicted by our recent Monte Carlo simulations under mild oxidizing conditions may be particularly interesting for making electrodes with high activity 100]. Surface Ru with O(H) bonded to it is beneficial for CO oxidation for two reasons: It reduces the Pt-CO adsorption, and provides an oxidation source for CO. The reduction of the CO-Pt adsorption energy that we find is somewhat larger, but in reasonable agreement with the value suggested by Lu et al. (~2 (kcal/mol)) [127].

Table 3-4: Adsorption energy of CO on Pt (or Ru) when coadsorption on nearby Ru (or Pt) is present. All ΔE_{ad}^{chem} are referenced to the adsorption energy of CO for pure Pt(111) surface.

Coadsorption & alloying	E_{ad}^{chem} [eV]	ΔE_{ad}^{chem} [meV]	d(C-Pt) (Å)	d(C-O) (Å)	d(Ru-O) (Å)	d(O-H) (Å)	Bond angle [°]
CO-PtRu-O	1.63	+123.4	1.85	1.20	1.94	N/A	N/A
CO-PtRu-OH	1.62	+132.1	1.85	1.20	1.94	1.00	61.9°

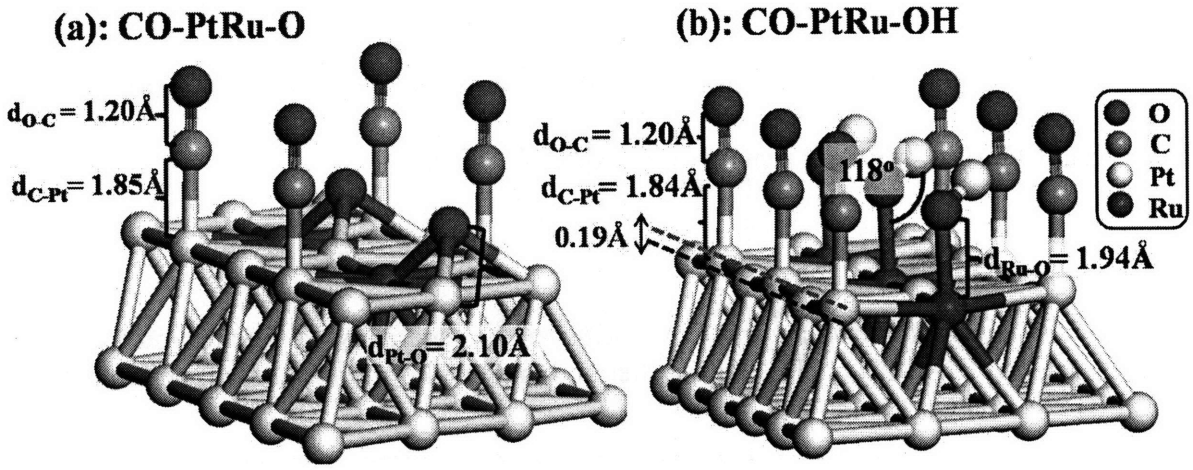

Figure 3-9: Surface of CO-Pt-Ru(111)-*p(2×2)*-O in (a) and CO-Pt-Ru(111)- *p(2×2)*-OH in (b).

3.4.5 Competitive adsorptions on Ru and Pt

So far, we have assumed that CO is bonded to surface Pt, and Ru on the surface is covered by either O or OH. This is a reasonable assumption as in methanol oxidation CO is generated on the Pt sites as intermediate. This does not, however, represent the thermodynamically favored state. Table 3-5 shows the energy for exchanging CO or OH between Pt and Ru sites. The surface consists of all Pt except a single Ru near to Pt, and all atoms in the sub-surfaces are Pt. Both of the adsorbates favor Ru and hence they will compete in bonding. If both CO and OH are present the thermodynamically favored state has CO on Pt and OH on Ru. If there are no adsorbates on the PtRu(111) surface except for CO, it has a strong driving force to move from Pt to Ru. If the suggestion in the literature that the activation barrier for CO diffusion on PtRu(111) surface is low [134-136] is correct, the displacement of CO from Pt toward Ru is kinetically feasible. Hence, the displacement of CO from Pt towards Ru is not only thermodynamically driven but also kinetically feasible. Under coadsorption of CO and OH, Ru relatively binds OH more strongly than CO. Hence, Pt will remain more exposed to CO.

Table 3-5: The energy for exchanging CO or OH, either separately or together between the Pt and Ru sites. A CO–PtRu(111)–OH is thermodynamically more favored structure to the CO–RuPt(111)–OH by 200 meV.

Surface	ΔE [meV]
CO-PtRu(111)	0
CO-RuPt(111)	-561
OH-RuPt(111)	0
OH-RuPt(111)	-702
OH-PtRu(111)-OH	0
CO-RuPt(111)-OH	202

3.5 Discussion

Figure 3-10 summarizes the variation of CO chemisorption energy on a Pt(111) surface as a function of coadsorption and Ru-alloying. The coadsorption of O or OH reduces the bond strength of Pt-CO under all circumstances. While some of this effect is electronic, our controlled calculation on frozen surfaces indicates that a substantial part of this coadsorption interaction may be attributed to surface relaxation effects. A crucial factor seems to be whether CO can "isolate" the Pt to which the CO binds by pulling Pt out of the surface. The difference between the calculation with and without surface relaxation (Table 3-2) confirms that CO strengthens its bond to Pt when the latter comes up from the surface. This can be understood by the bonding competition a Pt atom experiences between the CO adsorbed on Pt and its neighbors in the surface. Pulling the Pt out of the surface reduces the competition from the neighboring Pt atoms and makes a stronger Pt-CO bond. All of the adsorbates (CO, O and OH) pull surface Pt atoms up, but because oxygen bonds to three neighboring Pt atoms at the *fcc* site, it makes the surface flatter than OH, which adsorbs at the top site of a single Pt. This difference in surface strain explains why O is slightly better in reducing the adsorption energy of CO on Pt than OH. Hence, our results indicate that surface relaxations caused by coadsorption are very important in understanding the CO adsorption energy. While these relaxation effects are important on flat surfaces as studied here, they are even more likely to be significant in nano particle catalysts where the relaxation of surface atoms is less constrained.

Campbell et al. [92] reported that the rate of CO_2 production increases and its activation energy decreases as the oxygen coverage increases on the Pt(111) surface. They argue that the reduction of the adsorption energy is due to the repulsive interaction between the adsorbates,

reducing the electron back donation from Pt to $2\pi^*$ orbital of CO by oxygen. Gland et al. [102] also observed that the activation energy of CO_2 formation changes as a function of the surface concentration of oxygen and CO, from 40 kcal/mol on an almost clean Pt(111) surface to 17 kcal/mol at the saturation coverage. They attributed this decrease to the repulsive interactions between CO and O. They also observed that both CO and O form island structures on the Pt(111) surface, with an oxidation reaction occurring as CO diffuses into the boundaries of the island structure of oxygen atoms. These results are consistent with our findings. The reduction of the CO-Pt adsorption energy by oxygen atom is equivalent to a repulsive interaction between the two adsorbed species.

When surface relaxation is prohibited the presence of Ru near Pt decreases the CO adsorption energy, but surface relaxation washes this effect out and actually turns it slightly in the other direction. The effect of pure Ru is in each case rather small and likely not relevant under practical catalyst operating conditions. However, once Ru is oxidized by O or OH adsorption (a likely scenario) the CO adsorption energy on a neighboring Pt is reduced by $0.12 \sim 0.13$ eV.

All species preferentially adsorb on Ru when both Ru and Pt are present in the surface, though the simultaneous adsorption is more complicated. When both CO and a stronger oxidizing species such as O or OH are present on the surface, CO prefers Pt, and OH and O prefer Ru. Assuming CO is adsorbed on Pt (a reasonable assumption in the catalysis of hydrocarbons) its possible migration to a Ru site depends on the external (electro) chemical potentials of O and OH. If these are high enough to cause adsorption on Ru, CO will remain on Pt and the surface will consist of CO-Pt and Ru with O or OH coverage. In this case, CO removal from Pt can only proceed by oxidation to CO_2 (likely to occur at the boundary between

Pt and Ru islands). For low O or OH chemical potentials, CO is at least thermodynamically favored to migrate from Pt to Ru. It seems from these approximate arguments that an *ideal* situation would be one where Ru is somewhat covered with O or OH to provide oxidants but not fully covered so that CO can still migrate there from Pt.

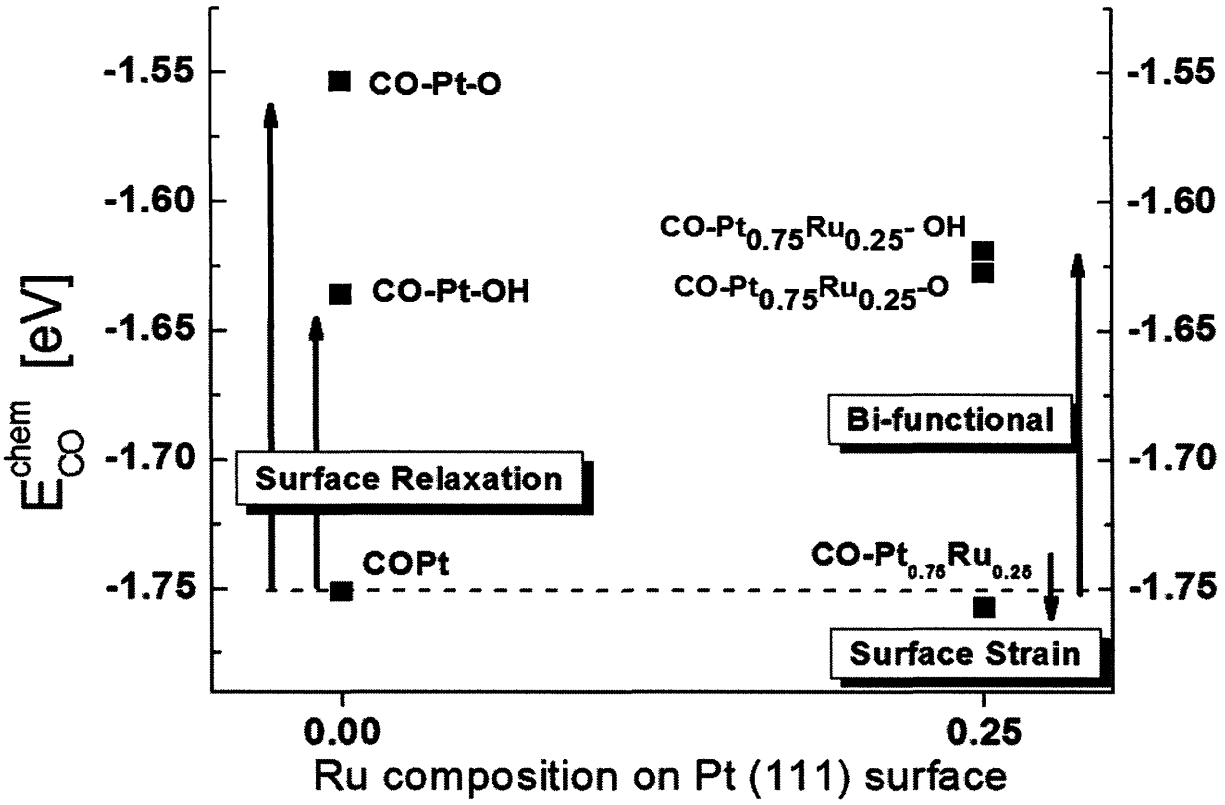

Figure 3-10: The variation of adsorption energies of CO on the Pt(111) surface as a function of coadsorption and alloying of Ru into Pt surface. While coadsorption of O or OH always decreases the bond strength of CO-Pt, alloying Ru into Pt(111) surface enhances it. However, once Ru is oxidized by O(H) the adsorption energy of CO reduces dramatically.

3.6 Conclusion

We studied the adsorption energy of CO on Pt(111) surface as a function of varying chemical conditions, such as the coadsorption of O(H) and alloying with Ru. Our results show that coadsorption of either O or OH always decreases the CO adsorption energy for both pure Pt and a Pt-Ru surface alloy. The surface relaxation effect is a key factor that transfers the interaction between adsorbed CO and O or OH. Alloying Ru to a Pt(111) surface in fact enhances CO adsorption slightly, but once Ru next to Pt is oxidized by O(H) the bond strength of Pt-CO decreases dramatically. Considering that the adsorbates can induce surface segregation of Ru and form island structures [100], the boundaries of these structures can be very important place for the chemical reaction of CO oxidation.

Chapter 4

Effect of particle size and surface structure on adsorption of O and OH on Platinum nano particles

4.1 Overview

This chapter is for studying the effect of particle size and surface structure on the chemisorption energy of OH and O on nano particles of Pt by using first principles density functional theory (DFT). We find that the chemisorption energies of O and OH are strongly affected by the size and structure of the Pt particle varying by up to 1.0 eV at different adsorption sites and particle sizes.

4.2 Introduction

To surface scientists, it is of interest to understand the detailed mechanism of electrocatalysis on the atomic scale since it leads to better control of the chemical reactions and may result in the rational design of better catalysts [137].

Modern electrocatalysts in fuel cells are Pt-alloy metallic nanoparticles dispersed on supports [138] such as carbon, aluminum oxide or titanium oxide. Both experimental measurements [139-

141] and computational calculations [142, 143] seem to indicate that nano-sized electro-catalysts show considerably different catalytic activity from extended flat surfaces. These investigations would indicate that changes observed with particle size reduction go well beyond the increase in surface area, but involve fundamental physical and chemical changes in the catalytic steps.

The unique activity of nano-sized electrocatalysts is still under debate [137, 144-146]. For example, on the basis of the XPS measurement, Mukerjee et al. [146] explained that the amount of *d*-band vacancies of metal catalysts, which control the surface reactivity with adsorbates [147], depends on the geometrical arrangements of the atoms around the adsorption sites as well as on the support materials and alloying [148]. Hammer and Nørskov [137, 149] attempted to explain the general trend of the chemical adsorption energies as a function of the metallic catalysts and its particle size through a *d*-band center model. According to the model, it is the relative shift of the *d*-band center (ε_d) of the catalyst atoms with respect to the Fermi energy (ε_F) that controls the surface reactivity. This model has been intensively used to describe experimentally measured chemical activity over a series of transition metals [150-152]. Several computational studies have reported that a simple parameter such as the *d*-band center [137], Density of States (DOS) around Fermi energy [153], a hole concentration of *d*-band around Fermi level [147] may not be enough to fully elucidate the effect of particle size and structure of adsorption site [154-156].

The general mechanism by which particle size influences catalytic activity is difficult to elucidate experimentally, as it is not easy to synthesize catalysts with well-defined size and structure. In addition, the activity of catalysts is measured by turnover frequencies (TOF), which

are quantities averaged over different particle sizes and active sites. While, ab-initio computational modeling offers in principle full control over the size and shape of the catalyst, it has typically been limited to bulk materials or systems of small size [157-160]: The morphology of the surface (i.e., the distribution of the various types of surface sites) changes with size and cannot be fully decoupled from the size effect. This is particularly true for particles with very small size for which the equilibrium shape often changes drastically with size [161, 162] Considering that the average size of catalyst particles in commercial fuel cells is around a few nano meters, it may be important to understand this simultaneous effect of size and surface structure.

In this paper, we therefore, chose to study explicitly Pt nano particles of 1nm and 2nm size and compare their chemical adsorption properties to those of an extended flat Pt(111) surface. We focus on the chemisorption energies of atomic oxygen (O) and the hydroxyl group (OH) and investigate how their chemisorption energies are modified by particle size and by the reduction in coordination for Pt at the surface. A chemical adsorption is an important step in the catalytic process which can be related to catalytic activity [163] and O and OH are two species of considerable importance in the electrocatalysis step of low temperature fuel cell [164, 165].

4.3 Methodology

To investigate the effect of Pt particle size and surface morphology on chemisorption, we set up three model systems shown in the Fig. 4-1: an extended flat Pt(111) surface, and Pt nano clusters of 1 and 2nm in size. The Pt (111) surface model consists of a six layer slab as described

in our previous work [166]. The 2nm Pt cluster is a 201-atom truncated octahedron of which 122 atoms (60%) are on the surfaces. The surface consists of (100) and (111) facets. For the 1nm Pt cluster structure we take the experimentally observed 167, 168] cubo-octahedron composed of 55 Pt atoms of which 42 atoms (76%) are on the surface.

The relevant adsorption sites on the surface of these model systems are represented in Table 4-1. The coordination number (Z) of an adsorption site is defined as the average nearest neighbor coordination of the Pt atom(s) that defines the adsorption site (e.g. one Pt for atop adsorption, three for fcc and hcp site adsorption).

Computation of all chemisorption energies was performed in the spin polarized Generalized Gradient Approximation (GGA) to DFT with Perdew-Wang exchange correlation functional (GGA-PW91) [110, 111]. The Projector Augmented Wave (PAW) method [73, 109] was used as implemented in VASP [112, 113]. In the Pt(111) slab, all adsorbates and the topmost four layers of Pt atoms are relaxed while the bottommost two layers fixed to the positions of the relaxed pure Pt slab. In the Pt nano particles, all atoms, including adsorbates, are fully relaxed, and periodic boundary conditions are implemented with a large enough vacuum to preclude interactions between the cluster and its images. The reciprocal space integration was performed with eight irreducible k-points for the 1nm Pt cluster, and convergence was tested with up to 27 k-points. For the 2nm Pt cluster, only the gamma point was used. All degrees of freedom are relaxed so that the OH molecule can change its orientation with respect to the surface plane.

The chemical adsorption energy (E_{ad}^{ads-Pt}) is calculated from the total energy difference between the system with the adsorbate (E_{Pt}^{ads}), the pure Pt system ($E_{Pt}(s)$) and the adsorbate in the gas phase ($E_{ads}(g)$):

$$E_{ad}^{ads\text{-}Pt} = \left[E_{Pt}^{ads} - \left(E_{Pt}(s) + E_{ads}(g) \right) \right] \tag{4-1}$$

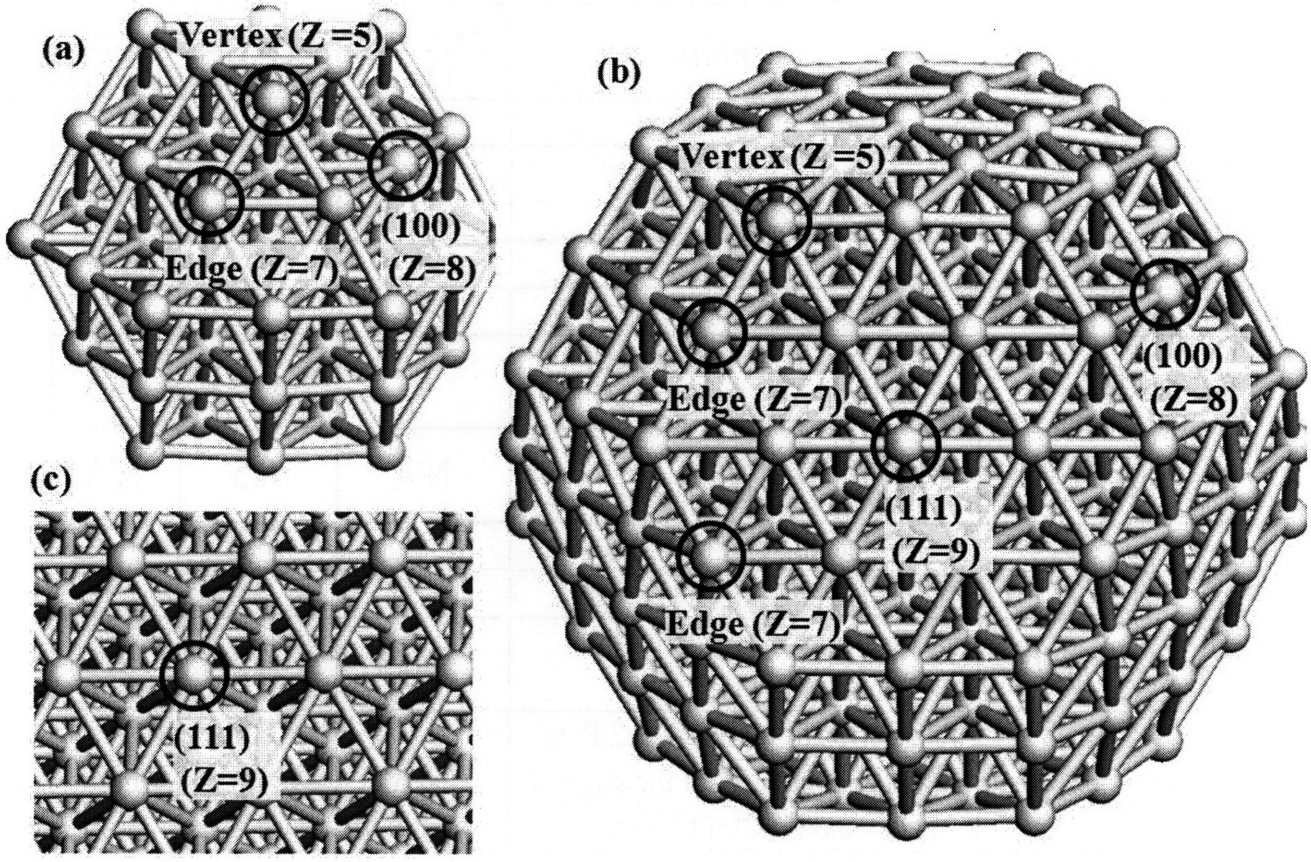

Figure 4-1: Different model systems used in our study: an 1nm Pt cluster (a), a 2nm Pt cluster (b) and an extended flat Pt(111) surface (c). Surface sites of different symmetry are depicted in the model systems. The coordination number "Z" of the adsorption site is as defined in the text.

Table 4-1: Relevant adsorption sites on the surface of the three model systems with their location and coordination number. An "N/A" means the adsorption site is not available in the model system.

adsorption site	location	coordination number of Pt (Z)		
		1 nm	2 nm	Pt(111)
AV	atop site at vertex	5	6	N/A
AE(1,0)	atop site at the edge of (111) and (100) facets	7	7	N/A
A(100)	atop site at (100) facet	8	8	N/A
A(111)	atop site at (111) facet	N/A	9	9
BE(1,0)	bridge site at the edge of (111) and (100) facets	6	6.5	N/A
BE(1,1)	bridge site at the edge between (111) facets	N/A	6.5	N/A
B(100)	bridge site on (100) facet	7.5	7.5	N/A
B(111)	bridge site on (111) facet	7	9	9
F-1 (H-1)	fcc (hcp) site around the center of (111) facet	7(6.3)	9(9)	9(9)
F-2 (H-2)	fcc (hcp) site set up with 2 Pt at (111) facet and 1 Pt at the edge of (111) and (100) ((111)) facet	N/A	8.3(8.3)	N/A
F-3 (H-3)	fcc (hcp) site set up with 2 Pt at the edge of (111) and (100) facets, and 1 Pt at (111) facet	N/A	7.3 (7.3)	N/A

4.4 Results

4.4.1 Chemisorption energy of O

Figure 4-2 shows the chemical adsorption energies of O at different adsorption sites on the three model systems. For the extended flat Pt(111) surface, oxygen atoms prefer to adsorb on the high symmetry sites, such as the fcc (which is the most stable site on the bulk Pt (111) surface) and hcp site. Chemisorption on an atop site is much weaker. On the bridge site oxygen is not stable and slides off to the fcc site. These bulk results agree well with previous calculations [123, 125, 150] and experimental observations [121, 122].

Oxygen atoms show significantly different chemical adsorption on the Pt nano clusters. In general, the surface of the 1nm Pt cluster attracts O much more strongly than the surface of the 2nm Pt particle or the bulk surface. (The fcc site is a notable exception and will be discussed in the next section). Under-coordinated Pt atoms, created by edges and vertices can be seen to have particularly high chemical reactivity. For example, on the 1nm cluster, the chemisorption energy of O at the atop position changes from −3.72 eV at the center of the (100) facet (A(100), Z = 8) to −4.55 eV at the vertex (AV, Z = 5). For the 2nm cluster, the atop adsorption energies vary from -3.01 eV at the (111) facet (A(111), Z = 9) to −3.30 eV at the vertex (AV, Z = 6). The effect of coordination number effect can be observed for all adsorption sites (fcc, hcp, atop etc.). In general, as the sites are further away from the center of the (111) facet, the O-Pt bond strength becomes stronger.

Although for the extended flat Pt(111) surface and the 2nm Pt cluster, fcc sites are more stable than hcp sites, their stability is reversed in the 1nm Pt cluster. This can be understood by considering the local environment of these sites. As Fig. 4-2 shows, one of the three Pt atoms

creating the hcp site in the 1nm cluster is located at a vertex, leaving it significantly under coordinated compared to atoms in fcc site, and enhancing its binding energy with O.

Figure 4-3 shows the adsorption energy of O as a function of bond length for the various sites and systems. Clearly, the bond length does not correlate with the variation of adsorption energies as was already pointed out for the adsorption of other molecules on Pt [169]. The bond distance of O-Pt is largely controlled by the nature of the adsorption site regardless of particle size.

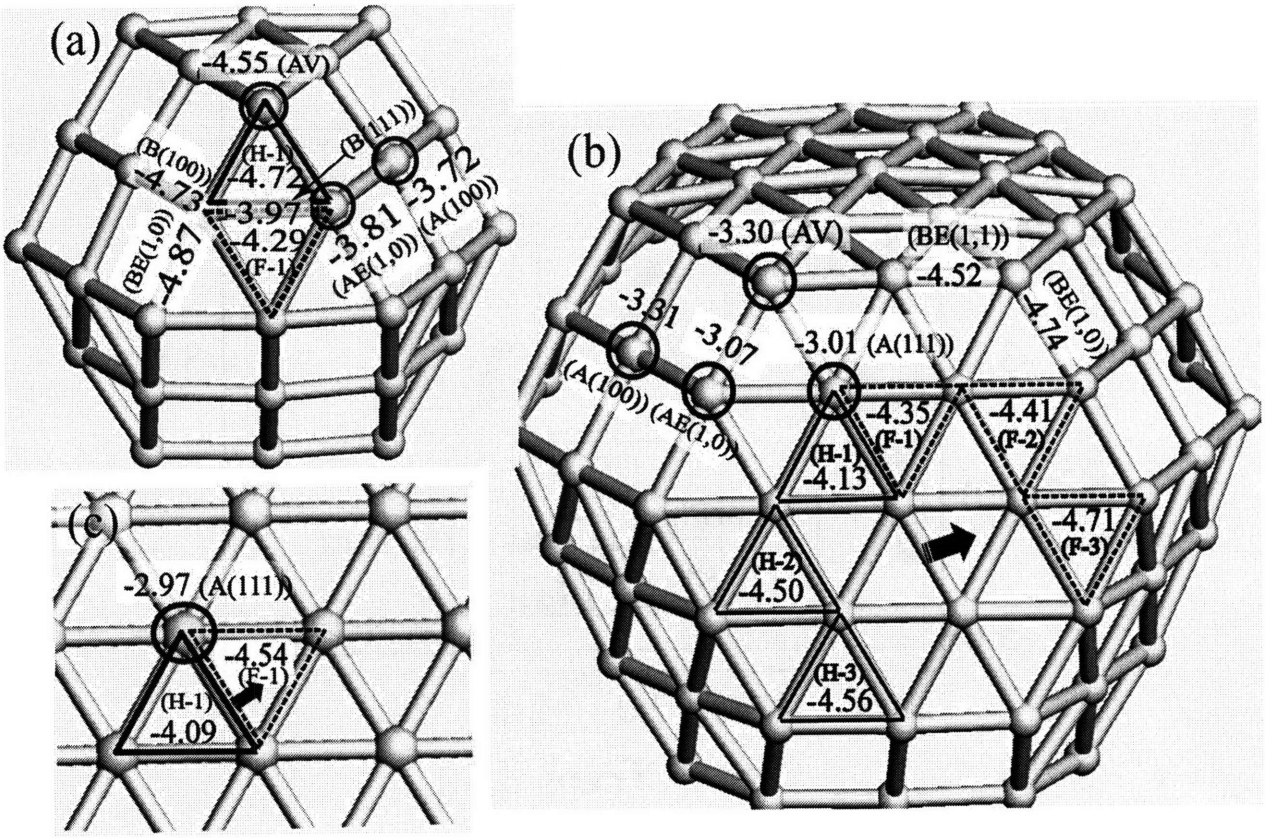

Figure 4-2: Chemisorption energies of O at various surface sites of the Pt model systems: 1nm (a) and 2nm clusters (b), and Pt(111) surface (c). Solid (dashed) triangles denote a *hcp* (*fcc*) site. An oxygen atom at *bridge* site on the (111) facet of the 2nm cluster and on the Pt(111) surface is unstable and moves to an *fcc* site (indicated by solid arrows).

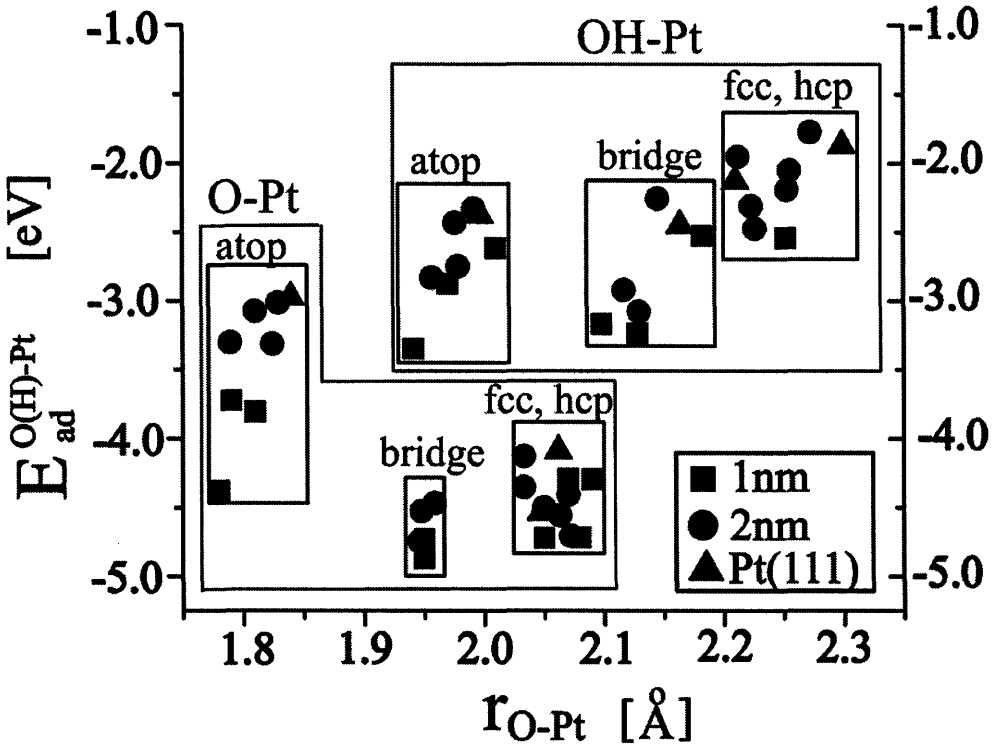

Figure 4-3: Chemisorption energies of O and OH as a function of bond length with Pt.

4.4.2 Chemisorption energy of OH

In contrast to oxygen, OH preferentially adsorbs at the atop or bridge position of the extended Pt(111) surface, with the Pt-O-H bond angle about 70o from the surface normal. At fcc or hcp sites such tilting of the Pt-OH bond angle would bring the H too close to Pt surface atoms, and the equilibrium configuration is a linear Pt-O-H bond [166],[170]. The bonding angles do not change considerably on the 1 and 2nm Pt clusters. Similar to O, OH binds to the 1nm Pt particles more strongly than to the 2nm particles for all sites. However the most stable sites vary with particle size: For the 1nm the atop at a vertex (AV) is most stable, while on a 2nm particle, the bridge between (111) and (100) facets (BE(1,0)) has the strongest adsorption energy.

The chemisorption energy of OH is also influenced by the coordination number of the adsorption site. For instance, for the 1nm particle the bond strength at an atop site varies from -2.61 eV at the center of the (100) facet (A(100), Z = 8) to -3.35 eV at a vertex of the particle (AV, Z = 5). In the 2nm cluster, the atop adsorption energies change from -2.33 eV at the (111) facet (A(111), Z = 9) to -2.83 eV at a vertex (AV, Z = 6). These differences in adsorption energy of OH are smaller than for O (Table 2). This may be due to the fact that the OH group binds in general less strongly as O and H already form a stable bond.

Figure 4-3 also shows the Pt-O bond length for Pt-OH. While there is a general increase in energy for Pt-OH (decrease in adsorption energy) as the bond length increases, the bond length is again largely controlled by the type of adsorption site.

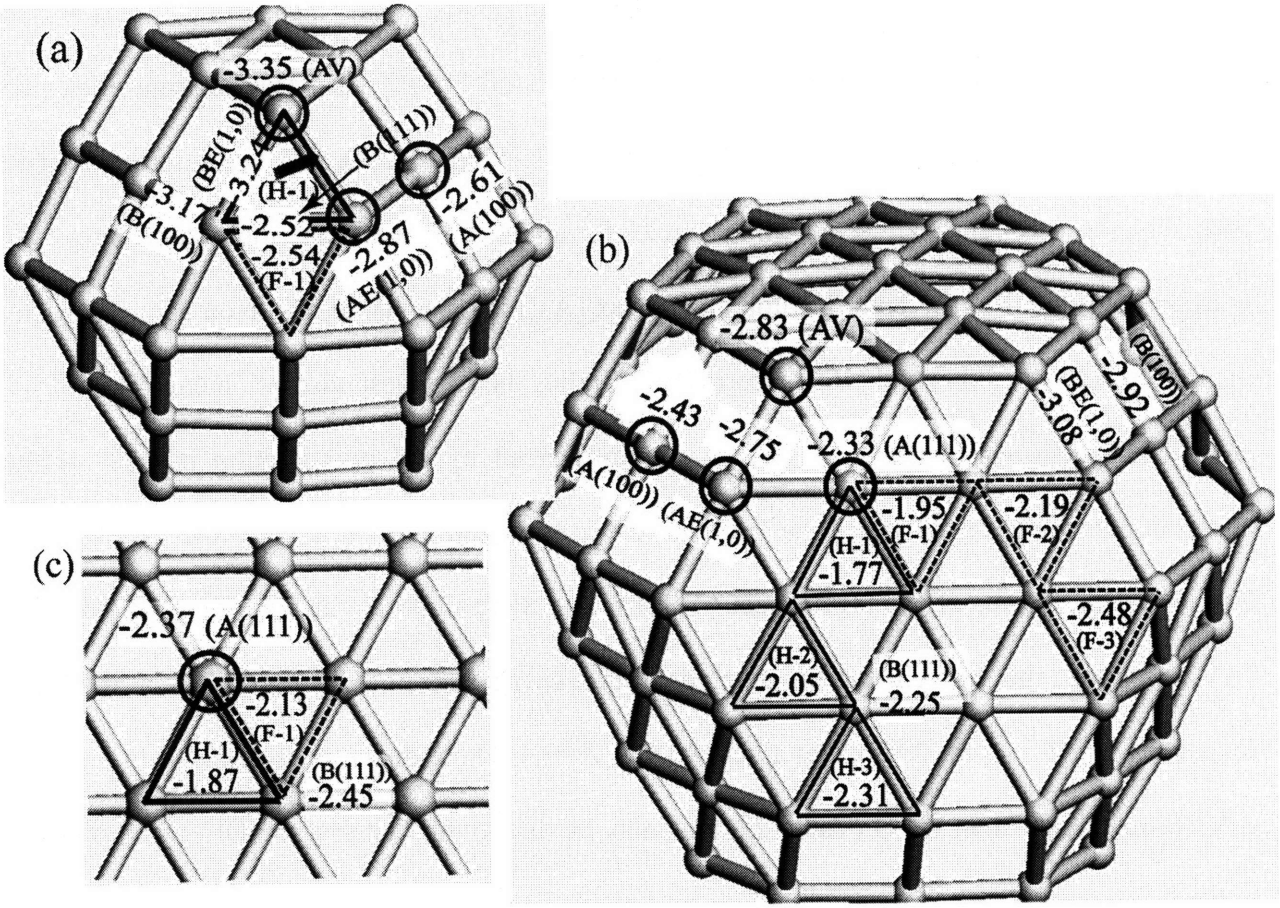

Figure 4-4: Chemisorption energies of OH at various sites of the Pt model systems: 1 nm (a) and 2 nm clusters (b), and Pt(111) surface (c). Solid (dashed) triangles denote *hcp* (*fcc*) sites. The OH group at an *hcp* (111) site on the (111) facet of the 1nm cluster is unstable and moves to *edge* site (marked by a solid arrow).

Table 4-2: The strongest and weakest adsorption sites and their adsorption energies for O and OH in the three Pt model systems. The energy difference (ΔE) is given between the two sites.

Adsorbate \ Model system			1 nm	2 nm	Pt(111)
O	strongest adsorption	site	*BE(1,0)*	*BE(1,0)*	*F-1*
		energy	-4.87	-4.74	-4.54
	weakest adsorption	site	*A(100)*	*A(111)*	*A(111)*
		energy	-3.72	-3.01	-3.08
	ΔE [eV]		-1.15	-1.73	-1.46
OH	strongest adsorption	site	*AV*	*BE(1,0)*	*B(111)*
		energy	-3.35	-3.08	-2.45
	weakest adsorption	site	*F-1*	*H-1*	*H-1*
		energy	-2.52	-1.77	-1.87
	ΔE [eV]		-0.83	-1.31	-0.58

4.5 Analysis and Discussion

The results presented in the previous section indicate that the effect of particle size and local surface structure on the chemisorption energies of O and OH is substantial. These two factors are, in fact, strongly coupled since the equilibrium shape of a nano particle depends considerably on its size [171]. Hence, it may not easy to decouple the two effects with experimental measurements which would provide quantities that entangle the effect of both factors. First principles DFT method, however, enables us to approach the task in a more or less systematic ways probing the energy of adsorption at every site.

4.5.1. Effect of surface structure (coordination number) of adsorption site

An overall trend is that the adsorption energy increases as the Pt atom involved in the adsorption become less coordinated by other Pt. This can be very clearly observed in Fig. 4-5, which shows the chemisorption energies of O and OH on the 2nm Pt particle for three fcc and hcp sites with different amount of under-coordinated atoms. As the boundary atoms are considerably under-coordinated compared to those in the center of the facets, the adsorption energy increases as adsorption site moves towards the boundaries of facets. The magnitude of the variation ($\approx$ 0.4 eV for O and $\approx$ 0.5 eV for OH) must have dramatic consequences on the range of oxygen pressures or electrochemical potentials at which nano-sized Pt oxidizes. The effect of coordination is stronger than the bulk fcc/hcp adsorption energy difference since the hcp site containing a vertex Pt attracts O and OH more strongly than an fcc site in the center of the (111) facet.

Similarly Fig. 4-6 shows the effect of Pt coordination for adsorption on the atop and edge sites of the 1 nm and 2 nm particles. The chemical adsorption energies at the atop and edge sites vary by as much as 0.9 eV (O-Pt) and 0.7 eV (OH-Pt) for a 1 nm Pt particle, and about 0.3 eV (O-Pt) and 0.8 eV (OH-Pt) in the 2 nm particle. Therefore, the effect of coordination number on the chemisorption energy at the atop and edge sites is even more substantial than for the high symmetry fcc and hcp sites.

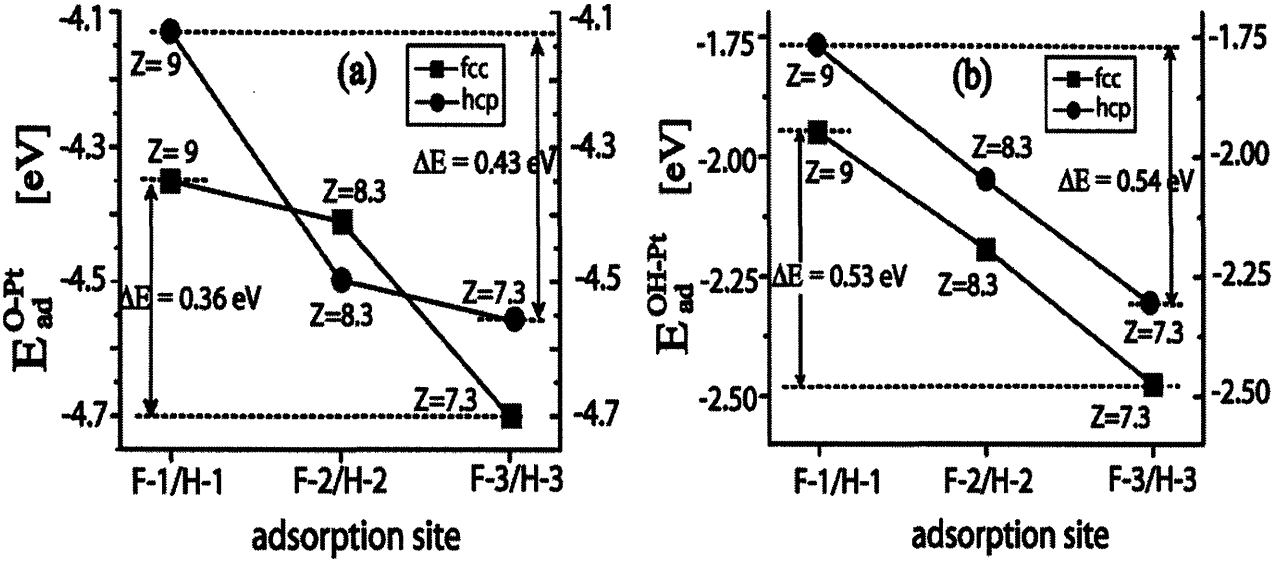

Figure 4-5: The chemisorption energies of O (a) and OH (b) at *fcc* and *hcp* sites on the (111) facet on the 2nm cluster. The position of adsorption site is numbered with decreasing coordination and can be located on Fig. 4-2 and Fig. 4-4.

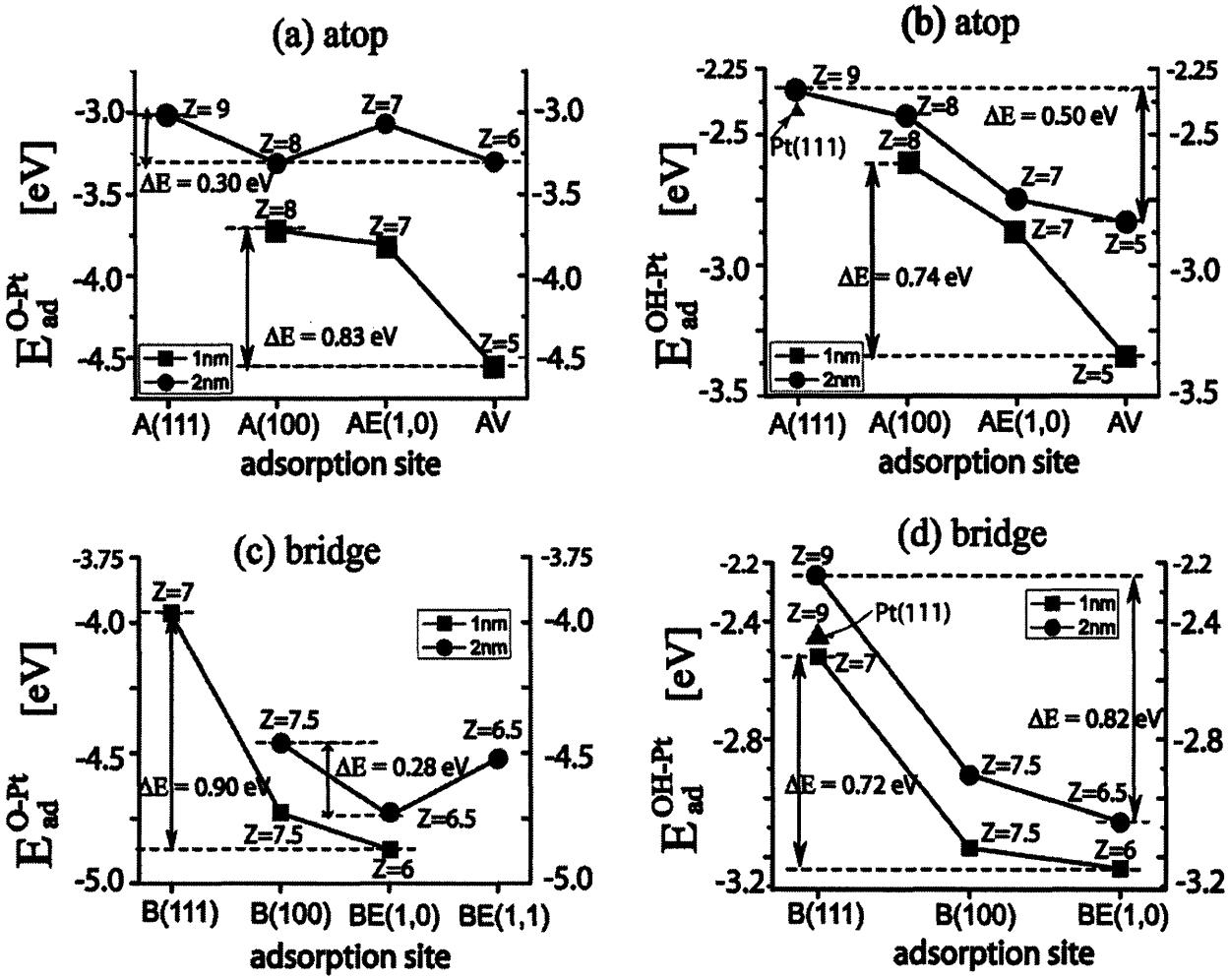

Figure 4-6: Effect of coordination number on the chemisorption energy of O and OH at *atop* (a and b) and *bridge* (c and d) sites of the two Pt nano-particle model systems. Note that oxygen atom is not stable at the *bridge* site of the (111) facet (B(111)) in the 2nm particle.

4.5.2 The effect of a particle size

In Fig. 4-5 and Fig.4-6 we showed the effect of Pt coordination on the adsorption energy for different site on a particle of fixed size. With Fig. 4-7 we try to investigate whether there is an intrinsic particle size effect on the adsorption energy even for sites with similar coordination but on a different particle size. Figure 4-7 shows chemisorption energies of O and OH on the three Pt model systems as a function of Pt particle size for a given adsorption site. We attempted to pick corresponding sites on each particle with the same coordination as much as possible. Since all the Pt atoms on the (111) facet of a 1nm cluster are on the edges or vertices, they are compared to the chemical adsorption energies of O and OH on similar edges or vertices of the 2nm cluster. Hence, the energy differences shown in Fig. 4-7 are largely induced by the effect of particle size. For reference, the chemisorption energies of O and OH on a Pt(111) bulk surface are also presented. As the results in Fig. 4-7 show, O and OH bind more strongly to the 1nm particle (except for the fcc site). The largest size effect for both O and OH occurs for binding at the atop vertex site (~ 1.2 eV). The adsorption energy for O(OH) on the bridge site varies by 0.06 eV (0.16 eV). Hence, particle size effects are the most pronounced at the atop vertex.

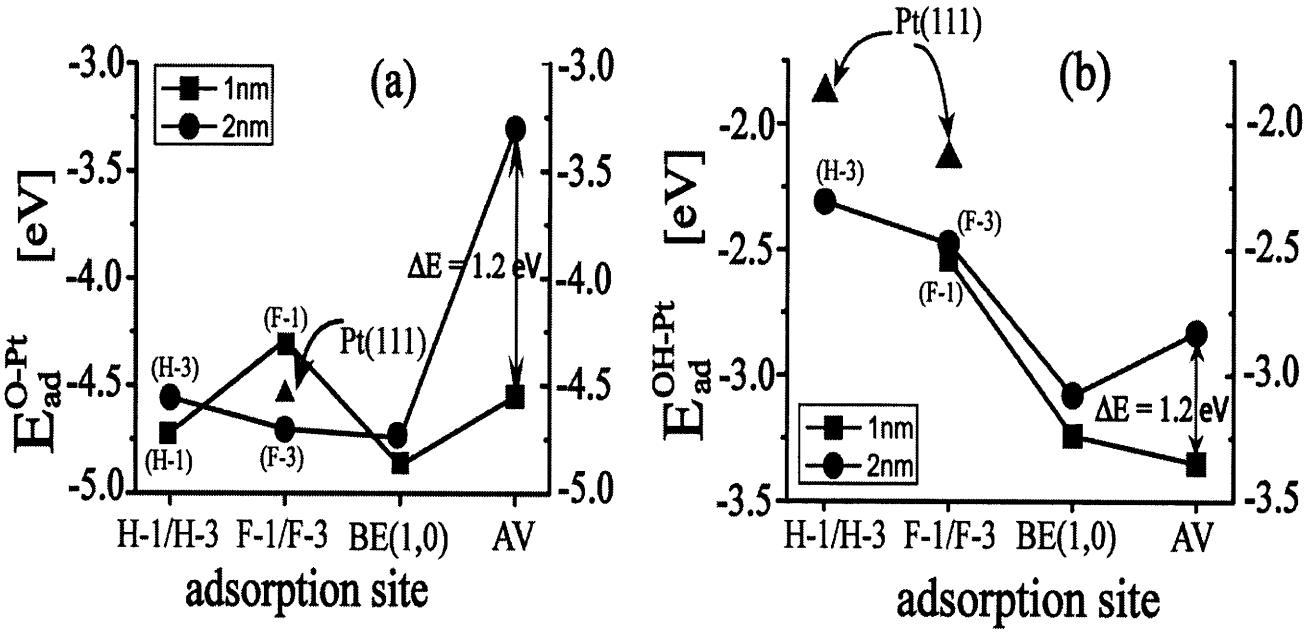

Figure 4-7: Comparison of chemisorption energies of O (a) and OH (b) on sites with similar coordination in the nano particles and the (111) bulk surface. OH at *hcp* site on the (111) facet (H-1) of the 1nm Pt cluster is unstable and moves to *bridge* site.

4.5.3 Electronic structure effects

The previous sections demonstrate that both coordination environment and particle size of Pt significantly affect its chemical ability to adsorb O and OH. One may ask whether this variation of chemisorption energy can be described by a simple underlying parameter or physical change. Hammer and Nørskov previously suggested a model that relates chemisorption to the location of the *d*-band center (ε_d) of the transition metals [124]. Figure 4-8 shows chemisorption energies of O and OH on the three Pt model systems as a function of the unadsorbed *d*-band center of the Pt located at the adsorption sites. The solid (dashed) lines denote linear fits of the chemical adsorption energies of O (OH) to the *d*-band center of Pt at the adsorption site. The chemisorption energy at the atop and bridge sites vary more than at the fcc and hcp sites for the same amount of the *d*-band center change. This clearly indicates that the *d*-band center is not the only variable that controls the adsorption energy. Actually, it may not at all be a relevant variable when change in particle size and coordination occur. While the *d*-band center shift correlates with the overall variation of the chemisorption energies a unique relation with the *d*-band center is not present (marked by circles in Fig.4-8).

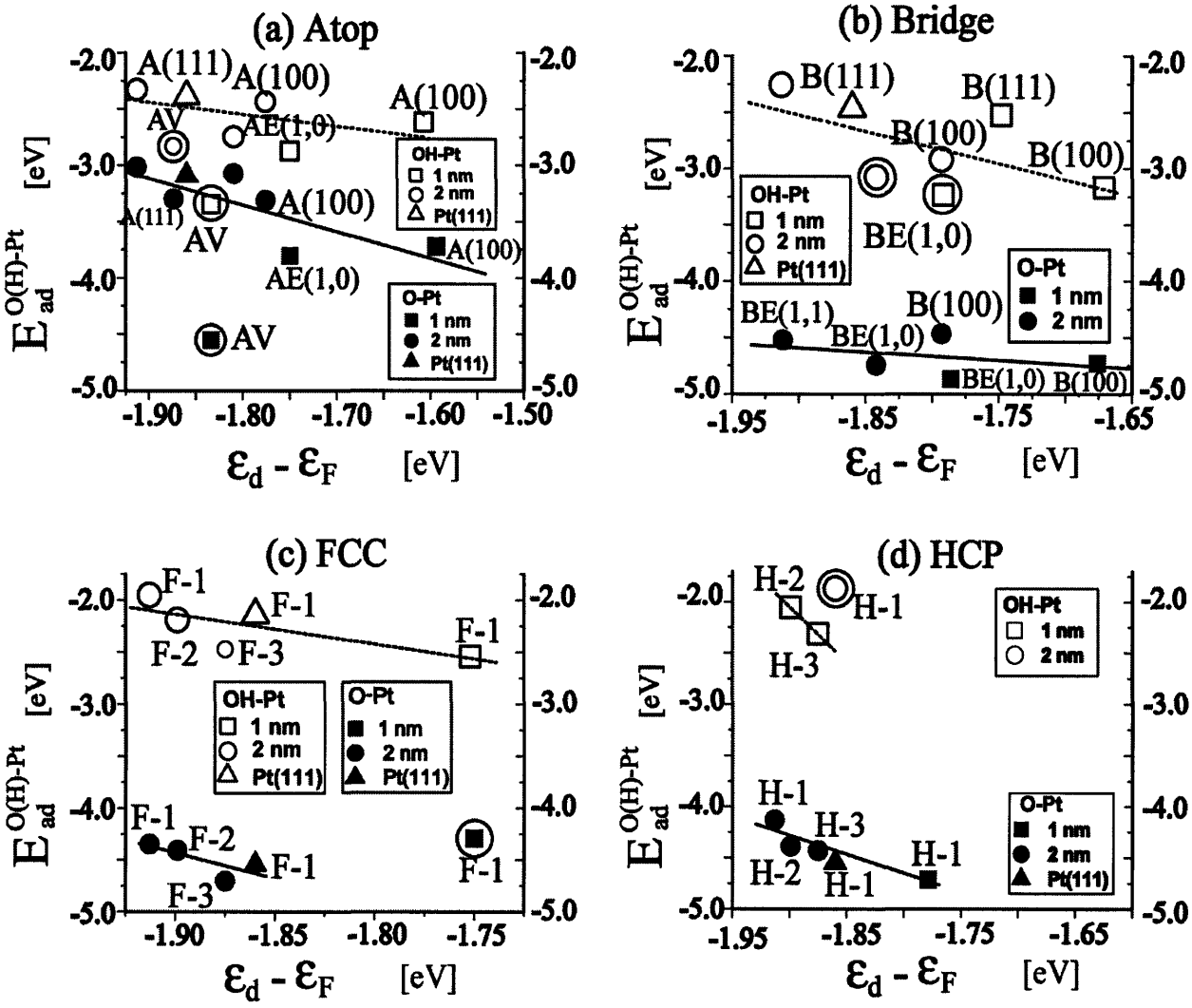

Figure 4-8: Chemisorption energies of the O and OH on the three model systems as a function of *d-band* center at the adsorption site. The solid (dashed) lines are a linear fit of adsorption energy of O (OH) to *d*-band centers for each site: atop (a), bridge (b), fcc (c) and hcp (d). The site, which shows a large deviation, is marked by a circle.

4.5.4 Discussion

The chemisorption energies of O and OH vary considerably between the Pt(111) surface and 1 and 2nm particles. Only some sites near the center of the (111) facet on the 2nm show similar adsorption energies to the Pt(111) bulk surface as shown in the Fig.4-9. While we find that on the bulk surface the fcc site is the most stable adsorption site, in agreement with previous work [172-174], oxygen adsorption is strongest in bridge sites on the edges of the 2 and 1nm particles. For both particles the maximal adsorption energy is stronger than on the bulk surface. The adsorption energies in the fcc and hcp sites of the nanoparticles are distributed above and below the bulk surface value, with adsorption getting stronger as the site is closer to the edge of the surface.

For OH adsorption, the effects of particle size are more dramatic. For OH in dilute concentration, as is the case in our supercell, the most stable sites on the bulk (111) surface are bridge and atop sites, in agreement with earlier work [166, 170]. At higher concentration of OH, experiments indicate that adsorption shifts to the atop position [175]. The adsorption energy for OH in both positions increases dramatically in the 2nm particle (Fig. 4-4) going up by more than half an electron volt. This trend continues in the 1nm particle where the atop site becomes the most stable site with almost an eV higher adsorption energy. The fcc and hcp positions, which are typically not favored for OH also increase in adsorption energy when the particle becomes smaller, though the effect is less pronounced than for the lower coordinated edge and vertex sites. These results enforce the notion that to estimate the surface reactivity of nano scale Pt catalyst a relevant Pt model system is important, and bulk values may be less relevant than previously thought.

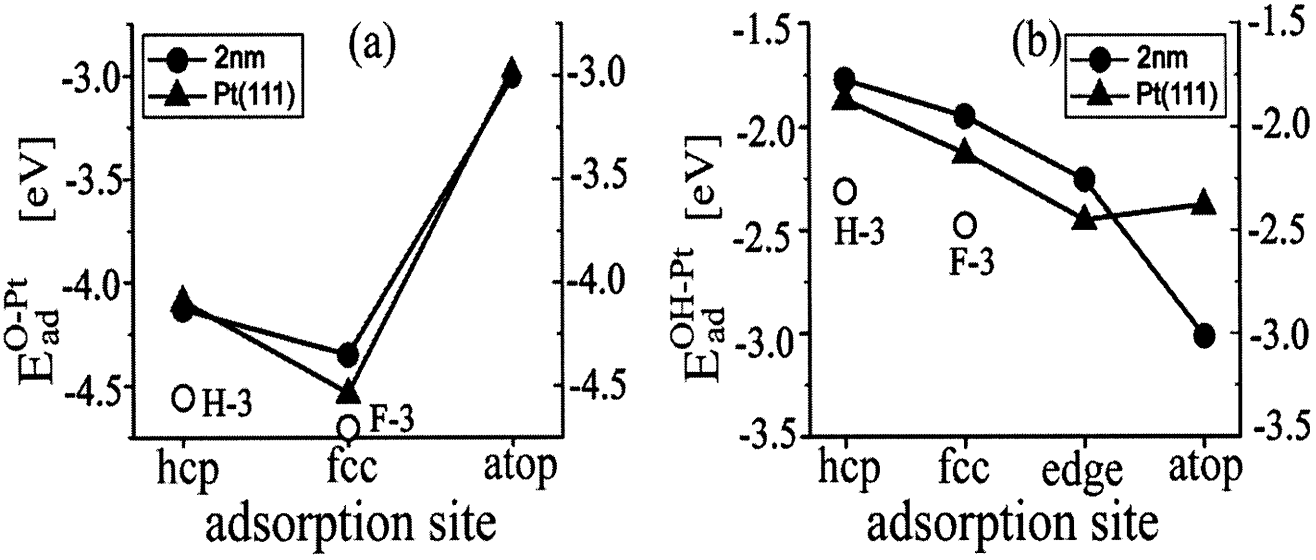

Figure 4-9: Chemisorption energy of O (a) and OH (b) on the (111) facets of the 2nm cluster and on the Pt(111) surface as a function of adsorption site.

While the *d*-band center has been successfully used to explain the variation of adsorption energy with chemistry under identical surface geometry [176] it does not capture most of the variation we find between different sites and particle size (Fig. 4-8). While there is an overall trend that the adsorption energy increases as the *d*-band center moves closer to the Fermi level, the adsorption energies seem to be largely controlled by long-range coordination effects. This can be best observed by comparing the adsorption energy of a given type of site at different positions on the nanoparticle, as for example presented in Fig. 4-5. As the site gets closer to the edge of the surface the adsorption energy increases. This position dependence is what one would expect from a bond saturation argument, which is often applied to explain the variation of bond strength with coordination in metals [177]: The Pt atoms near the edge of the surface have less neighbors thereby increasing the bond strength of each species they are bonded with.

The effect of coordination seems more pronounced for the atop and bridge position than for the fcc and hcp position which explains why the adsorption energy of OH varies more with particle size than that of oxygen. It is possible that as the adsorbed species binds with less Pt atoms (as in the atop position) it is much more sensitive to the extent to which that Pt atom is bonded with other Pt atoms.

While in general the adsorption energy on the 1nm particle on equivalent sites is higher than on the 2nm particle, this trend is reversed for the fcc(111) site. This peculiarity occurs because the surface facets on the 1nm particle have significant curvature in order to reduce the total surface area of the particle. This causes the distance between nearest neighbor Pt atoms to be longer on the surface of the 1nm particle (2.85 Å before O adsorption) than on the 2nm particle

(2.7 Å before O adsorption). This bond elongation reduces the extent to which adsorbed oxygen can simultaneously hybridize with all three Pt atoms defining the site.

Understanding how the variations of the adsorption energy with particle size affect catalysis is complex and depends on the precise role of the adsorbed species (O and OH in this study) in the catalytic process, and on the change in adsorption of other relevant species. It is now generally accepted that the specific CO oxidation rate increases as the particle size decreases [178-180]. Mayrhofer et al.[144] attributed this to the stronger OH adsorption on smaller particles, which provides the oxidant for CO. Our finding of a stronger OH adsorption would certainly corroborate this finding. The situation when Pt is used as a cathode for the oxygen reduction reaction is more complex. Watanabe et al. [181] argued that there is no effect of particle size on the rate of the ORR, but that the mean particle spacing on the support is the more relevant variable though his findings have been disputed by Giordano et al. [182] and Takasu et al. [183]. Similarly, Yano et al. [184] measured ORR catalytic activity and ratio of peroxide (H_2O_2) formation for particles 1.6, 2.6 and 4.8 nm in diameter. By using NMR analysis for ^{195}Pt located at surfaces of the Pt nano particles, they found that the electronic structure does not change with particle sizes, from which they suggested that the ORR activity does not change with Pt particle size. Mayrhofer et al. [144] on the other hand argue that the rate of the ORR will decrease with decreasing particle size since stronger OH adsorption removes sites for oxygen adsorption.

Recently, other investigations have pointed at the importance of under-coordinated sites on nanoparticles. Narayanan et. al. [185, 186] systematically investigated how the shape and particle size affect the catalytic activity of Pt nanoparticles: They found that the surface activity

of Pt is significantly sensitive to the number of under-coordinated sites, such as edges and vertices. More recently, Tian et al. [187] synthesized a tetrahexahedral Pt nanocrystal and observed it to have enhanced catalytic activity for electro-oxidation of small organic molecules. They rationalized this finding on the basis of the large number of under-coordinated sites on high index facets.

Our results indicate that adsorption on nanoparticles is significantly different from on flat bulk surfaces and quantitative results from bulk studies may be less relevant to nanoparticle catalysis than previously thought. While we find in general that the adsorption energies increase as the particle size decreases, consistent with a lack of bond saturation of the Pt atoms in small particles, the magnitude of the effect varies substantially with the type of site. Adsorption in low coordination, such as on the atop or bridge position changes much more significantly with particle size than adsorption energies in the higher symmetry hcp and fcc sites. How particle size will affect the adsorption of a species will therefore depend on the position in which it adsorbs. Hence, given that catalytic activity depends on the outcome of competitive adsorption between species, there may be no general trend to predict how catalytic activity of reactions changes with particle size. However, clever engineering of both the shape and size of catalyst particles, thereby optimizing the adsorption strength and number of adsorption positions for all the relevant species involved could, in principle, be used to design better catalyst, though such a study would require the evaluation of considerably more species than what has been presented in this paper.

Our results indicate that Pt nanoparticles may undergo oxidation/reduction reaction at different external conditions than bulk Pt metal. According to our calculated chemisorption

energies of O and OH, the smaller 1 nm Pt cluster will form surface oxide much more easily than 2 nm and Bulk Pt(111) surface. By using first principles DFT calculations Xu et al. [188] showed that small Pt clusters in the form of Pt_nO_m (in range of n=1~3) oxidize much easier than bulk Pt metal. Our results indicate that the stronger affinity to oxygen continues to 2nm Pt particle.

4.6 Conclusion

We investigated the effect of particle size and local surface structure on of the adsorption of O and OH on Pt. We found that adsorption energies of O and OH are sensitive to the coordination number and size of the Pt particles in some case changing by as much as 1 eV from the bulk to the 1nm particle. Low-coordinated sites show much stronger sensitivity to the particle size and surface structure than other sites. Although an electronic structure model such as the *d*-band center theory captures some overall tendencies of chemical reactivity as a function of Pt size and adsorption site, there is considerable deviation from this model at the vertex or edge sites.

Chapter 5

Electrochemical Modeling of Intercalation Processes with a Phase Field Model

5.1 Overview

In the previous three Chapters, environmental factors influencing the surface structures of Pt (or Pt based alloy) electrocatalysts are rigorously investigated on an atomic scale. In those studies quantum mechanical approach with first principles DFT calculations was extensively used. On the other hand, this chapter explores transport kinetics on the meso-scale regime by using a continuum modeling, *phase field model.*

While, classical Fick's law has been widely used for studying kinetics for example, the Li ion diffusion in the intercalating electrodes of secondary batteries, a phase field model is potentially more accurate and allows simpler tracking of phase boundaries than the Fick's equation. In this chapter, the phase model is implemented with highly accurate but computationally fast chebyshev spectral method. By simulating Li diffusion processes with the phase field model, important experimental techniques for measuring diffusion coefficients, such as GITT (Galvanostatic Intermittent Titration Technique) and PITT (Potentiostatic Intermittent Titration Technique) are investigated to the extent of which a non-Fickian behavior can affect results from these experiments. It is shown that GITT and PITT can still accurately measure the Li diffusion

coefficient in systems described by a phase field model even when significant gradient energy term, which is an energy penalty of having concentration gradients, are present.

5.2 Introduction

Lithium (Li) transport in rechargeable batteries is one of the essential factors that determine the rate at which a battery can be charged and discharged. There are extensive literatures on the modeling of a Li transport in rechargeable batteries [189-193]. This modeling has primarily relied on Fick's law to describe transport inside particles of the anode and cathode. Fickian diffusion can be derived from a local description of the free energy. If the free energy of a system also depends on gradients in its state variables (such as concentration) or fully non-local variable (such as boundary conditions for systems under stress [194]), more elaborate kinetic theories are required. Even for Fickian systems, diffusion through multiphase systems are particularly demanding, and while elaborate boundary tracking methods have been used to deal with multiphase systems [195], these methods pose significant computational challenges. Phase field model [196-199] represents potentially a powerful tool for modeling of Li batteries because it is more accurate in regions with sharp gradients of the composition and allows treatment of phase boundaries without explicitly tracking interfaces. This chapter describes the phase field model and uses it to simulate electrochemical properties of topotactic intercalation in a two-phase system. The phase field model is implemented with a highly efficient Chebyshev spectral method [200-202].

The Galvanostatic Intermittent Titration Technique (GITT) and Potentiostatic Intermittent Titration Technique (PITT) methods [203, 204] are the standard experimental techniques used to measure Li transport properties in Li batteries. The extraction of diffusion constants from both GITT and PITT relies on Fick's diffusion equation, so it is not obvious, a priori, how these methods relate to the quantities in a non-Fickian phase field model. Hence, it is necessary to assess the impact of non-Fickian behavior in GITT and PITT by simulating both techniques with a phase field model for the dynamics.

The goal of this chapter is to describe the basic theory of phase field models in the context of Li battery modeling, and then use their ability to incorporate non-Fickian behavior to estimate the errors introduced by Fickian approximations in standard GITT and PITT measurements. All tests are done on a model of two-phase system. Although this model is simple, it is relevant for many battery materials, and highlights the essential issues that might arise in other systems.

This chapter consists of seven sections. Section 5.3 introduces the phase field model and the spectral method used to solve it. Section 5.4 describes the GITT and PITT methods and the approximations inherent in their use. Section 5.5 describes a model system. A phase field model is applied to GITT and PITT in the section 5.6 and 5.7, which is followed by discussion (section 5.8) and conclusion (section 5.9).

5.3 The Phase Field Model and Spectral Method

5.3.1 Phase field models

In a phase field model the time evolution of a property ("the field") is governed by the gradient of a free energy functional. Depending on whether the field is a conserved quantity or not, this is formulated by either the Cahn-Hilliard or Allen–Cahn equation [205, 206]. This chapter considers a topotactic intercalation compound in which Li ions reside in interstitial sites of a crystalline host structure. In topotactic compounds, the different phases that appear during intercalation are characterized by a different concentration and hence the local Li concentration can serve as a field variable. The concentration field, which is a conserved property, evolves by long-range diffusion. Hence, a description of diffusion and phase transformations within the electrode material can be modeled with a Cahn-Hilliard formulation. On an atomic scale, Li transport in topotactic intercalation compounds occurs through interstitial diffusion involving exchanges with adjacent vacant sites [207].

The total free energy of solid (F_s) containing concentration gradients can be cast in the following form (neglecting strain energy)

$$F_s = N_V \int_V \left[f_h(c) + \widetilde{K}(\nabla c \cdot \nabla c) \right] dV \tag{5-1}$$

where, c is a concentration, $\widetilde{K}$ denotes a gradient energy coefficient, N_V is a number of atoms per unit volume, and f_h means free energy densities of a topotactic lithium intercalation compound with a homogeneous lithium concentration. To calculate the total free energy of a non-homogenous solid, f_h is evaluated at the local concentration. The gradient energy term can be understood physically as the energy penalty of having concentration gradients. In the presence

of concentration gradients, the thermodynamic driving force for a diffusion potential,(χ) , can be shown to be [205]

$$\chi = \frac{\delta F_s}{\delta c} = N_V \left[\frac{\partial f_h}{\partial c} - 2\tilde{K}\nabla^2 c\right] \tag{5-2}$$

where for a topotactic lithium intercalation compound the partial derivative of f_h with respect to the concentration (c) is equal to the lithium chemical potential. If the flux is assumed proportional to the gradient as is usually done in kinetic theory, the flux (J) for an interstitial diffuser such as Li can be written in one dimension as

$$J = -L\frac{d\chi}{dx} = LN_V\frac{d}{dx}\left[\frac{df_h}{dc} - 2\tilde{K}\frac{d^2c}{dx^2}\right] \tag{5-3a}$$

where x is the spatial variable and L is kinetic coefficient. This flux expression can be written in a more familiar form as

$$J = -N_V L\frac{d^2 f_h}{dc^2}\frac{dc}{dx} + 2LK\frac{d^3 c}{dx^3} \tag{5-3b}$$

where K is the gradient energy coefficient, which is a $\tilde{K}$ multiplied by the number of atoms per unit volume (N_V). In this form, the connection between the Cahn-Hilliard flux equation and Fick's flux equation becomes more obvious. Indeed, Fick's equation for interstitial diffusion can be recovered from Eq. (5-3b) by setting the gradient coefficient (K) equal to zero. In that case, the chemical diffusion coefficient is simply

$$D_{chem} = N_V L\frac{\partial^2 f_h}{\partial c^2} = N_V L\frac{kT}{c}\Theta \tag{5-4}$$

where, k and T denote the Boltzmann constant and absolute temperature. Θ is a thermodynamic factor which is defined as [208].

$$\Theta = \frac{c}{kT}\frac{\partial^2 f_h}{\partial c^2} \tag{5-5}$$

In Eq. (5-3b), the driving force for diffusion not only depends on the gradient of the local chemical potential, which itself depends on the local gradient in concentration, but also on higher order derivatives of the concentration profile. With Eq. (5-3) the continuity equation expressing the conservation of concentration becomes

$$\frac{\partial c}{\partial t} = \frac{\partial}{\partial x}\left[L\frac{\partial}{\partial x}\left(\frac{\partial f_h}{\partial c} - 2\tilde{K}\nabla^2 c\right)\right] \tag{5-6}$$

Eq. (5-6) is the differential equation that describes the evolution of a solid that can undergo compositional changes and diffusional phase transformations on the same parent lattice. This makes it ideally suited to study topotactic intercalation compounds. Three materials quantities appear in the Cahn-Hilliard Eq. (5-6): the homogeneous free energy density (f_h), the kinetic coefficient (L), and the gradient energy term ($\tilde{K}$). In general, all three quantities are expected to be concentration and temperature dependent. The free energy can be determined experimentally by integrating the lithium chemical potential, which is linearly related to the measured open cell voltage profile. The kinetic coefficient for diffusion, (L), can be measured by performing diffusion coefficient measurements. At present, no experimental techniques have been devised to measure the gradient energy term, ($\tilde{K}$).

5.3.2 Effective Diffusion Coefficient

Several experimental methods exist to determine diffusion coefficients under conditions when Fick's flux equation is sufficiently accurate (i.e. moderate concentration gradients). Furthermore, well established methods are available to calculate diffusion coefficients from first principles [208, 209]. It is unclear though how these diffusion coefficients are related to the kinetic parameter (L) that appears in the Cahn-Hilliard equation. Only in the limit of small $\widetilde{K}$ or small rate of the curvature, variation in the concentration profile does the Cahn-Hilliard flux equation map onto Fick's flux equation.

While solids are expected to have a non-zero gradient energy term, experimental measurements of diffusion coefficients that rely on the validity of Fick's equation implicitly assume $\widetilde{K} = 0$. In this context, we can define an *effective chemical diffusion coefficient* when the gradient energy coefficient is not zero by casting Eq. (5-3b) into the same form as Fick's diffusion equation

$$J = -D_{chem}^{eff} \nabla c \tag{5-7}$$

With

$$D_{chem}^{eff} = N_V L \frac{\partial^2 f_{homo}}{\partial c^2} - 2\widetilde{K} N_V L \left[\frac{\partial^3 c}{\partial x^3} \Big/ \frac{\partial c}{\partial x} \right] = D_{chem} - 2KL \left[\frac{\partial^3 c}{\partial x^3} \Big/ \frac{\partial c}{\partial x} \right] \tag{5-8}$$

One can see from Eq.(5-8) that there are two terms in the phase field model equation for the effective diffusion coefficient. The first term is identical to that found in Fick's law. The second

one is called a gradient energy term, and it depends on the strength of the gradient energy coefficient ($\tilde{K}$), and higher order derivative of the concentration profile. When the gradient energy term is large compared to the first term, the system will not be well described by Fick's law. This could occur in regions close to spinodals, where D_{chem} approaches zero as the thermodynamic factor approaches zero at the spinodal point, or in the inhomogeneous systems where the concentration profile is characterized by a strongly varying curvature, for example, across an interface. It is not known how the gradient energy term might influence the results of GITT and PITT measurements.

5.3.3 Chebyshev Spectral Method

To perform diffusion simulations with the phase field model, Eq.(5-6) needs to be solved with proper boundary conditions. Since this is a partial differential equation, we need numerical schemes for both time and space evolution. We chose a spectral method to discretize the spatial component, as it is more accurate than the Finite Difference Method (FDM) or Finite Element Method (FEM) for the same number of grid points. In the spectral methods, the error decays exponentially with the number of grid points, unlike with FDM or FEM, which have only an algebraic convergence [200]. In the spectral method, the unknown solution (concentration in the present context, c), is expanded in basis functions (Φ_k) up to some truncation order (N).

$$c(x) \cong c_N(x) = \sum_{k=0}^{N} a_k \Phi_k \tag{5-9}$$

Chebyshev polynomial is used for a basis function (Chebyshev spectral method), which produces a non-uniform grid, much denser near the boundaries of the particle. Its grid points are the projections onto the horizontal axis of equally spaced grids on a unit circle and the density of the grids is expressed as Eq. (5-10) below [201]

$$N \to \infty,\ density \approx \frac{N}{\pi\sqrt{1-x^2}} \tag{5-10}$$

To minimize the impact of error due to truncation (residue) we use the pseudo spectral method [200, 202], in which the expansion coefficients are calculated by requiring that the residue vanishes at the grid (collocation) points. The Cahn-Hilliard equation is very stiff and converges slowly with typical numerical schemes, such as the Euler method or the Crank-Nicholson method [210-212]. Therefore, for the time marching scheme, the 'ode15s' package built in Matlab [213] was used which is optimized for stiff differential equations and uses a variable order method.

5.4 The GITT and PITT Methods

5.4.1 GITT

Weppner and Huggins introduced the Galvanostatic Intermittent Titration Technique (GITT) [203, 204]. In GITT, a system is perturbed by imposing a constant current (I_o) for some time interval (τ), and measuring the potential (E) as a function of time (t). Assuming constant diffusivity of the diffusing species and a semi-infinite solid, the evaluation of the surface

concentration (and hence the potential) can be found by solving Fick's equation with appropriate boundary conditions. By comparison, of the measured voltage to this analytical solution, the chemical diffusion coefficient can be obtained. The fundamental equation used in GITT is

$$D_{GITT} = \frac{4}{\pi}\left[\frac{1}{SFz_A}\right]^2 \left[I_o \left(\frac{dE}{dc}\right) / \frac{dE}{d\sqrt{t}}\right]^2, \quad \left(t \ll \frac{r^2}{D_{GITT}}\right) \tag{5-11}$$

The quantities z_A, F and S are respectively the charge number of the ion, the Faraday constant, and the particle area exposed to the current. The quantities I_o, r and E are the galvanostatic current step, particle length, and the measured voltage, respectively. This equation is valid when the measuring time is short enough so that the particle behaves as semi-infinite solid. For small currents and short time steps (τ), $\frac{dE}{d\sqrt{t}}$ and $\frac{dE}{dc}$ are approximated by

$$\frac{dE}{d\sqrt{t}} \approx \frac{\Delta E_t}{\sqrt{\tau}} \tag{5-12}$$

$$\frac{dE}{dc} \approx \frac{\Delta E_s}{\Delta c} \tag{5-13}$$

where ΔE_t denotes the total transient voltage change after time τ and ΔE_s corresponds to the change of the steady-state voltage. With these relations and by relations between the quantities of S, F, z_A and I_o, Eq. (5-11) is transformed into simpler form.

$$D_{GITT} = \frac{4r^2}{\pi\tau}\left[\frac{\Delta E_s}{\Delta E_\tau}\right]^2 \tag{5-14}$$

where, ΔE_τ is the total transient voltage change of the cell for applied current for time τ and ΔE_s is the change of the steady-state voltage of cell for this step.

5.4.2 PITT

In the Potentiostatic Intermittent Titration Technique (PITT), the system is perturbed with a potential step and the current is measured as a function of time [214]. In a standard PITT analysis, the particle is assumed to initially have a homogeneous concentration. Based on the solution to Fick's equation, the concentration and current profile as a result of the potential step can be calculated in terms of the diffusivity. Using these relations the diffusivity can be obtained from the measured current using.

$$I(t) = zFs(c_s - c_o)\left[\frac{D_{PITT}}{\pi t}\right]^{\frac{1}{2}}, \quad \left(t \ll \frac{r^2}{D_{PITT}}\right) \tag{5-15}$$

The quantity $(c_s - c_o)$ denotes the concentration difference at the surface at time t and at time $t=0$, which should be constant due to the constant potential boundary condition. This expression is known as the Cottrell equation. In an experiment, it is impossible to measure $c_s(t)$ directly and it is estimated from the total charge (ΔQ) transferred to the system after the system has completely equilibrated with potential step

$$\Delta Q = \int_0^{\infty} I(t)dt = zFnV_M(c_s - c_o) \tag{5-16}$$

In Eq. (5-16), n and V_M denote the number of gram atom and the molar volume of the component where Li ions intercalate, respectively. Inserting this equation into Eq.(5-15) we obtain.

$$D_{PITT} = \pi r^2 \left[\frac{max\,(I\sqrt{t})}{\Delta Q}\right]^2 \tag{5-17}$$

If the current decay follows the Cottrell equation, $I\sqrt{t}$ is constant. But in real systems it is not constant and instead max ($I\sqrt{t}$) is used [191, 193]. Practically, ΔQ is usually taken as the charge transferred when the current has decayed to less than 1 % of its initial value. Thus, the charge calculated by integrating the current up to this time always underestimates the concentration difference ($c_s - c_o$). In this paper 1, 0.1 % and effectively infinite decay times were used to estimate the effect of integration time. For voltage steps, we explored values of 1, 5 and 10 mV.

5.5 Model System

In order to model a physical system with the phase field model described by Eq.(5-6), it is necessary to have a free energy function (f), a kinetic coefficient (L), and a gradient energy term ($\tilde{K}$). We consider a simple two-phase system, which is relevant to portions of the Li composition range of many cathode materials. In particular, the important new Olivine Li_xFePO_4 material is well known to have a two-phase region over almost its entire concentration range at room temperature [215]. For our two-phase model, we use a mean-field free energy curve of the form:

$$F(c,T) = N_V[\Omega c(1-c) + kT(c\,log_e\,c + (1-c)\,log_e(1-c))] \qquad (5\text{-}18)$$

where, Ω is a constant and is related to the nearest-neighbor interaction strength between lithium ions within the host. Fig. 5-1 shows our free energy functional at room temperature, with set Ω to 59 meV which at room temperature gives a broad two-phase region in the concentration range of (0.20 ~ 0.80).

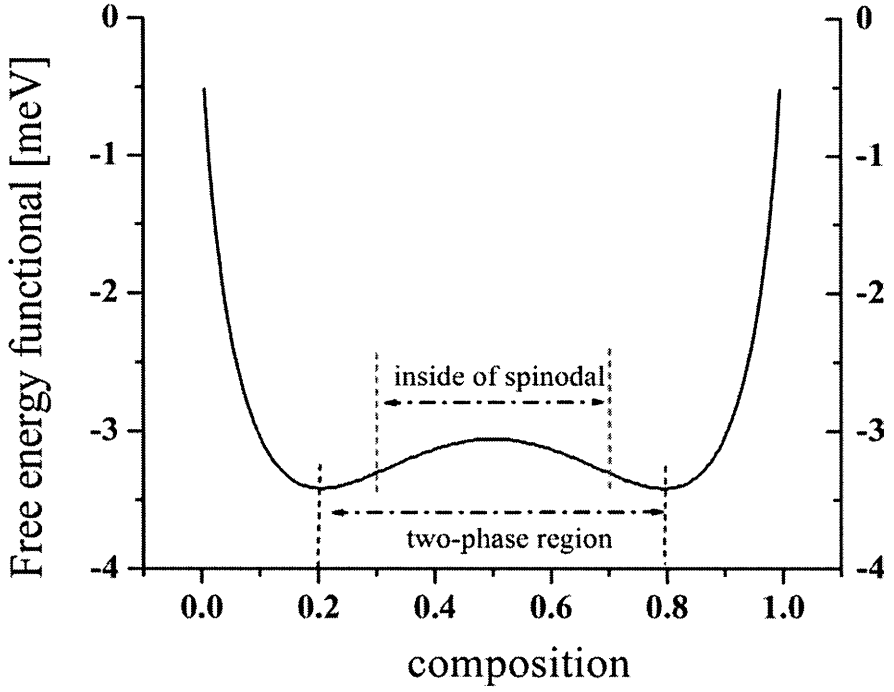

Figure 5-1: Free energy functional for a model system at room temperature

The spinodal instability lies between 0.30 and 0.70. Spinodals correspond to the concentrations where the curvature of the free energy is zero. A uniform solid with composition between the spinodals is unstable and spontaneously decomposes into a mixture of two phases. The results below only pertain to the stable concentration ranges up to the spinodals. It should be noted that the solid is metastable between the two-phase boundaries and the spinodals. This may or may not be experimentally accessible, depending on the kinetics of the system, and is shown primarily to allow easy identification of trends that peak at the spinodal points. For given value of Ω, assuming a nearest neighbor regular solution model parameter, a value for $\tilde{K}$ can be derived, which for a one-dimensional lattice like that in $LiFePO_4$, takes the form [205]

$$K = \frac{1}{2}\Omega\left(\frac{1}{3}a^2\right) \tag{5-19}$$

where, a is the nearest neighbor distance. With N_V =8.40×10^{28} (/m^3), a = 2.5 Å, Ω =59 meV Eq. (5-19) gives K ($\equiv N_V\tilde{K}$) as 2.48×10^{-11} (J/m). For the model system, we assume $L = L_o c(1-c)$, where L_o is a constant independent of lithium. This form for L would give a constant Fickian diffusion coefficient for an ideal solution model (in which the thermodynamic factor Θ = 1 for all concentrations) so that all composition dependence in our model arises from the energetic term. The kinetic coefficient $L_o = 2.71 \times 10^{-14}$ $(m^2/J.\text{sec})$ was chosen to give physically reasonable values of the diffusion constant, in the 10^{-15}~10^{-17} (m^2/sec) range.

5.6 Results for GITT

In order to test the role of gradient energy terms in GITT, we have simulated GITT experiments on our model system described in Sec.5.4. All simulations were performed with a single one-dimensional particle with length $r = 1$ μm (so no effect of a particle size distribution is considered). As discussed above, the base gradient energy coefficient was set to $K = 2.48 \times 10^{-11}$ $\left(\frac{\mathrm{J}}{\mathrm{m}}\right)$. In order to check the effect of the gradient energy coefficient two other values of K, an order of magnitude smaller and larger than the base value, were also used. Simulations were also performed with $K = 0$ to test the errors inherent in the GITT model, even without a gradient energy term. In our simulations, constant current was imposed on one side of the particle, with an impermeable boundary condition on the other side. The current pulse strength corresponded to a *c*-rate of a *c/60* ($= 1.081\ \mu A/\mathrm{cm}^2$) and the pulse lasted for 10 sec. This time is significantly shorter than the time at which finite size effects occur (simple arguments show that the finite size effects become important at $t = r^2/D_{chem}$, which in our case is $\approx$ 2500 sec) [191]. For each current density, the total amount of Li added (or subtracted) from the particle by the current pulse corresponds to a concentration change of less than 0.1 %. In each case the chemical diffusion coefficient was extracted from the voltage response by GITT simulation, D_{GITT} (m^2/sec) with Eq. (5-14) and compared to the true chemical diffusion coefficient D_{chem} (m^2/sec) in Eq. (5-4)). The results are shown in Fig. 5-2. Fig. 5-3 shows the same results as percentage errors in the calculated values of D_{GITT} compared to D_{chem} (defined by $100\times(D_{GITT} - D_{chem})/D_{chem}$).

Errors intrinsic to the GITT method come from a number of assumptions used to derive a tractable expression for experimental analysis. The key approximations that lead to errors are summarized here.

(1) One-dimensional semi-infinite particles: GITT assumes particles with simple geometries (i.e. one-dimensional cylindrical or spherical geometries) that are large enough such that finite size effects can be neglected.

(2) Fickian dynamics: GITT assumes that the transport is described by Fick's equation, with no gradient energy term.

(3) Constant diffusion coefficient during perturbation: GITT assumes that during the current pulse the diffusion coefficient does not change as the concentration changes.

(4) Constant $\frac{dE}{d\sqrt{t}}$, $\frac{dE}{dc}$ (see Eq. (5-12) and (5-13)): GITT assumes that these derivatives are constant to make it possible to write the diffusion coefficient in terms of experimentally accessible quantities.

(5) Small current pulse: GITT assumes that the current pulse is small and short enough that the above approximations hold.

(6) Extra-particle dynamics: GITT assumes no impact on the voltage response from the dynamics outside the particle (in the electrolyte or at the electrolyte/particle interface).

In Fig. 5-3 we see that for $K = 0$ the errors are extremely small, amounting to less than five percent of the true value of the diffusion coefficient. To the extent that there are any errors at all, they would come from approximations 3 and 4, since the use of a short time pulse and $K = 0$ assure that approximations 1 and 2 are valid. The extremely high accuracy of the GITT method

for K=0 is somewhat misleading. More detailed analysis shows that there are significant errors in the approximations 3 and 4, but that the errors cancel, giving a very accurate final estimate for the diffusion coefficient. At this time, it is not clear if this cancellation is a fortuitous result of our specific simulation parameters, or if it is likely to occur in general.

For $K \neq 0$ the value of D_{GITT} increases with increasing K. This makes intuitive sense, since larger K reduces gradients by energetically penalizing them, enhancing the effective diffusion coefficient. In particular, larger values of K reduce the surface concentration gradients built up during the current pulse, causing the transient voltage to be reduced (reducing ΔE_t in Eq. (5-12)), and increasing D_{GITT}.

The errors increase significantly as the concentration approaches the spinodal. This is presumably due to changes in the transport properties. At the spinodal the thermodynamic factor goes to zero, which means the diffusion coefficient is also going to zero (see Eq.(5-4), (5)). This will cause large gradients in the system, and decrease the accuracy of approximations 2 and 3, and possibly 4 as well. However, even with quite large values of K the errors are within 10 % in the stable region of the two-phase model. For this reason, we do not think that the presence of a gradient energy term causes a significant deviation between measured diffusion constants and the true D_{chem}. This means that experimentalists can trust D_{GITT} to give a good representation of D_{chem} independent of the gradient energy terms in the material, and phase field models can use D_{chem} from experiment even in models with significant gradient energy terms.

It should be noted that our simulations treat only dynamics within the cathode particles, and therefore the simulated voltage response does not include any extra-particle dynamical effects. This is equivalent to assuming infinitely fast extra-particle kinetics. Therefore, in our

simulations, approximation 6 above is met exactly. This restriction in our simulations allows us to focus on the impact of non-Fickian diffusion, but it is not meant to imply that these effects are unimportant sources of error in real experiments.

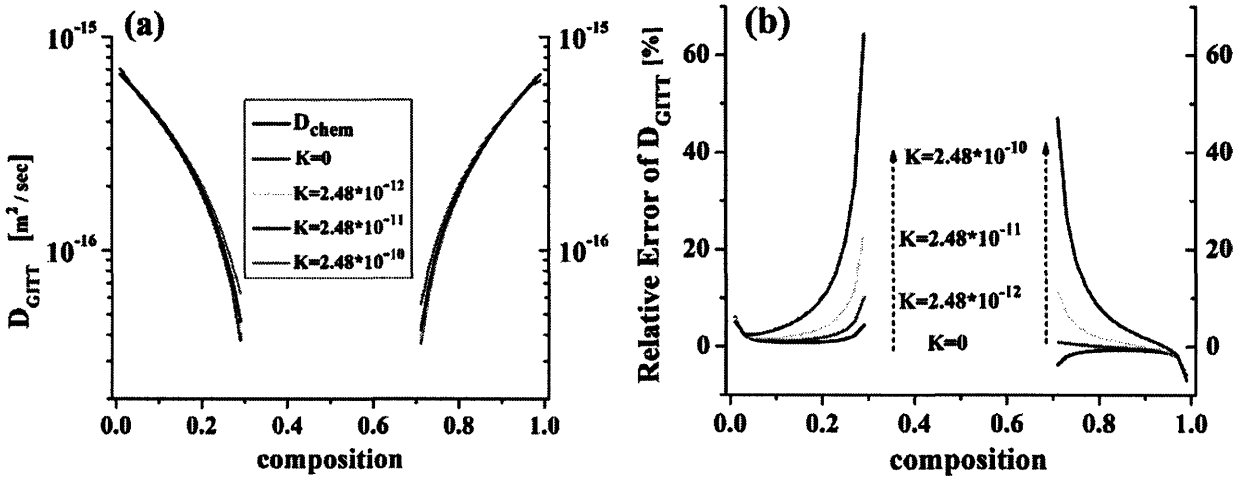

Figure 5-2: Chemical diffusion coefficient by GITT as function of gradient energy coefficient in (a) and in (b) relative errors of D_{GITT} diffusion coefficient with current density j = 1.081 (mA/cm^2) in (a).

5.7 Results for PITT

All PITT simulations were performed for the same particle size and range of K values as the GITT simulations. The time for current integration (t_{int}) was chosen when the initial current decayed to 1 % of its initial value and the voltage step (ΔE) was set to 1 mV. The chemical diffusion coefficient was extracted from the voltage response by PITT simulation D_{PITT} with Eq. (5-17) and compared to the true chemical diffusion coefficient (D_{chem}) in Eq. (5-4). The results are shown in Fig. 5-4. Fig. 5-5 shows the relative error of diffusivity extracted from PITT (defined by $100\times(D_{PITT} - D_{chem})/D_{chem}$). Note that the concentration range on either side of the spinodals is not symmetric around c = 0.5. This is because the voltage step in PITT always increases the concentration, and one cannot actually step into the spinodal. This imposes a maximum concentration to the left of the lower spinodal.

Errors intrinsic to the PITT method come from a number of assumptions used to derive a tractable expression for analysis. The key approximations that lead to errors are summarized here.

(1) One-dimensional semi-infinite particles: PITT assumes particles with simple geometries (i.e. one-dimensional cylindrical or spherical geometries) that are large enough such that finite size effects can be neglected.

(2) Fickian dynamics: PITT assumes that the transport is described by Fick's equation, with no gradient energy term.

(3) Constant D during perturbation: PITT assumes that during the voltage step the diffusion coefficient does not change as the concentration changes.

(4) Cutoff current: PITT assumes an infinite time integration, which must be truncated after some practical interval.

(5) Small voltage step: PITT assumes that the voltage step is small enough that the above approximations hold.

(6) Extra-particle dynamics: PITT assumes no impact on the current response from the dynamics outside the particle (in the electrolyte or at the electrolyte / particle interface).

In Fig. 5-5 we see that for K = 0, the errors are much larger than for GITT, and can reach about 450 % near the spinodal. In the stable regions, the errors are generally much smaller, around 30-50 %. These errors are due to approximations 3, 4, and 5. The errors are not very large, but as they might be larger in some cases, we take this opportunity to point out that they can be significantly reduced by some rather simple adjustments to the traditional PITT method.

The errors due to approximation 4 can be decreased by increasing t_{int}. It can be shown analytically from the Cottrell equation that the error relative to 1% decay of current in D_{PITT} from t_{int} is proportional to I_{cut}^2, where I_{cut} is the percentage of the initial current at which the integration stops. For example, the relative error at I_{cut} = 1 % is 100 times bigger than I_{cut} = 0.1 %. This makes it seem that highly accurate results require impractically long integration times. However, real systems stop following the Cottrell equation after times on the scale of $t = \frac{r^2}{D}$, at which point the current will decay at a greatly accelerated rate, since the back of the particle has been reached. Therefore, by setting t_{int} to slightly larger than $t = \frac{r^2}{D}$, quite good convergence can be obtained. The simulated current vs. time for a typical PITT voltage step is shown in Fig. 5-6.

As expected, a deviation from Cottrell behavior and a sharp drop in current occurs near $t = \frac{r^2}{D}$. By setting t_{int} using I_{cut} = 0.1 %, instead of I_{cut} = 1 %, t_{int} increases only by a factor of 3 (rather than the factor of 100 expected from the Cottrell equation) and the errors seen in Fig. 5-5 are generally reduced by about a factor of two.

The errors due to approximation 5 can also be easily reduced by using a variable voltage step. These errors are more pronounced if one is using a larger voltage step (for example, with ΔV = -10 meV we found errors about twice as large as for 1 meV). The errors from a voltage step are generally due to large concentration gradients near the surface, which create errors due to approximation 3. For a fixed voltage step, the concentration step can be quite varied, according to the relations $\Delta E / (\frac{dE}{dC}) = \Delta c$. For flat voltage curves, even a small step in voltage can create large changes in concentration and gradients at the particle surface. By using the known voltage curve, PITT can be performed with constant concentration steps Δc_o by setting $\Delta E = (\frac{dE}{dc}) \Delta c_0$. A simple test of this approach in our simulation, using $\Delta c_0 = 10^{-3}$, decreases the errors in Fig. 5-3d by a factor of 2. Note that using $\Delta c_0 = 10^{-3}$ would require 1000 steps for the whole concentration range, quite comparable to the number of 1 mV steps that might be needed. There is experimental evidence that approximation 5 can easily introduce errors [216]. The authors in Ref. 26 measured the Li ion chemical diffusion coefficient in two electrode systems, one showing a first order phase transition and the other solid solution formation. In the case of the electrode with a phase transition, it was seen that a smaller potential step was needed around the phase transition region to measure the chemical diffusion coefficient more accurately.

Fig. 5-4 shows the unexpected result that the deviations in D_{PITT} from D_{chem} are essentially independent of K. This is presumably due to the specific boundary condition of PITT, which fixes the surfaces concentration. This makes it hard for K to influence the surface gradients and affect the results. Detailed examination of the calculations shows that for almost all our PITT simulation conditions the gradient energy term in Eq. (5-8) is at least 100 times smaller than the first term. This means that K will have little impact on the current flux and the PITT results. As with GITT, this is very good news, as it allows us to continue to rely on PITT results in the phase field context.

As with GITT above, PITT approximation 6 above is also met exactly in our simulations. For PITT it has been shown that this approximation can be a very significant source of error, as pointed out by in References [191, 217]. For example, Deiss shows that the PITT boundary condition creates a spurious potential dependence of the diffusion coefficient measured by PITT. Therefore, we wish to stress that the approximation of infinite extra-particle dynamics has not been tested here and may be a dominant source of error in real diffusion constants measured by the PITT method.

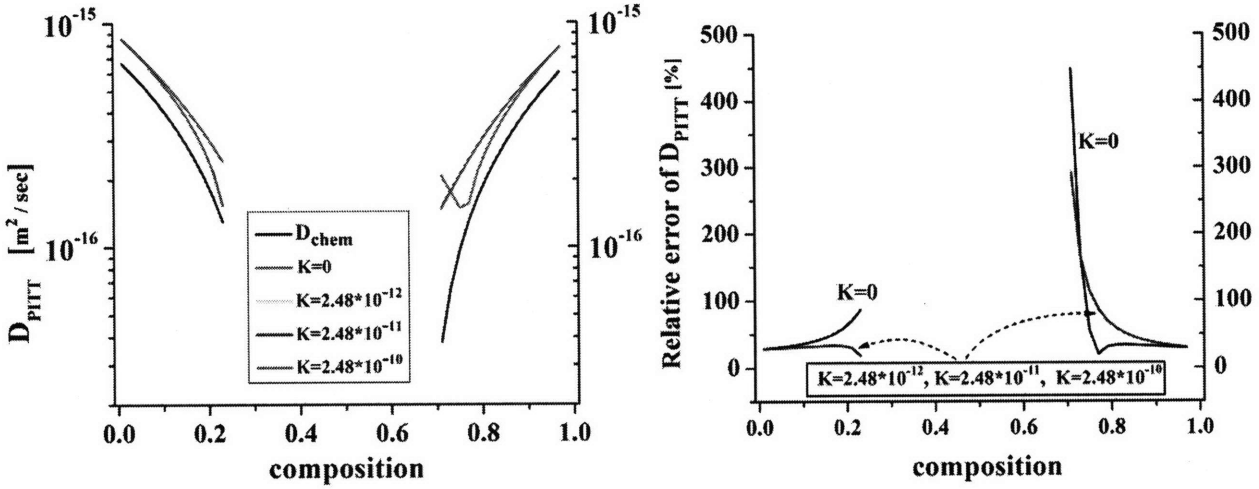

Figure 5-3: Chemical diffusion coefficient by PITT as function of gradient energy coefficient in (a) and in (b) relative errors with constant I_{cut} (1%) and voltage step -1 mV.

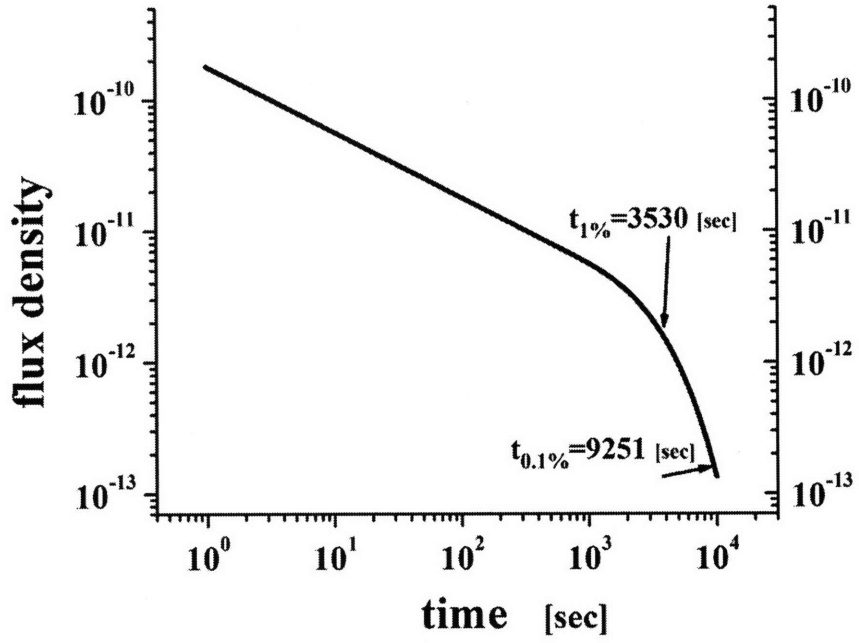

Figure 5-4: log-log plot of current density vs. time at two-phase limit (c = 0.19) with K = 2.48*10^{-11} (J/m).

5.8 Discussion

The Phase field model is a more general approach to the diffusion problem, especially when several phases are present. It is based on linear kinetics with a driving force proportional to a generalized diffusion potential, which includes a gradient energy term. It is capable of simulating single phases and interfaces simultaneously. In order to assure accuracy, we have used an efficient numerical algorithm, the Chebyshev spectral method, which has a much higher accuracy than the traditional finite difference or finite element methods.

We have performed detailed simulations of GITT and PITT experiments for a phase field model and a simple two-phase system, and discussed sources of error. These results are important since GITT and PITT are based entirely on approximations to Fick's equation, and their accuracy in the presence of a gradient energy term has not been previously established. We find that for our model system both techniques give reliable predictions for the chemical diffusion coefficient, even in the presence of a significant gradient energy term. This establishes the validity of GITT and PITT for real systems with large gradient energy terms. In addition, it shows that phase field modelers can use diffusion coefficients measured with GITT and PITT (or diffusion coefficients calculated from first principles for that matter) in phase field models without worrying about introducing large inconsistencies. Although our model system is relevant for many battery systems, it is possible that greater errors in GITT and PITT might occur for other systems.

We found that PITT is generally somewhat less reliable than GITT, but even for the worst case results, near the spinodal in the metastable region, the error in the PITT measured diffusion coefficient was only a factor of 3~7 (depending on voltage step) compared to the true value. We

suggest that using a longer cutoff time (larger than r^2/D), and using variable voltage steps to minimize concentration gradients, could each reduce errors by about a factor of two.

Having demonstrated that measurements of diffusion coefficients with GITT and PITT do not depend significantly on the gradient energy term, K, we can be confident in using phase field models to study intercalation in electrodes with experimentally measured or calculated Fickian diffusion coefficients. In fact, the phase field model is ideal to study intercalation that involves diffusional phase transformations, as no special computational schemes to track interfaces between different phases are required. In the phase field model, the gradient energy term makes it possible to have a steep concentration gradient corresponding to the interface between two phases with different concentration. The concentration within the interface region characterized by a large concentration gradient spans all values within the two-phase coexistence region, including all values within the spinodal. Without the gradient energy term (i.e. purely Fickian behavior), concentrations within the spinodal region are unstable, as the diffusion coefficient is then negative due to the negative curvature of the free energy. Simulating systems in which several phases can exist, as in the case of a miscibility gap, with only a Fickian diffusion equation requires the introduction of an explicit interface, which needs to be tracked. This is often done with shrinking and expanding grids [218]. In the phase field model, explicitly tracking interfaces is not necessary and new phases can spontaneously form once the local concentration crosses into the spinodal region. Fig. 5-7 shows a concentration profile when Li ions are extracted from cathode materials. Initially the system had homogeneous concentration (0.9) and Li ions were extracted with *C/10* (hr) *C*-rate. The simulation was stopped when the surface concentration reached 0.1.

It must be noted though that while new phases can form in phase field simulations once the local composition enters the spinodal region, such phases can form before that through a nucleation and growth mechanism. Nucleation and growth can occur for local compositions between the phase boundaries of the miscibility gap and the spinodal. While in the current study we have neglected nucleation and growth, it is straightforward to simulate the formation of new phases through nucleation with a phase field model, as has been demonstrated by Chen and A. Finel et al. [219, 220].

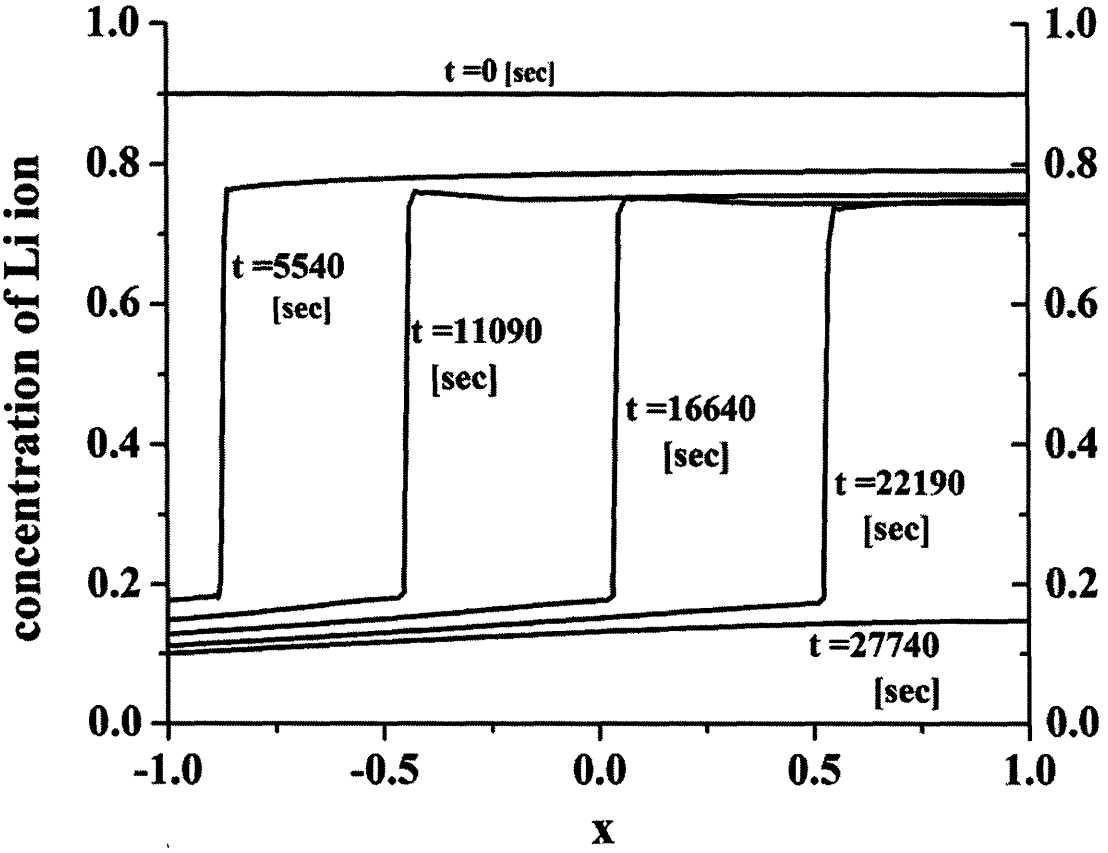

Figure 5-5: Concentration profile of Li ion in charging processes. From initially homogeneous concentrations ($c = 0.9$), at time $t = 27740$ sec, it reached 0.1 with $C/10$ (hr) C-rate.

5.9 Conclusion

We have investigated the phase field model in the context of topotactic intercalation. The phase field model, based on the Cahn-Hilliard equation, can be used to simulate both diffusion and diffusional phase transformations simultaneously. Because of the gradient energy term, it is possible to model diffusion in several phases as well as the interfaces between phases without having to track the interfaces explicitly. We have investigated, with a model system for which all parameters of the Cahn-Hilliard equation are pre-assigned, the accuracy of the experimental GITT and PITT techniques in determining diffusion coefficients. We find that even though GITT and PITT are based on Fick's equation, these methods are capable of accurately determining diffusion coefficients even for a non-zero gradient energy term. This paves the way for the use of phase field models to simulate electrode characteristics using diffusion coefficients measured with conventional experimental techniques.

Although in this chapter, the phase field models are applied to estimate diffusion kinetics, they are also very powerful tools to simulate and predict the evolution of complex microstructure morphology. For example, they have been applied to many materials science fields, such as, diffusion controlled phase decomposition (nucleation, Spinodal decomposition, Ostwald ripening, etc.), order-disorder transition, dendrite growth, effect of applied field (stress, magnetic and electric field, etc.). An ab-initio approach to these fields may not be impossible, phase field models have advantages in the scale of both computation time and particle size of the model systems they can treat. The two methodologies, first principles DFT calculations and phase field models of continuum theory, however, can have very useful interactions. Most of input parameters of the phase field model are obtainable by an ab-initio method without fitting to the

experimental results. The parameters, in turn, enable phase field models to evaluate the (surface and bulk) microstructure evolutions in the macroscopic time and size scales. In this point of view, the surface structures of Pt-based alloy electrocatalysts, which are treated in the chapter 2, are neatly studied by the phase field model. Electrocatalyst particles are never uniform and the particles are always distributed in their sizes and surface morphologies. As such, phase field model can handle the long-term variation of the surface structures in those situations (size and morphology distribution), which lead to better estimation of the activity-surface structure relationship.

Chapter 6

Conclusion

It has been of interest to elucidate a detailed mechanism how electrocatalytic activity is modified as a function of its surface structure and size. However, over the last decades concerted theoretical and experimental studies were not able to find out a fundamental rationalization of the effects.

This thesis was aimed at figuring out a relationship between surface reactivity of Pt based alloy electrocatalyst and its surface structure on the atomic scale. An accurate and consistent approach was used for the purpose. First principles DFT method was intensively employed to quantify energetics of a system accurately from which ground state structures and compositions of the catalyst surfaces are obtained. In addition, chemisorption energies of various atomic or molecular chemical species were precisely predicted. The energetic information obtained by the *ab-initio* DFT calculations is extensively utilized to characterize the surface structure, composition and hence, activity of electrocatalyst as a function of relevant model systems. In chapter 2, we characterized detailed surface structures of bulk Pt-alloy catalysts under both vacuum and non-vacuum conditions. For the purpose, we developed a rigorously statistical mechanical methodology, Coupled Cluster Expansion (CCE), which can parameterize the interacting potentials of all adsorbates and catalysts atoms from energetic information calculated by *ab-initio* DFT method. Hence, CCE enabled Monte Carlo simulation to explore whole

configurational spaces of electrocatalysts and adsorbates with temperature and chemical potentials as controllable variables. Figure 2-7 showed an example for the surface structures of O/Pt-Ru alloy catalysts. It was found that in a mild oxidation condition, Ru significantly segregates to the surface and forms island structure with O. A good activity of Pt-Ru alloy to CO oxidation was discussed in terms of the surface structure.

By using ab-initio DFT method, it was shown that electrocatalytic activity of Pt-alloy is influenced by the lateral interactions between adsorbates, and alloying elements. Chemisorption energy of CO on Pt(111) surface was considerably influenced by coadsorption of O or OH and Ru alloying as shown in Fig. 3-10. It was found that surface relaxation and strain fields on the catalyst surface were underlying mechanism of it.

Considering the real electrocatalysts are typically nano sized and have much larger surface dispersion than bulk particles, the effect of particle size on the surface reactivity was investigated by using relevant three model systems of Pt. We showed that chemical adsorption energies of O and OH changed considerably sensitive to particle sizes and surface structure (coordination number) of Pt catalysts. Furthermore, it was found that the two factors, particle size and coordination number of adsorption site were strongly coupled (see Fig. 4-2 and Fig. 4-3). However, the surface reactivity of Pt(111) surface was well below of two nano particles, which implies it may not be justified to extrapolate bulky a catalytic activity to nano particle sizes. Elegant electronic structure model was applied to describe chemisorption energies of O and OH as a function of particle size and structure of sites. The model captured overall trends reasonably well, but it shows several deviations at significantly under-coordinated sites. It represented there

was a strong interplay of electronic property and coordination number in chemical interactions between adsorbates and Pt catalysts.

In chapter 5, a general interface kinetic model, the phase field model, was used to describe Li transportation in secondary Li-ion batteries. The model could capture a non-Fickian diffusion phenomenon, and calculated Li diffusion coefficients in the multi-phase system, which were compared to the experimental techniques, GITT and PITT. This model was powerful tool in describing microstructure evolution, especially in phase separation systems such as Pt-Ru alloys.

The main conclusion of this thesis is that we have explores the structure sensitivity of electrocatalytic activity of Pt by first principles DFT method. We quantified the effect of chemical adsorbates, alloying and particle size as well as local morphology of the adsorption sites on the Pt surface reactivity.

7. References

[1] A. Hamnett, Handbook of Fuel cells- Fundamentals, Technology and Applications, **1**, 3 (2003).

[2] K Kordesch, and G. Simader, Fuel Cells and their Applications, VCH-Verlagsgesellschaft mbH, Weinheim Wiley (1996).

[3] http://www.efcf.com/media/ep010813.shtml.

[4] B. Hammer, and J. K. Norskov, Adv. Catal. **45**, 71 (2000).

[5] G. A. Sormorjai, John Wiley & Sons, INC., (1994).

[6] B. Hammer, O. H. Nielsen, and J. K. Norskov, catal. Lett. **46**, 31 (1997).

[7] A. J. Bard, R. Parsons, and J. Jordan, Marcel Dekker, New York (1985).

[8] http://thewatt.com.

[9] http://fuelcellsworks.com/Typesoffuelcells.html.

[10] http://thewatt.com.

[11] M. Winter, and R. J. Brodd, Chem. Rev. **104**, 4245 (2004).

[12] Vijay Ramani, The Electrochemical Society's Interface, **15**, 41 (2006).

[13] W. Vielstich, Handbook of Fuel cells- Fundamentals, Technology and Applications, **2**, 3 (2003).

[14] M. Watanabe, and S. Motoo, J. Electroanal. Chem. **60**, 267 (1975).

[15] N. Wakabayashi, H. Uchida, and M. Watanabe, Electrochem. Solid-State. Lett. **5**, E62 (2002).

[16] V. R. Stamenkovic *et al.*, science **315**, 493 (2007).

[17] K. Yasuda *et al.*, Phys. Chem. Chem. Phys. **8**, 746 (2006).

[18] M. Pourbaix, Pergamon, New York (1966).

[19] P. J. Ferreira *et al.*, J. Electrochem. Soc. **152**, A2256 (2005).

[20] J. Aragane, T. Murahashi, and T. Odaka, J. Electrochem. Soc. **135**, 844 (1988).

[21] T. R. Ralph, and M. P. Hogarth, Platinum Met. Rev. **46**, 117 (2002).

[22] M. S. Wilson *et al.*, J. Electrochem. Soc. **140**, 2872 (1993).

[23] A. Bonakdarpour *et al.*, J. Electrochem. Soc. **153**, A1835 (2006).

[24] D. A. J. Rand, and R. Woods, J. Electroanal. Chem., **35**, 209 (1972).

[25] D. C. Johnson, D. T. Napp, and S. Bruckenstein, Electrochim. Acta., **15**, 1493 (1970).

[26] K. Kinoshita, J. T. Lundquist, and P. Stonehart, J. Electroanal. Chem., **48**, 157 (1973).

[27] S. J. Tauster, S. C. Fung, and R. L. Garten, J. Am. Chem. Soc. **100**, 170 (1978).

[28] C. R. Henry, Surf. Sci. Rep. **31**, 231 (1998).

[29] M. S. Chen, and D. W. Goodman, science **306**, 252 (2004).

[30] Andreas Eichler, and Jürgen Hafner, Phys. Rev. B **59**, 13297 (1999).

[31] P. Sabatier, La Catalyse en Chimie Orgarnique (1913).

[32] P. J. Feibelman, and D. R. Hamann, Phys. Rev. Lett. **52**, 61 (1984).

[33] J. Harris, and S. Andersson, Phys. Rev. Lett. **55**, 1583 (1985).

[34] B. Hammer, and J. K. Nørskov, Surf. Sci. **343**, 211 (1995).

[35] R. A. Van Santen, and W. M. H. Sachtler, Surf. Sci. **63**, 358 (1977).

[36] J. A. Dalmon, and G. A. Martin, J. Catal. **66**, 214 (1980).

[37] Q. Ge, C. Song, and L. Wang Comput. Mat. Sci. **35**, 247 (2006).

[38] M. Che, and C.O. Bennet, In Advances in Catalysis, Academic press (1989).

[39] T. Stace, Nature, **331**, 116 (1988).

[40] C. R. Henry, Cryst. Res. Technol. **33**, 1119 (1998).

[41] B. C. Han *et al.*, Phys. Rev. B **72**, 205409 (2005).

[42] http://seimitsu.shinshu-u.ac.jp/IMC/TakasuSugimoto/ENG/Research.html.

[43] C. Sanchez, and E. Leiva, Handbook of Fuel cells- Fundamentals, Technology and Applications, **2**, 14 (2003).

[44] K. Honkala *et al.*, science **307**, 555 (2005).

[45] G. Ceder, G. D. Garbulski, and P. D. Tepesch, Phys. Rev. B **51**, 11257 (1995).

[46] J. McBreen, and S. Mukerjee, J. Electrochem. Soc. **142**, 3399 (1995).

[47] M. Watanabe *et al.*, Electrochemistry **68**, 244 (2000).

[48] H. A. Gasteiger, N. M. Markovic, and P. N. Ross, J. Phys. Chem **99**, 8290 (1995).

[49] T. A. Zawodzinski, T. E. Springer, and S. Gottesfeld, Abstract of the 1997 Joint International Meeting of ECS and ISE, The Electrochemistry Society Paris **97-2**, 1228 (1997).

[50] E. Christoffersen *et al.*, J. Catal. **199**, 123 (2001).

[51] J. M. Sanchez, F. Ducastelle, and D. Gratias, Physica A **128**, 334 (1984).

[52] D. de Fontaine, Solid State Physics **47**, 33 (1994).

[53] A. Zunger, MRS. Bull **22**, 20 (1997).

[54] A. Van de Walle, and G. Ceder, J. Phase Equilibria **23**, 348 (2002).

[55] B. P. Burton, and A. Van de Walle, Phys. Chem. Minerals **30**, 88 (2003).

[56] M. Asta, V. Ozolins, and C. Woodward, JOM - Journal of the Minerals Metals & Materials Society **53**, 16 (2001).

[57] B. Sadigh *et al.*, Phys. Rev. Lett. **83**, 1379 (1999).

[58] O. Wieckhorst *et al.*, Phys. Rev. Lett. **92**, 195503 (2004).

[59] G. Ceder *et al.*, Modeling and Simulation in Materials Science and Engineering **8**, 311 (2000).

[60] G. Ceder, Computational Materials Science **1**, 144 (1993).

[61] A. Van der Ven, M. K. Aydinol, and G. Ceder, Phys. Rev. B **58**, 2975 (1998).

[62] G. D. Garbulsky, and G. Ceder, Phys. Rev. B **49**, 6327 (1994).

[63] A. Van de Walle, and G. Ceder, Rev. Mod. Phys. **74**, 11 (2002).

[64] A. Van de Walle, and G. Ceder, Phys. Rev. Lett. **80**, 4911 (1998).

[65] C. Wolverton, and V. Ozolins, Phys. Rev. Lett. **86**, 5518 (2000).

[66] John L. Gland, Brett A. Sexton, and Galen B. Fisher, Surface Science **95**, 587 (1980).

[67] N. Materer *et al.*, Surf. Sci. **325**, 207 (1995).

[68] A. Eichler, and J. Hafner, Phys. Rev. Letter **79**, 4481 (1997).

[69] B. C. Stipe, M. A. Rezaei, and W. Ho, science **279**, 1907 (1997).

[70] Alexander Bogicevic, Johan Stromquist, and Bengt I. Lundqvist, Phys. Rev. B **57**, R4289 (1998).

[71] K. Bleakley, and P. Hu, J. Am. Chem. Soc. **121**, 7644 (1999).

[72] M. Lynch, and P. Hu, Surf. Sci. **458**, 1 (2000).

[73] G. Kresse, and D. Joubert, Phys. Rev. B **59**, 1758 (1999).

[74] E. A. Wood, J. Appl. Phys. **35**, 1306 (1964).

[75] H. Steininger, S. Lehwald, and H. Ibach, Surface Science **123**, 1 (1982).

[76] Hairong Tang, A.Van der Ven, and Berhardt L. Trout, Phys. Rev. B **70**, 045420 (2004).

[77] J. M. Hutchinson, Platinum Met. Rev. **16**, 88 (1972).

[78] G. N. Derry, and P. N. Ross, J. Chem. Phys. **82**, 2772 (1985).

[79] Terrell L. Hill, An introduction to Statistical Thermodynamics, Chapter 8, Addison-Wesley Pub. 2nd Ed. (1962).

[80] H. Tang, A.Van der Ven, and B. L. Trout, Phys. Rev. B **70**, 045420 (2004).

[81] C. L. Mallow, Technometrics **15**, 661 (1973).

[82] E. Christofferssen, P. Stoltze, and J. K. Nørskov, Surface Science **505**, 200 (2002).

[83] M. Watanabe, and S. Moto, J. Electroanal. Chem. **60**, 267 (1975).

[84] J. M. Chen *et al.*, J. power sources, **159**, 29 (2006).

[85] T. R. Rlalph, and M. P. Hogarth, Platinum Metals Rev. **46**, 117 (2002).

[86] A. Van der Ven *et al.*, Physical Review B **64**, 184307 (2001).

[87] A. Van der Ven, and G. Ceder, Phys. Rev. Lett. **94**, 045901 (2005).

[88] E. P. M. Leiva, E. Santos, and T. J. Iwasita, J. Electroanal. Chem. Interfacial Electrochem. **215**, 357 (1986).

[89] O. A. Petrii, and G. A. Tsirlina, Electrochimica Acta. **39**, 1739 (1994).

[90] H. A. Gasteiger *et al.*, J. Phys. Chem. **97**, 12020 (1993).

[91] X. Q. Gong *et al.*, J. Am. Chem. Soc. **126**, 8 (2004).

[92] C. T. Campbell *et al.*, J. Chem. Phys. **73**, 5862 (1980).

[93] M. Xu, J. Liu, and F. Zaera, J. Chem. Phys. **104**, 8825 (1996).

[94] J. Narayanasamy, and A. B. Anderson, J. Electroanal. Chem. **554**, 35 (2003).

[95] P. Liu, A. Logadottir, and J. K. Nørskov, Electrochimica Acta. **48**, 3731 (2003).

[96] M. Watanabe, and S. Motoo, J. Electroanal. Chem. Interfacial Electrochem. **60**, 267 (1975).

[97] G. A. Somorjai, Surface Chemistry and catalyst, John Wiley & Sons, INC, (1994).

[98] M. S Liao, C. R. Cabrera, and Y. Ishikawa, Surf. Sci. **445**, 267 (2000).

[99] Q. Ge *et al.*, J. Phys. Chem. B **105**, 9533 (2001).

[100] B. C. Han *et al.*, Phys. Rev. B **72**, 205409 (2005).

[101] F. Zaera, J. Liu, and M. Xu, J. Chem. Phys. **106**, 4204 (1997).

[102] J. L. Gland, and E. B. Kollin, J. Chem. Phys. **78**, 963 (1983).

[103] A. L. Gerrard, and J. F. Weaver, J. Chem. Phys. **123**, 224703 (2005).

[104] K. Bleakely, and P. Hu, J. Am. Chem. Soc. **121**, 7644 (1999).

[105] A. Eichler, and J. Hafner, Phys. Rev. B **59**, 5960 (1999).

[106] J. G. Wang *et al.*, Phys. Rev. Lett. **95**, 256102 (2005).

[107] B. L. M. Hendriksen, and J. W. M. Frenken, Phys. Rev. Lett **89**, 046101 (2002).

[108] X. Q. Gong, R. Raval, and P. Hu, Phys. Rev. Lett. **93**, 106104 (2004).

[109] P. E. Blöchl, Phys. Rev. B **50**, 17953 (1994).

[110] J. P. Perdew, and Y. Wang, Phys. Rev. B **45**, 13244 (1992).

[111] J. P. Perdew *et al.*, Phys. Rev. B **46**, 6671 (1992).

[112] G. Kresse, and J. Furthmuller, Phys. Rev. B **54**, 11169 (1996).

[113] G. Kresse, and J. Furthmuller, Computational Materials Science **6**, 15 (1996).

[114] N. W. Ashcroft, and N. D. Mermin, in Solid State Physics, Saunders Colledge Publishing (1976).

[115] M. Tushaus *et al.*, J. Electron Spectrosc. **44**, 305 (1987).

[116] J. Yoshinobu, and M. Kawai, J. Chem. Phys. **103**, 3220 (1995).

[117] Y. T. Wong, and R. Hoffmann, J. Phys. Chem. **95**, 859 (1991).

[118] P. J. Feibelman *et al.*, J. Phys. Chem. B **105**, 4018 (2001).

[119] H. Orita, N. Itoh, and Y. Inada, Chem. Phys. Lett. **384**, 271 (2004).

[120] Y. Yeo, L. Vattuone, and D. A. King, J. Chem. Phys. **106**, 392 (1997).

[121] U. Starke *et al.*, Surf. Sci. **287**, 432 (1993).

[122] J. L. Gland, B. A. Sexton, and G. B. Fisher, Surf. Sci. **95**, 587 (1980).

[123] A. Bogicevic, J. Stromquist, and B. I. Lundqvist, Phys. Rev. B **57**, R4289 (1998).

[124] B. Hammer, and J. K. Nørskov, Adv. Catal. **45**, 71 (2000).

[125] Y. Xu, A. V. Ruban, and M. Mavrikakis, J. Am. Chem. Soc. **126**, 4717 (2004).

[126] I. Dabo, and N. Marzari, Private communication.

[127] C. Lu *et al.*, J. Phys. Chem. B **106**, 9581 (2002).

[128] S. Volkening *et al.*, Phys. Rev. Lett., **83**, 2672 (1999).

[129] G. B. Fisher, and B. A. Sexton, Phys. Rev. Lett. **44**, 683 (1980).

[130] A. Michaelides, and P. Hu, J. Chem. Phys. **114**, 513 (2001).

[131] A. Michaelides, and P. Hu, J. Chem. Phys. **114**, 513 (2001).

[132] M. T. M. Koper, T. E. Shubina, and R. A. Van Santen, J. Phys. Chem. B **106**, 686 (2002).

[133] H. Igarashi *et al.*, Phys. Chem. Chem. Phys. **3**, 306 (2001).

[134] M.T.M. Koper *et al.*, J. Phys. Chem. B **103**, 5522 (1999).

[135] P. K. Babu *et al.*, J. Phys. Chem. B. **109** 2474 (2005).

[136] Y. Tong *et al.*, J. Am. Chem. Soc. **124**, 468 (2002).

[137] B. Hammer, and J. K. Nørskov, Adv. Catal., **45**, 71 (2000).

[138] C. R. Henry, Surf. Sci. Rep., **31**, 231 (1998).

[139] A. Wieckowski, E. R. Savinova, and C. G. Vayenas, Catalysis and Electrocatalysis at Nanoparticle Surfaces, Macel Dekker, New York (2003).

[140] M. Valden, X. Lai, and D. W. Goodman, science, **281**, 1647 (1998).

[141] J. Meier, K. A. Friedrich, and U. Stimming, Faraday Discuss., **121**, 365 (2002).

[142] N. Lopez, and J. K. Norskov, J. Am. Chem. Soc., **124**, 11262 (2002).

[143] F. Maillard *et al.*, Faraday Discuss., **125**, 357 (2004).

[144] K. J. J. Mayrhofer *et al.*, J. Phys. Chem. B, **109**, 14433 (2005).

[145] M. Arenz *et al.*, J. Am. Chem. Soc., **127**, 6819 (2005).

[146] S. Mukerjee, and J. McBreen, J. Electroanal. Chem., **448**, 163 (1998).

[147] J. Harris, and S. Andersson, Phys. Rev. Lett., **55**, 1583 (1985).

[148] N. Lopez *et al.*, J. Catal., **223**, 232 (2004).

[149] B. Hammer, and J. K. Nørskov, Suf. Sci., **343**, 211 (1995).

[150] B. Hammer, and J. K. Nørskov, Adv. Catal. **45**, 71 (2000).

[151] J. K. Nørskov, Rep. Prog. Phys., **53**, 1253 (1990).

[152] B. Hammer, and J. K. Nørskov, Chemisorption and Reactivity on supported clusters and thin films, Kluwer Academic Publishers, printed in the Netherlands, 285 (1997).

[153] J. Feibelman, and D. Hamann, Phys. Rev. Lett., **52**, 61 (1984).

[154] Z. P. Liu, P. Hu, and A. Alavi, J. Am. Chem. Soc., **124**, 14770 (2002).

[155] X. Lin *et al.*, J. Phys. Chem. B, **105**, 7739 (2001).

[156] M. H. Cohen, and M. V. Ganduglia-Pirovano, Phys. Rev. Lett., **72**, 3222 (1994).

[157] B. Hammer, Phys. Rev. Lett. **83**, 3681 (1999).

[158] K. Honkala *et al.*, science **307**, 555 (2005).

[159] M. Mavrikakis, Nature Materials, **5**, 847 (2006).

[160] Y Xu, W. A. Shelton, and W. F. Schneider, J. Phys. Chem. A, **110**, 5839 (2006).

[161] K. Kinoshita, Modern Aspects of. Electrochemistry **14, Plenum**, New York (1982).

[162] U. Heiz *et al.*, J. Am. Chem. Soc. **121**, 3214 (1999).

[163] J. Narayanasamy, and A. B. Anderson, J. Electroanal. Chem., **554-555**, 35 (2003).

[164] A. Wieckowski, E. R. Savinova, and C. G. Vayenas, Catalysis and Electrocatalysis at Nanoparticle Surfaces, Macel Dekker, New york (2003).

[165] B. C. Han, and G. Ceder, Phys. Rev. B, **74**, 205418 (2006).

[166] B. C. Han, and G. Ceder, Phys. Rev. B, **74**, 205418 (2006).

[167] K. Kinoshita, J. Electrochem. Soc., **137**, 845 (1990).

[168] M. J. Yacaman *et al.*, J. Vac. Sci. Technol. B, **19**, 1091 (2001).

[169] I. Dabo, and N. Marzari, submitted (2007).

[170] A. Michaelides, and P. Hu, J. Chem. Phys., **114**, 513 (2001).

[171] Y. P. Chiu *et al.*, Phys. Rev. Lett., **97**, 165504 (2006).

[172] U. Starke *et al.*, Surf. Sci., **287**, 432 (1993).

[173] J. L. Gland, B. A. Sexton, and G. B. Fisher, Surf. Sci., **95**, 587 (1980).

[174] Ye. Xu, A. V. Ruban, and M. Mavrikakis, J. Am. Chem. Soc., **126**, 4717 (2004).

[175] A. P. Seitsonen *et al.*, J. Am. Chem. Soc. **123**, 7347 (2001).

[176] B. Hammer, and J. K. Nørskov, Chemisorption and Reactivity on supported clusters and thin films, Kluwer Academic Publishers, printed in the Netherlands, , 285 (1997).

[177] M.S.Daw, S.M. Foiles, and M.I. Baskes, Mater. Sci. Rep. **9**, 251 (1993).

[178] K. J. J. Mayrhofer *et al.*, J. Phys. Chem. B, **109**, 14433 (2005).

[179] K. S. Han, O. H. Han, and P. K. Babu, J. Electrochem. Soc. **152**, J131 (2005).

[180] A. Sirijaruphan, J. G. Goodwin, and R. W. Rice, J. Catal. **221**, 283 (2004).

[181] M. Watanabe, S. Saegusa, and P. Stonehart, Chem. Lett. **17**, 1487 (1988).

[182] N. Giordanoa *et al.*, Electrochim. Acta **36**, 1979 (1991).

[183] Y. Takasu *et al.*, Electrochim. Acta, **41**, 2595 (1996).

[184] H. Yano *et al.*, Phys. Chem. Chem. Phys. **8**, 4932 (2006).

[185] R. Narayanan, and M. A. El-Sayed, Nano Lett. **4**, 1343 (2004).

[186] R. Narayanan, and M. A. El-Sayed, J. Phys. Chem. B **107**, 12416 (2003).

[187] N. Tian *et al.*, Science **316**, 732 (2007).

[188] Y. Xu, W. A. Shelton, and W. F. Schneider, J. Phys.Chem. B., **110**, 16591 (2006).

[189] M. D. Levi, Z. Lu, and D. Aurbach, J. Power Sources **97-98**, 482 (2001).

[190] H. C. Shin *et al.*, Electrochimica Acta **46**, 897 (2001).

[191] E. Deiss, Electrochimica Acta, **47**, 4027 (2002).

[192] F. Lantelme, H. Groult, and N. Kumagai, Electrochim. Acta **45**, 3171 (2000).

[193] C. Delmas *et al.*, Solid State Ionics **69**, 257 (1994).

[194] F. Larche, and J. W. Cahn, Acta Metall **21**, 1051 (1973).

[195] J. Stefan, Sitzber. Wien. Akad, Mat. Naturw **98**, 473 (1889).

[196] T. Miyazaki, T. Koyama, and T. Kozakai, Materials Science and Engineering A **312**, 38 (2001).

[197] J. Collins, and H. Levine, Phys. Rev. B **31**, 6119 (1985).

[198] J. S. Lange, in Directions in Condensed Matter Physics, edited by G. Grinstein and G. Mazenko (World Scientific, Philadelphia), 165 (1986).

[199] A. A. Wheeler, W. J. Boettinger, and G. B. McFadden, Phys. Rev. A **45**, 7424 (1992).

[200] J. P. Boyd, in Chebyshev and Fourier Spectral Methods (2nd ed.), Dover publications, Mineola, New York (2001).

[201] L.N. Trefethen, in Spectral Methods in Matlab, **SIAM** (2000).

[202] B. Fornberg, and D.M. Sloan, Acta Numerica **1994**, 203 (1994).

[203] W. Weppner, and R. A. Huggins, J. Electrochem. Soc. **124**, 1569 (1977).

[204] C. J. Wen, B. A. Boukamp, and R. A. Huggins, J. Electrochem. Soc. **126**, 2258 (1979).

[205] J. W. Cahn, and J. E. Hilliard, J. Chem. Phys. **128**, 258 (1958).

[206] S. M. Allen, and J. W. Cahn, Acta Metall. **27**, 1085 (1979).

[207] A. Van der Ven, and G. Ceder, J. Power Sources **97-98**, 529 (2001).

[208] A. Van der Ven *et al.*, Phys. Rev. B **64**, 184307 (2001).

[209] D. Morgan, A. Van der Ven, and G. Ceder, Electrochemical and Solid-State Letters **7**, A30 (2004).

[210] C. M. Elliott, IMA J. Appl. Math **38**, 97 (1987).

[211] C. M. Elliott, D.A. French, and F.A. Milner, Numer. Math **54**, 575 (1989).

[212] D. J. Eyre, SIAM Journal on Applied Mathematics **53**, 1686 (1993).

[213] V. Stamenkovic *et al.*, J. Phys. Chem. B **106**, 11970 (2002).

[214] C. J. Wen, B. A. Boukamp, and R. A. Huggins, Journal of the Electrochemical Society **126**, 2258 (1979).

[215] C. Masquelier *et al.*, Journal of Solid State Chemistry **135**, 228 (1998).

[216] M. D. Levi *et al.*, Journal of Electroanalytical Chemistry **477**, 32 (1999).

[217] M. D. Levi *et al.*, J. Electrochem. Soc. **146**, 1279 (1999).

[218] S. Crusius *et al.*, Zeitschrift fur Metallkunde **83**, 673 (1992).

[219] R. Poduri, and L. Q. Chen, Acta Materialia **44**, 4253 (1996).

[220] L. Proville, and A. Finel, Phys. Rev. B **64**, 054104 (2001).